



University of Kentucky
UKnowledge

Theses and Dissertations--Physics and
Astronomy

Physics and Astronomy


2018

CORRELATION BETWEEN EMISSION LINES AND RADIO LUMINOSITIES OF ACTIVE GALACTIC NUCLEI

Jessica Short-Long

University of Kentucky, jessica.k.short@gmail.com

Author ORCID Identifier:

 <https://orcid.org/0000-0003-1741-697X>

Digital Object Identifier: <https://doi.org/10.13023/etd.2018.333>

[Right click to open a feedback form in a new tab to let us know how this document benefits you.](#)

Recommended Citation

Short-Long, Jessica, "CORRELATION BETWEEN EMISSION LINES AND RADIO LUMINOSITIES OF ACTIVE GALACTIC NUCLEI" (2018). *Theses and Dissertations--Physics and Astronomy*. 55.

https://uknowledge.uky.edu/physastron_etds/55

This Doctoral Dissertation is brought to you for free and open access by the Physics and Astronomy at UKnowledge. It has been accepted for inclusion in Theses and Dissertations--Physics and Astronomy by an authorized administrator of UKnowledge. For more information, please contact UKnowledge@lsv.uky.edu.

STUDENT AGREEMENT:

I represent that my thesis or dissertation and abstract are my original work. Proper attribution has been given to all outside sources. I understand that I am solely responsible for obtaining any needed copyright permissions. I have obtained needed written permission statement(s) from the owner(s) of each third-party copyrighted matter to be included in my work, allowing electronic distribution (if such use is not permitted by the fair use doctrine) which will be submitted to UKnowledge as Additional File.

I hereby grant to The University of Kentucky and its agents the irrevocable, non-exclusive, and royalty-free license to archive and make accessible my work in whole or in part in all forms of media, now or hereafter known. I agree that the document mentioned above may be made available immediately for worldwide access unless an embargo applies.

I retain all other ownership rights to the copyright of my work. I also retain the right to use in future works (such as articles or books) all or part of my work. I understand that I am free to register the copyright to my work.

REVIEW, APPROVAL AND ACCEPTANCE

The document mentioned above has been reviewed and accepted by the student's advisor, on behalf of the advisory committee, and by the Director of Graduate Studies (DGS), on behalf of the program; we verify that this is the final, approved version of the student's thesis including all changes required by the advisory committee. The undersigned agree to abide by the statements above.

Jessica Short-Long, Student

Dr. Renbin Yan, Major Professor

Dr. Chris Crawford, Director of Graduate Studies

CORRELATION BETWEEN EMISSION LINES AND RADIO LUMINOSITIES
OF ACTIVE GALACTIC NUCLEI

DISSERTATION

A dissertation submitted in partial
fulfillment of the requirements for
the degree of Doctor of Philosophy in
the College of Arts and Sciences at
the University of Kentucky

By
Jessica Short-Long
Lexington, Kentucky

Co-Directors: Dr. Renbin Yan, Professor of Physics
and Dr. Ron Wilhelm, Professor of Physics
Lexington, Kentucky
2018

Copyright© Jessica Short-Long 2018

ABSTRACT OF DISSERTATION

CORRELATION BETWEEN EMISSION LINES AND RADIO LUMINOSITIES OF ACTIVE GALACTIC NUCLEI

Radio-loud active galactic nuclei (AGN) are one class of objects associated with accretion activity onto supermassive black holes in centers of massive galaxies. They are believed to be in a radiatively-inefficient accretion mode with low accretion rate. To understand this accretion mode, it is important to measure its radiative output at high energies ($> 13.6\text{eV}$), which can be traced through optical emission lines. However, little is known about their true radiative output. This is because no correlation between optical emission-line and radio luminosity has been found for the majority of low-luminosity radio AGN, which are often classified as low-excitation radio galaxies, or Fanaroff-Riley Class I (FR-I) radio galaxies. We demonstrate that most of the line emission found in these galaxies is not powered by the central AGN, but likely powered by some old stellar population. Only when this component is subtracted or otherwise taken into account can we estimate the true line emission associated with the AGN. These emissions may show interesting correlations with the radio luminosities in some cases.

KEYWORDS: line: profiles, radio continuum: galaxies, galaxies: nuclei, accretion, galaxies: jets

Author's signature: Jessica Short-Long

Date: August 2, 2018

CORRELATION BETWEEN EMISSION LINES AND RADIO LUMINOSITIES
OF ACTIVE GALACTIC NUCLEI

By
Jessica Short-Long

Co-Director of Dissertation: Renbin Yan

Co-Director of Dissertation: Ron Wilhelm

Director of Graduate Studies: Chris Crawford

Date: August 2, 2018

I would like to dedicate this to Orion Long, whose tiny existence prodded me along; and to Stacy Long, my love who held life together when my health fell apart...

ACKNOWLEDGMENTS

First of all, I would like to thank Stacy Long for his helpful comments on statistics and IDL programming.

Also, NASA's Astrophysics Data System Bibliographic Services greatly simplified finding references.

Lastly, as this dissertation used SDSS Data Release 7, the following acknowledgements are included:

Funding for the SDSS and SDSS-II has been provided by the Alfred P. Sloan Foundation, the Participating Institutions, the National Science Foundation, the U.S. Department of Energy, the National Aeronautics and Space Administration, the Japanese Monbukagakusho, the Max Planck Society, and the Higher Education Funding Council for England. The SDSS Web Site is <http://www.sdss.org/>.

The SDSS is managed by the Astrophysical Research Consortium for the Participating Institutions. The Participating Institutions are the American Museum of Natural History, Astrophysical Institute Potsdam, University of Basel, University of Cambridge, Case Western Reserve University, University of Chicago, Drexel University, Fermilab, the Institute for Advanced Study, the Japan Participation Group, Johns Hopkins University, the Joint Institute for Nuclear Astrophysics, the Kavli Institute for Particle Astrophysics and Cosmology, the Korean Scientist Group, the Chinese Academy of Sciences (LAMOST), Los Alamos National Laboratory, the Max-Planck-Institute for Astronomy (MPIA), the Max-Planck-Institute for Astrophysics (MPA), New Mexico State University, Ohio State University, University of Pittsburgh, University of Portsmouth, Princeton University, the United States Naval Observatory, and the University of Washington.

TABLE OF CONTENTS

Acknowledgments	iii
List of Tables	v
List of Figures	vi
Chapter 1 Background	1
1.1 General Views of AGN	1
1.2 AGN Classifications	1
1.3 Summary of Project Goals	6
Chapter 2 Data	8
2.1 Optical Data	8
2.2 Radio Band Data	8
Chapter 3 Sample Selection	10
3.1 Exclusion of Star-Forming Galaxies	10
3.2 Constructing the Radio and Control Samples	10
Chapter 4 Preliminary Results	22
4.1 Recreating Previous Results	22
4.2 Differences in Stacked Spectra	22
4.3 Differences in Cumulative Distributions	22
4.4 Quantifying the Differences	30
4.5 Statistically Extracting the Excess Line Emission from Radio-AGN	34
Chapter 5 Results from Lognormal Modeling	50
5.1 Derivation of AGN Contribution from Fenton-Wilkinson Approximation	50
5.2 Effects of Noise on Median and Standard Deviation	52
5.3 Testing Error Measurements	53
5.4 Lognormal Modeling through Random Walks	55
5.5 Revisiting the Differences in Medians	58
5.6 Discussion	58
Chapter 6 Summary	76
Bibliography	77
Vita	80

LIST OF TABLES

3.1	Sample Sizes	15
4.1	Percentage of times that Medians of the randomly-drawn control subsets are smaller than the medians of the corresponding radio sample.	30
5.1	Classifications of Radio Galaxies	70

LIST OF FIGURES

1.1	Diagnostic diagram for Seyferts, LINERs, and star-forming galaxies. . . .	2
1.2	Illustration of unified model for radio AGN.	6
3.1	Color-magnitude cuts to select redder galaxies.	11
3.2	$D_n(4000)$ -color cuts to select galaxies with older stellar populations. . . .	12
3.3	Radio samples on radio luminosity vs z plot.	13
3.4	Aperture effect on $H\alpha$ and [OIII]	14
3.5	Redshift matching between radio and control samples.	16
3.5	Caption for 3.5.	17
3.6	Stellar mass matching between radio and control samples.	18
3.6	Caption for 3.6.	19
3.7	Color matching between radio and control samples.	20
3.7	Caption for 3.7	21
4.1	Reproducing Best et al. (2005) results.	23
4.2	Comparing stacked spectra for radio and control samples for the wave- length window including $H\alpha$, [NII], and [SII].	24
4.3	Comparing stacked spectra for radio and control samples for the wave- length window including $H\beta$ and [OIII]	25
4.4	$H\alpha$ cumulative profiles.	26
4.5	$H\beta$ cumulative profiles.	27
4.6	[NII] cumulative profiles.	27
4.7	[OI] cumulative profiles.	28
4.8	[OII] cumulative profiles.	28
4.9	[OIII] cumulative profiles.	29
4.10	[SII] cumulative profiles.	29
4.11	Mean and median stability tests for [OIII].	31
4.12	Mean and median stability tests for $H\alpha$	32
4.13	$H\alpha$ profile for Bin 2.	33
4.14	Differences in $H\alpha$ medians between radio and control samples.	34
4.15	Differences in $H\beta$ medians between radio and control samples.	35
4.16	Differences in [NII] medians between radio and control samples.	36
4.17	Differences in [OI] medians between radio and control samples.	37
4.18	Differences in [OII] medians between radio and control samples.	37
4.19	Differences in [OIII] medians between radio and control samples.	38
4.20	Differences in [SII] medians between radio and control samples.	38
4.21	AGN-powered $H\alpha$ mean vs radio luminosity using simple mean subtraction.	39
4.22	AGN-powered $H\alpha$ mean vs radio luminosity using simple mean subtraction under the czv matching scheme.	40
4.23	AGN-powered $H\alpha$ mean vs radio luminosity using simple mean subtraction under the czmv matching scheme.	41

4.24	AGN-powered $H\beta$ mean vs radio luminosity using simple mean subtraction.	42
4.25	AGN-powered [NII] mean vs radio luminosity using simple mean subtraction.	43
4.26	AGN-powered [OI] mean vs radio luminosity using simple mean subtraction.	44
4.27	AGN-powered [OII] mean vs radio luminosity using simple mean subtraction.	45
4.28	AGN-powered [OIII] mean vs radio luminosity using simple mean subtraction.	46
4.29	AGN-powered [OIII] mean vs radio luminosity using simple mean subtraction under the czv matching scheme.	47
4.30	AGN-powered [OIII] mean vs radio luminosity using simple mean subtraction under the czmv matching scheme.	48
4.31	AGN-powered [SII] mean vs radio luminosity using simple mean subtraction.	49
5.1	Histograms of lognormal simulations of Control Bin 2's $H\alpha$ distribution.	50
5.2	Effects of noise on lognormal distributions.	52
5.3	Error vs signal scatter plot for $H\alpha$ of Control Bin 4.	53
5.4	The rms of negative $H\alpha$ values divided by the median reported errors as a function of control bin.	54
5.5	Lognormal modeling random walk.	56
5.6	Examples of lognormal model fitting.	57
5.7	Simulated $H\alpha$ distributions.	59
5.8	Simulated $H\beta$ distributions.	60
5.9	Simulated [NII] distributions.	61
5.10	Simulated [OI] distributions.	62
5.11	Simulated [OII] distributions.	63
5.12	Simulated [OIII] distributions.	64
5.13	Simulated [SII] distributions.	65
5.14	Simulated $H\alpha$ differences in medians.	66
5.15	Simulated $H\beta$ differences in medians.	66
5.16	Simulated [NII] differences in medians.	67
5.17	Simulated [OI] differences in medians.	67
5.18	Simulated [OII] differences in medians.	68
5.19	Simulated [OIII] differences in medians.	68
5.20	Simulated [SII] differences in medians.	69
5.21	Comparing radio luminosity to radio-to-Eddington ratios.	71
5.22	Comparing AGN mean $H\alpha$ -to-Eddington ratios to median radio-to-Eddington ratios.	73
5.23	Comparing AGN mean [NII]-to-Eddington ratios to median radio-to-Eddington ratios.	73
5.24	Comparing AGN mean [OI]-to-Eddington ratios to median radio-to-Eddington ratios.	74
5.25	Comparing AGN mean [OII]-to-Eddington ratios to median radio-to-Eddington ratios.	74
5.26	Comparing AGN mean [OIII]-to-Eddington ratios to median radio-to-Eddington ratios.	75

5.27 Comparing AGN mean [SII]-to-Eddington ratios to median radio-to-Eddington ratios.	75
--	----

Chapter 1 Background

1.1 General Views of AGN

Supermassive black holes (SMBHs) are found at the centers of most massive galaxies. These SMBHs are typically between 10^6 and 10^{10} solar masses (Frolov & Zelnikov, 2011), and their growth seems to be linked to the evolution of their host galaxies. For example, according to the findings of Magorrian et al. (1998), most galaxies have values of $\log(M_{SMBH}/M_{bulge})$ that fall within the range of -2.27 ± 0.07 , indicating some correspondence between black hole and galaxy bulge masses. Furthermore, there is a correlation between the mass of SMBHs and the velocity dispersion of galactic stars, known as the $M - \sigma$ relation. Gebhardt et al. (2000) found that the mass of the supermassive blackhole is roughly proportional to $\sigma^{3.75(\pm 0.3)}$ where σ is the line-of-sight velocity dispersion of stars within the half-light radius (hereafter called v_{disp} to avoid confusion with our standard deviations). To explain these correlations, it has been proposed that SMBHs may produce an energy feedback mechanism that leads to suppression of star formation in host galaxies (Sijacki et al., 2007). In order to further evaluate this theory, we must understand how the SMBH processes energy via accretion. Accretion of material can release energy in one of two ways: kinetically (by throwing material away from the SMBH) or radiatively. To understand the mechanics of the AGN (and thus increase our understanding of the SMBH-galaxy relation), we should evaluate the amount of energy released in either method. Thus, we need to measure the radiative output and accretion rates for different types of AGN.

Accretion disks form as materials, such as gas, fall onto a SMBH. The viscosity of the in-falling fluid helps transport its angular momentum. This process allows its gravitational potential energy to be released thermally (by raising the temperature within the gas) and then radiatively as photons, or kinetically by propelling the gas outward into ultra-relativistic jets (Netzer, 2013). These regions, which emit photons ranging from radio to x-ray (or even beyond), form what is known as active galactic nuclei or AGN.

1.2 AGN Classifications

Observationally, AGN have been classified into a dozen different types based on different detection techniques, luminosity, spectral property, and variability. Notice that these classification schemes are not mutually-exclusive as one can apply all of them to a given AGN. In this section, we will give an overview of three classification schemes—optical emission lines, radio-loudness, and accretion mode—as well as how they relate to this project. First, we will examine optical spectra classifications.

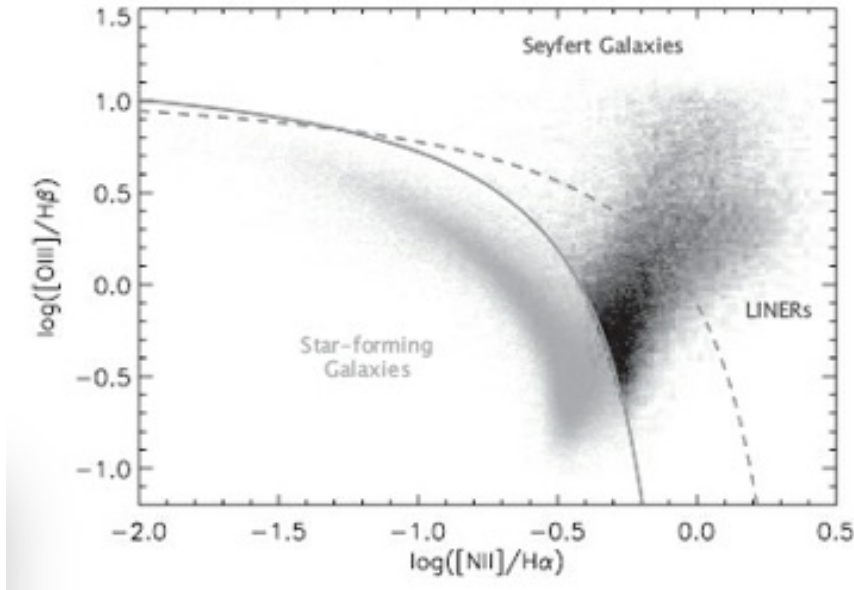


Figure 1.1: This is the diagnostic diagram shown on page 120 of Netzer (2013). The vertical axis indicates increasing ionization parameter (as estimated by $[OIII]/H\beta$) and the horizontal axis shows increasing $[NII]/H\alpha$. The respective locations of star-forming galaxies, Seyfert AGN, and LINER AGN are labeled on the diagram.

Optical Emission Lines

Using optical spectra, an AGN may be classified as high-luminosity (Quasars) for absolute magnitudes brighter than approximately -23. AGN with absolute magnitudes dimmer than -23 are low-luminosity AGN. These low-luminosity AGN may be further classified as Seyferts (with $[OIII]/H\beta > 3$ and $[NII]/H\alpha > 0.6$) or as low-ionization nuclear emission-line region (LINER) with $[OIII]/H\beta < 3$ and $[NII]/H\alpha > 0.6$.

Within AGN galaxies, emission lines result from electron transitions in photoionized or collisionally-ionized gas (Netzer, 2013). As hydrogen is the most abundant element, the ionization parameter is defined as the ratio between the hydrogen-ionizing photon flux (which must have energies >13.6 eV) and the total density of hydrogen gas. The ionization parameter should correlate to the fraction of hydrogen gas that is ionized (Netzer, 2013).

Netzer (2013) describes the ionization parameter as it relates to Seyfert/LINER classifications. A high $[OIII]$ (resulting from doubly-ionized oxygen) to $H\beta$ ratio generally indicates high ionization levels. Seyfert AGN have high ionization parameters and thus will have higher $[OIII]/H\beta$ ratios, whereas LINERs have low ionization parameters and are classified by the lower $[OIII]/H\beta$ ratios.

At this point, it is worth mentioning that both LINERs and Seyferts tend to have higher $[NII]/H\alpha$ ratios than those of star-forming galaxies. These differences are explicitly shown in diagnostic diagrams, such as the one shown in Netzer (2013) (see Figure 1.1). We will focus on the LINER class below.

LINER Emission Lines Powered by Sources Other than AGN

In our overview of optical classifications, a few key characteristics of LINER galaxies should be mentioned. Firstly, LINER-like emission line ratios are common among red galaxies. Secondly, while some galaxies classified as LINERs contain AGN, the dominant ionization mechanism of LINERs has been a subject of debate. The four proposed ionization mechanisms of LINERs are photoionization by AGN (Ferland & Netzer, 1983; Halpern & Steiner, 1983), photoionization by hot x-ray emitting gas (Voit & Donahue, 1990; Kim, 1989), shocks (Heckman et al., 1989; Dopita & Sutherland, 1995), and photoionization by hot evolved stars (di Serego Alighieri et al., 1990; Binette et al., 1994). Most LINERs do host weakly-accreting supermassive black holes, the evidence of which is cited by Ho (2008). However, the ionization of gas in most LINERs is not necessarily powered by these weak AGN. In fact, the weak AGN may only be capable of powering emissions within the central 10-20 pc of their host galaxies, and thus are not strong enough to power the line emissions on galactic scales on the order of 100 pc or larger (Eracleous et al., 2010). Therefore, it is entirely possible that another ionization mechanism may dominate the large scale emission lines of LINER galaxies.

This idea holds up in analyses of the spatial distributions of line emissions and line ratio gradients (Sarzi et al., 2010; Yan & Blanton, 2012; Singh et al., 2013; Papaderos et al., 2013; Belfiore et al., 2016). In their paper, Yan & Blanton (2012) found that the emission lines from many LINER-classified galaxies follow patterns indicative of spatially-distributed ionization sources, thus ruling out the idea that LINER ionization is exclusively (or even predominantly) powered by point-source AGN. Instead, photo-ionization by hot, evolved stars, such as post-asymptotic giant branch (post-AGB) stars, is a promising candidate. Stasińska et al. (2008) and Cid Fernandes et al. (2011) show that these stars could provide enough ionizing photons to power the line emission on larger scales. However, the primary ionizing source in these galaxies remains a topic of research.

Regardless of the exact source of ionization, evidence clearly indicates that most, if not all, of the line emission in a LINER is powered by non-AGN sources, especially in cases when the spectroscopy covers light from kpc scales in a galaxy. Therefore, to study the emission line properties associated with the AGN in a radio galaxy, we must remove or control for those line emission that is not powered by AGN. This should allow us to evaluate any correlation between AGN-powered emission lines and radio luminosity (which indicates kinetic of the AGN). Such a correlation could give us information on AGN mechanics.

Emission Line Widths

Historically, AGN have been categorized by the widths or equivalent widths of their permitted (or high-probability) emission lines, such as $H\alpha$ and $H\beta$. Type-I AGN have broad permitted emission lines, the physical explanation of which will be discussed in the subsection on the AGN Unified Model. It is worth noting that low-luminosity broad emission lines may be difficult to detect (Netzer, 2013). Contrastingly, Type-II

AGN tend to have narrow permitted lines. Both types tend to display fairly narrow forbidden (low-probability) lines, such as [NII], [OII], and [OIII], which tend to be similar in width to the permitted lines in Type-II AGN (Netzer, 2013).

Radio-Loudness and Luminosity

Now that we have briefly outlined the pertinent aspects of optical AGN classification, let's examine radio classifications of AGN. Astronomers generally agree that some AGN produce radio waves via synchrotron radiation in relativistic jets and lobes of material shooting out from the AGN. Beyond that, discussions of radio AGN classifications can be inconsistent. Nonetheless, we will address a few of the broad classification schemes. First, astronomers often refer to radio-loud versus radio-quiet AGN. These categories simply refer to AGN with high versus low radio band to optical luminosity ratios. For this project, we chose not to classify our target objects by radio-loudness, but simply by radio luminosity. Since radio-loudness is usually defined by the ratio between radio luminosity and optical luminosity and much of the luminosity can be dominated by distributed sources in galaxies with relatively weak AGN, radio-loudness does not depend solely on the properties of the AGN. Therefore, instead of radio-loudness, we adopt radio luminosity as the primary parameter in our studies.

Secondly, radio AGN are often categorized according to their morphologies as Fanaroff-Riley I (FR I) or FR II AGN (Fanaroff & Riley, 1974). FR I objects have most of their radio luminosity concentrated in the AGN and nearby relativistic jets, with the luminosity decreasing at greater radii. FR II objects, contrastingly, are most luminous in the lobes on either side of the AGN. Measuring the power at 151 MHz, Ghisellini & Celotti (2001) reports that the division between FR I and the generally higher-power FR II objects occurs when the kinetic power of the jets is approximately 0.015 times the Eddington Limit (or the maximum luminosity which can be emitted in balance with the mass of the SMBH). Still, Ghisellini & Celotti (2001) warn that the separation is likely blurred.

Thirdly, radio-loud AGN galaxies are classified according to their optical emission spectra as high-excitation or low-excitation radio galaxies, which roughly corresponds to the Seyfert-versus-LINER optical classification. For example, radio galaxies have been classified as high-excitation radio galaxies (HERG) and low-excitation radio galaxies (LERG) according to the classification of their optical spectra in line ratio diagnostic diagrams (Best & Heckman, 2012). Most radio galaxies have an optical spectrum that has line ratios characteristic of Low-Ionization Nuclear Emission-line Regions (LINERs). Emission line-based classifications makes sense if the emission lines can be attributed to the AGN. However, this AGN classification becomes somewhat problematic and even misleading if the emission lines are primarily powered by stellar or other non-AGN sources.

When considering radio galaxies, a natural question arises as whether there is any correlation between radio and emission line luminosities. Such a correlation is known at higher luminosities, which makes sense as radio power can be used to estimate the kinetic energy of the jets (Ghisellini & Celotti, 2001). However, in their 2005

paper, Best et al. (2005) studied galaxies in the lower radio luminosity ranges. Upon plotting [OIII] luminosities versus radio luminosities, Best et al. (2005) did not find any significant emission line-radio luminosity relationship between radio luminosities of approximately $22.5 < \text{Log}(L_{\text{SNVSS}}/WHz^{-1}) < 25.0$. However, this research (which included spectra galaxies covering several kpc), did not consider the possibility of stellar-powered or other spatially-distributed ionization sources, which Yan & Blanton (2012) already established as a major contributor to emission line luminosities in many LINER-like galaxies. Thus, the first goal of this project is to isolate the actual radio-detected AGN contribution of emission lines. As will be shown, the stellar-powered emission line contribution may be statistically estimated and removed (thus, leaving the AGN contribution) by using a control group of non-radio galaxies.

Accretion Mode and Energy Release

In addition to optical and radio classifications, the final AGN classification pertinent to this project is that of accretion mode. AGN may be powered by either a radiatively-efficient accretion mode or radiatively-inefficient accretion flow (RIAF). Radiatively-efficient accretion modes typically have high accretion rates and release a relatively high fraction of energy as electromagnetic radiation (in comparison to a RIAF). Seyferts and quasars are thought to be powered by radiatively-efficient accretion mode. RIAFs, on the other hand, have lower accretion rates and are thought to likely power low-excitation radio galaxies. Unfortunately, there are currently few observational constraints on RIAFs. In order to better understand and place constraints on RIAF models, we need to measure the radiative output of AGN, which can be accomplished by studying their emission lines. This brings us to the second and final goal of this project: to contribute to our understanding of RIAFs by accurately measuring the radiative output of radio AGN.

AGN Unified Model

The AGN unification theory has achieved great success at explaining many of these different types of AGNs as the same physical phenomena viewed from different viewing angles (Urry & Padovani, 1995).

AGN unification theory can unify the broad line objects with narrow line objects as the same objects seen from different orientations, as illustrated by Figure 1.2 (Urry, 2003). According to the unified model, the SMBH and its accretion disk are surrounded by an obscuring toroid. Emission lines originating from regions near the SMBH are motion-broadened due to gas speeds of up to thousands of km/s. Thus, this area is known as the Broad-Line Region (BLR). The area further away from the SMBH produces narrow emission lines (due to lower gas velocities), and thus is known as the Narrow-Line Region (NLR). According to this model, if our viewing angle causes the BLR to be obscured by the dusty toroid, we detect only the narrow lines. Likewise, if our viewing angle provides a more direct observation of the central engine, we can more easily detect both the broad lines from the BLR and the narrow lines from the NLR.

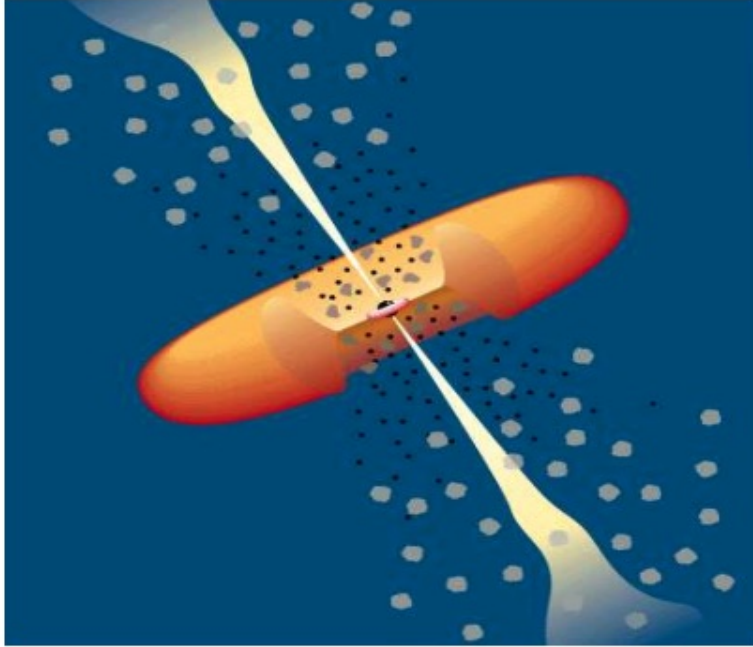


Figure 1.2: This diagram illustrates the unified model for radio-loud AGN (Urry, 2003). The SMBH is in the center, surrounded by its accretion disk. An obscuring toroidal disk surrounds the SMBH, accretion disk, and broad-line region (BLR). The corona of hot electrons and narrow-line region (NLR) extend beyond the toroid. Outflow jets (which emit in the radio band via synchrotron radiation) shoot from either side of the SMBH.

The unified model also accounts for highly-variable, intense radio and γ -ray sources—known as blazars (Netzer, 2013). According to the model, blazars differ from other radio AGN only in their orientation toward us, with blazars directing their relativistic jets toward Earth (Urry & Padovani, 1995). Currently, we do not know what physically causes an AGN to be radio-loud or radio-quiet. Do any radio-quiet AGN have jets, and, if not, why not? A few culprits have been suggested, such as the spin of the black hole (Wilson & Colbert, 1995) or differences in accretion mode. Radiatively-inefficient accretion flow (Narayan & Yi, 1994, 1995; Blandford & Begelman, 1999; Quataert & Gruzinov, 2000; Hawley & Balbus, 2002) has been proposed to explain the radio-loud objects, while the classical accretion disk could explain the radio-quiet objects. In this dissertation, we attempt to shed light on the physical origins of radio-loudness by studying the statistical difference in optical emission line luminosity between radio-loud and radio-quiet galaxies.

1.3 Summary of Project Goals

In this dissertation, we will revisit the question of how much line emission is actually associated with the AGN, as well as whether there are correlations between AGN-

powered emission lines and radio luminosities in LINER galaxies. We use control samples that are matched to radio galaxies in a number of galaxy properties—stellar mass, color, and redshift—in order to estimate the emission line contribution of non-AGN sources. We will then examine the emission line luminosity difference between radio-luminous galaxies and radio-faint galaxies to check for correlation between the AGN-only emission line luminosity and radio luminosity.

In summary, this project seeks to isolate the radio AGN contribution to emission lines and use those emission line distributions to shed light on the actual radiative output of RIAF-powered radio AGN.

This dissertation will have the following format: Chapter 2 will describe our data catalogs, followed by our sample selection methods in Chapter 3. Chapter 4 describes early, straight-forward attempts to isolate the AGN-powered emission line distributions, as well as the drawbacks to these elementary methods. Chapter 5 details our attempts to improve the previous chapter's results through using lognormal distributions to model the AGN-powered and non-AGN powered emission line distributions. The findings will be summarized in Chapter 6.

Chapter 2 Data

2.1 Optical Data

Our optical data originated from the seventh data release of the Sloan Digital Sky Survey (SDSS DR7, York et al. 2000; Abazajian et al. 2009). SDSS consisted of three surveys: Legacy, Sloan Extension for Galactic Understanding and Exploration (SEGUE), and the Supernova Survey, all of which were performed using the 2.5 m telescope at the Apache Point Observatory, SDSS Legacy survey obtained extensive u, g, r, i, and z band imaging over 8200 square degrees, and spectroscopy data for several hundred thousand of galaxies and quasars.

SEGUE provided additional spectroscopy of 240,000 stars, along with 3240 square degrees of sky images. The Supernova Survey, which had the primary goal of finding supernovae, scanned the area between declinations of ± 1.25 degrees with right ascension less than 59 degrees or greater than 310 degrees. Altogether, the seventh data release of SDSS contained data from 1,640,940 spectra of various objects and the sky (Abazajian et al., 2009).

We used the data compiled in the New York University Value Added Galaxy Catalog (NYU-VAGC, Blanton et al. 2005), which provides a magnitude-limited sample brighter than r of 17.9. Using spectra extracted from spPlate files on the SDSS Science Archive Server, we have fitted the stellar continuum using a set of stellar population templates from Bruzual & Charlot (2003). After subtracting the stellar continuum, we measured the flux and equivalent widths for all the strong emission lines in the spectra. The details are described by Yan & Blanton (2012). As detailed in Yan (2018), additional zeropoint corrections were applied to the equivalent width and emission line flux. The uncertainty for emission line equivalent width and fluxes are scaled up slightly according to repeated observations, which will be discussed in section 5.3.

2.2 Radio Band Data

In addition to the SDSS optical data, we employ 1.4GHz radio continuum data from the National Radio Astronomy Observatory Very Large Array Sky Survey (NVSS), which covered the entire sky north of -40 deg declination. NVSS has a resolution of 45" FWHM, and coordinate uncertainties varying from $< 1''$ in strongly-detected radio sources to 7" in more faintly-detected sources (Condon et al., 1998).

For convenience, this project used the radio source catalog compiled by Best & Heckman (2012) from NVSS and the Faint Images of the Radio Sky at Twenty Centimeters (FIRST) survey cross-matched with SDSS galaxy catalog. The crossmatching had a lower detection limit of 5 mJy. Since it covers the entire area of the SDSS, using this catalog gives us a complete sample of radio sources above 5 mJy. Galaxies that were not detected had fainter radio fluxes. Such galaxies were used to construct

the control sample. From this point, we will refer to the Best & Heckman (2012) catalog with supplemental data from SDSS as the "radio catalog".

Chapter 3 Sample Selection

3.1 Exclusion of Star-Forming Galaxies

Radio signals can originate from both AGN and star-forming regions. To study AGN and remove star-forming galaxies from the merged data, four initial cuts were adopted. We adopted the following cuts based on color and spectral index to achieve this. We avoided basing cuts on emission lines so as to not bias the emission line properties of the samples. As the majority of radio AGN are in massive, early-type galaxies, the first two cuts were color-magnitude criteria designed to select red galaxies with old stellar populations (see Figure 3.1):

$$^{0.1}(g - r) \geq -0.02M_{0.1r} + 0.49 \quad (3.1)$$

$$^{0.1}(g - r) \leq -0.02M_{0.1r} + 0.59 \quad (3.2)$$

Significant variation in star formation rates could have two undesirable effects on data: altering emission line properties and adding radio luminosity such that the galaxies could not be accurately classified by their AGN radio luminosities. Some of these star-forming galaxies could possibly be found in the red sequence due to dust attenuation. A well-defined 4000-Angstrom break (which is caused by metal absorption lines) indicates an absence of younger stars (Bruzual A., 1983). This feature, unlike color alone, is fortunately not sensitive to dust. As shown in Figure 3.2, there is a plume of galaxies with red color but low $D_n(4000)$. These are dusty star-forming galaxies and post-starburst galaxies. So, by excluding the galaxies with low $D_n(4000)$ ratios (along with any galaxies with extremely high ratios), the next two cuts helped to remove remnant star-forming galaxies from the sample (see Figure 3.2):

$$D_n(4000) \geq 1.6^{0.1}(g - r) + 0.26 \quad (3.3)$$

$$D_n(4000) \leq 1.6^{0.1}(g - r) + 0.52 \quad (3.4)$$

3.2 Constructing the Radio and Control Samples

From here, we made a number of telling plots in order to compare results from our samples to the Best et al. (2005) results by studying the emission line as a function of radio luminosity. Naturally, for these studies, we excluded galaxies lacking data for any of the emission lines we studied ($H\alpha$, $H\beta$, [NII], [OI], [OII], [OIII], or [SII]). Then, we divide the radio galaxies into six radio luminosity bins according to their radio luminosity from NVSS $\log(L_{NVSS}/WHz^{-1}h^{-2})$, with a spacing of 0.5 dex. Galaxies that are undetected in the radio band (radio flux less than 5 mJy) serve as our overall

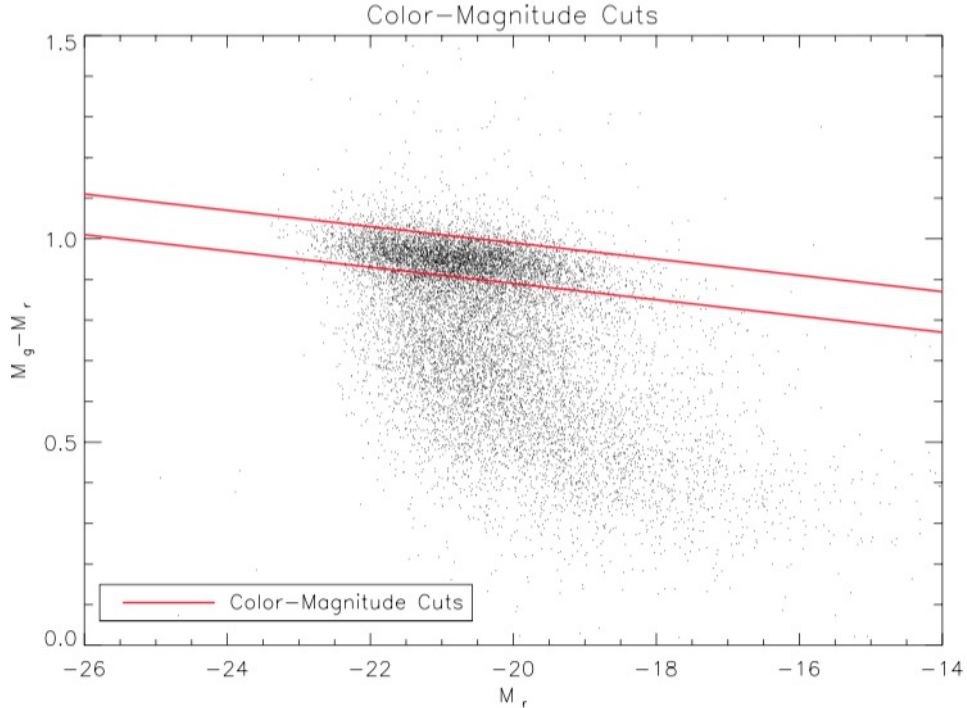


Figure 3.1: Color-magnitude plot for SDSS galaxies within $0.03 < z < 0.35$. With the magnitude numbering scheme, redder galaxies lie closer to the top of the plot, while bluer galaxies are nearer to the bottom. The individual black dots represent a 2% random sampling of all galaxies in our data set (to preserve the visibility of the density distribution). The solid lines show the upper and lower limits (Eqn. 3.1 and 3.2) that were placed to select red sequence galaxies from the data set.

control group. For the six radio luminosity bins, we placed corresponding redshift limits on each sample such that the highest redshift for each bin did not exceed the farthest distance at which the lower radio luminosity limit was still detectable by NVSS (see Figure 3.3). Our methods depend on comparing the emission line luminosities of radio galaxy samples to those of their corresponding control groups. By applying these redshift limits to each radio sample and their corresponding control sample, we ensure all control galaxies have much fainter radio luminosities than those in the radio sample.

We constructed radio-faint control samples to be compared with the radio-luminous samples. Because a large portion of the line emission could be powered by non-AGN sources in these galaxies, we would like the control sample to have the same galaxy properties as the galaxies hosting radio AGN. Although we do not know exactly what factors determine the strength of the line emission powered by non-AGN sources, we tried to replicate the conditions by matching each control sample with its corresponding radio sample in stellar mass, color, and stellar velocity dispersion. These would make sure the stellar population ages, masses, and depth of the gravitational

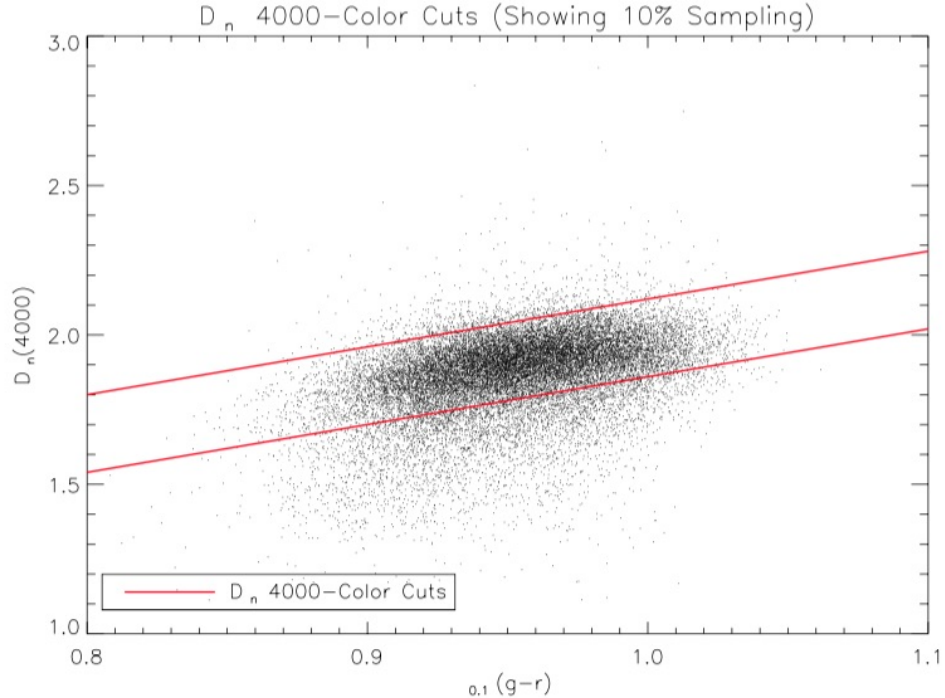


Figure 3.2: The vertical axis depicts the $D_n(4000)$ ratio value, whereas the horizontal axis depicts the green band magnitude minus the red band magnitude at redshift 0.1. Hence, the bluer galaxies are toward the left of the plot. Moreover, the galaxies with the stronger $D_n(4000)$ values (hence, the older stellar populations) are higher on the plot. The solid lines show the upper and lower bounds set for the final sample. The individual dots represent a 10 percent random sampling of galaxies before the $D_n(4000)$ -color cuts were taken.

potentials (as indicated by velocity dispersions) are similar between the control samples and the corresponding radio samples. The necessity of considering these factors becomes apparent considering that stellar age (indicated by color), total stellar mass, and velocity dispersion (which indicates the strength of gravitational potential in a galaxy’s central regions) can affect emission lines (Best et al., 2005). We would have a good chance to ensure the non-AGN contribution to the emission lines are similar between the two samples.

In addition to these three factors, the galaxies’ redshifts can affect the luminosities of emission lines through the aperture effect. The aperture effect simply denotes the concept that galaxies which are closer to the telescope (and thus have a lower redshift) cover a larger angle of view than higher-redshift objects of the same actual size. Thus, the spatially-extended stellar-powered light from a lower-redshift galaxy may not be fully detected by the optical fiber, an effect which could be compared to attempting to photograph a large object too close to the camera lens. This means that, if we consider two galaxies with identical spectra and actual sizes—Galaxy A at redshift 0.03 and Galaxy B at redshift 0.15—SDSS may miss the flux from the

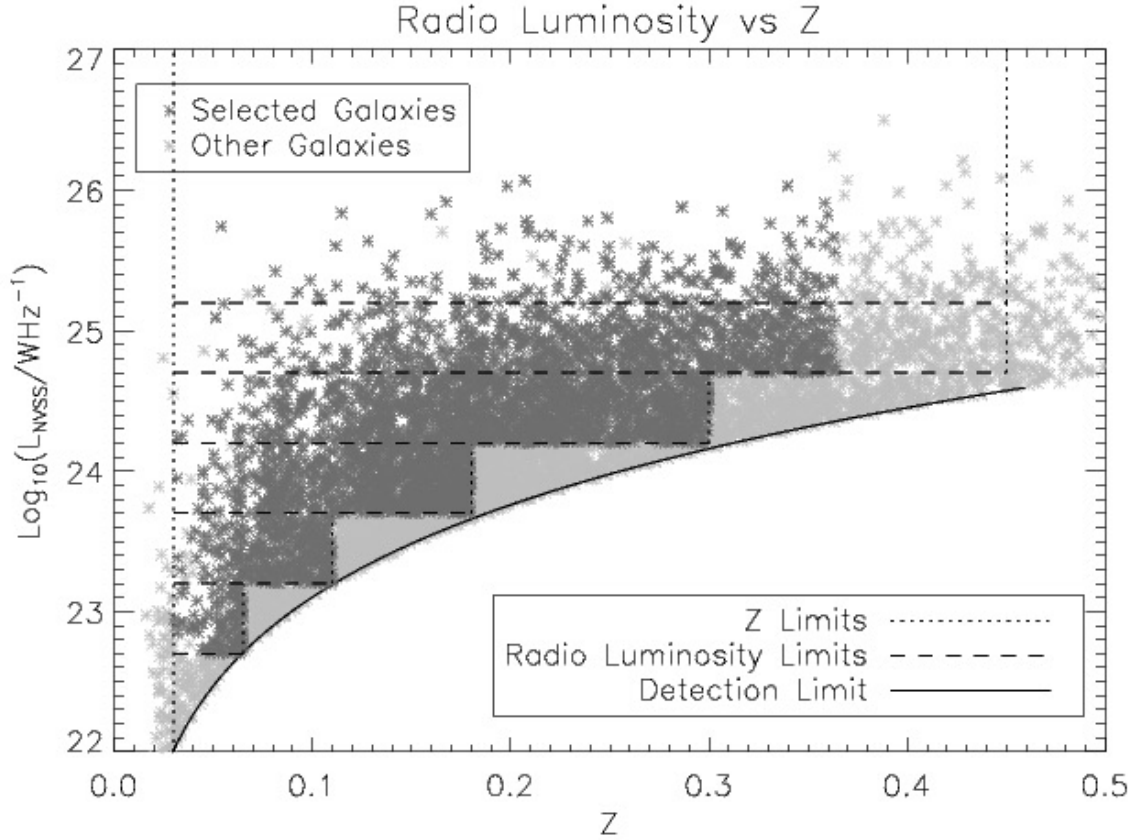


Figure 3.3: This radio luminosity versus redshift plot depicts the redshift and luminosity cuts for the six radio luminosity bins. The vertical dotted lines represent the redshift limits adopted for each radio sample, and the dashed horizontal lines show the radio luminosity boundaries between the radio samples. The vertical axis labels the logarithm of the radio luminosity, which is in units of watts per hertz. The horizontal axis shows redshift. Moreover, the darker symbols show the radio galaxies selected after the redshift cuts were made, whereas the lighter symbols show rejected galaxies. The solid black curve represents the detection limit of radio luminosity as a function of redshift. Notice that, as expected, no galaxies (either accepted nor rejected) appear below the detection limit.

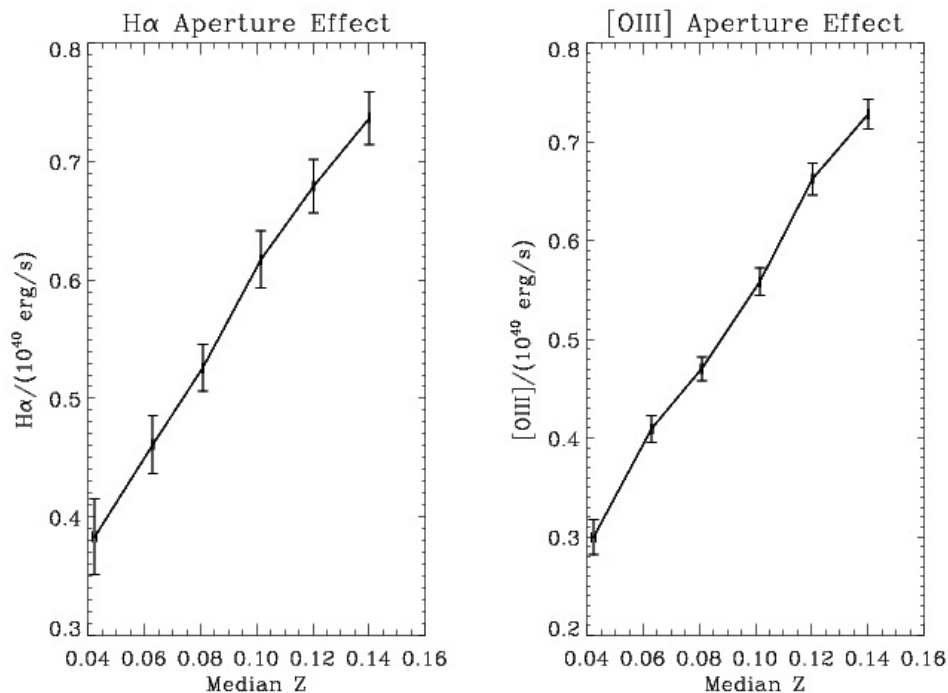


Figure 3.4: .

]These figures demonstrate the aperture effect for $H\alpha$ and [OIII]. The other emission lines of this project demonstrated this effect as well. To create these plots, a sample within a narrow stellar mass range of $10^{10.75}$ to $10^{10.80} M_{sun} h^{-2}$ (to avoid biasing the samples with vastly different stellar masses) was divided into bins according to redshift. Then, for each bin, the median emission line luminosity was plotted against the median redshift. The vertical axes show emission line luminosities in 10^{40} erg/s, whereas the horizontal axes denote redshift. The solid black lines indicate the median emission line luminosities for each redshift bin, and the vertical and horizontal error bars show the errors in median estimates for emission line luminosities and redshift, respectively. Notice that, at these redshifts, detected emission line luminosity significantly increases with redshift, as one would expect for the aperture effect.

Table 3.1: Sample Sizes

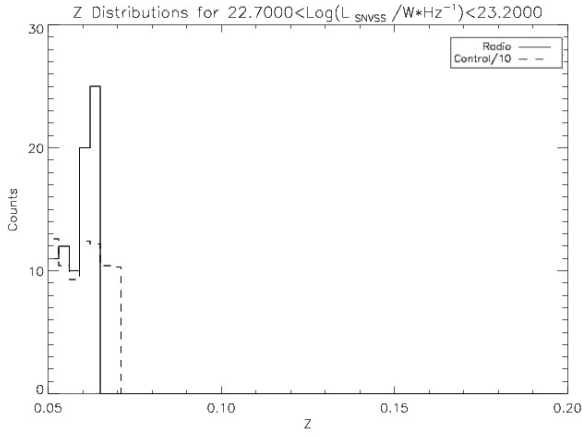
Bin	# of Radio Galaxies	# of Control Galaxies
1	104	1040
2	348	3480
3	920	9200
4	1430	14,300
5	805	8050
6	190	1900

outer parts of Galaxy A and subsequently underreport Galaxy A’s luminosity relative to Galaxy B’s. This effect has been demonstrated by Yan & Blanton (2012). We were able to recreate the aperture in the figures below 3.4 by showing that, for relatively-close redshifts (less than about 0.2), the emission line luminosity increases with increasing redshift, despite limiting the stellar masses to a very narrow range of $10^{10.75}M_{sun}h^{-2} < M_* < 10^{10.80}M_{sun}h^{-2}$.

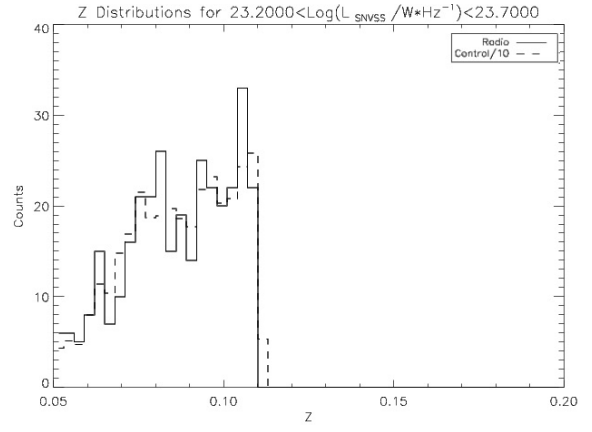
Nonetheless, since the AGN is approximately at the center of a galaxy, the optical fiber should capture the AGN-powered light. The missing part of extended stellar-powered emission luminosities can be safely ignored as long as the radio galaxy is compared to control galaxies experiencing approximately the same aperture effect.

So far, we’ve described four properties that optimally should be matched to create control samples for each radio category. For the radio sample in each radio luminosity bin, we constructed a control sample matching it in multi-dimensional parameter space. For each radio galaxy, we randomly selected 10 radio-undetected control galaxies which had similar values regarding the aforementioned properties. Occasionally, there weren’t 10 available radio-undetected galaxies closely matching a given radio galaxy, in which case the radio galaxy was excluded from the sample, naturally resulting in a reduction of sample size. Thus, the more dimensions we matched, the more severely the sample size was constrained.

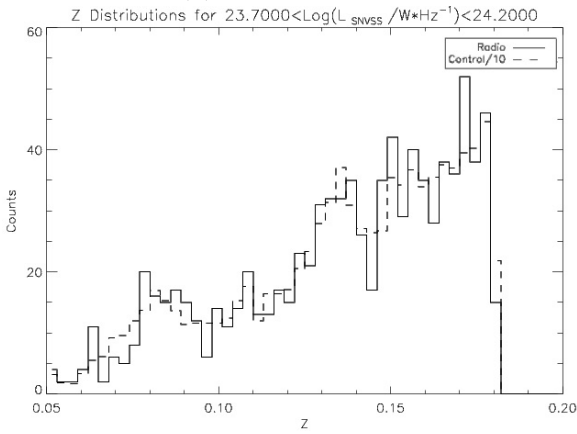
For one such matching scheme, six copies of the control sample were matched to the six radio luminosity samples in redshift (Figure 3.5), $^{0.1}(g-r)$ (Figure 3.7), and stellar mass (Figure 3.6) in order to promote consistency in aperture effect, color, and stellar mass respectively. We will refer to this as the “czm” scheme. Similarly, we tried matching redshift, $^{0.1}(g-r)$, and velocity dispersion in our “czv” matching scheme. Lastly, we matched all four attributes in our “czmv” matching scheme. Note that, for all three schemes, the matching bins were defined as follows: $\Delta z = \pm 0.01$, $\Delta \log M = \pm 0.2$, $\Delta ^{0.1}(g-r) = \pm 0.005$, $\Delta v_{disp} = \pm 15\text{km/s}$. Because the three matching schemes seemed to give us fairly similar results in our stronger lines (compare Figures 4.22 and 4.23 to Figure 4.21, as well as Figures 4.29 and 4.30 to Figure 4.28) and the czmv scheme seemed to limit our sample size unnecessarily, we chose to use the czm matching scheme for the rest of the project. The final sample sizes for the czm scheme are recorded in Table 3.1.



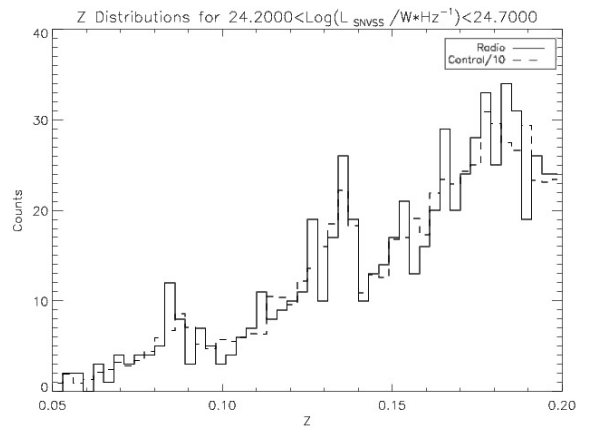
(a) 1st Radio Bin



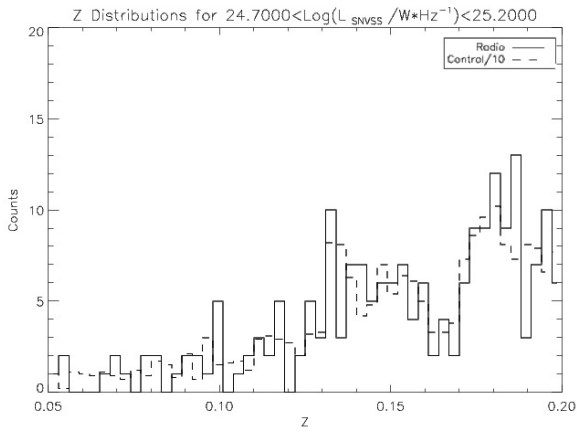
(b) 2nd Radio Bin



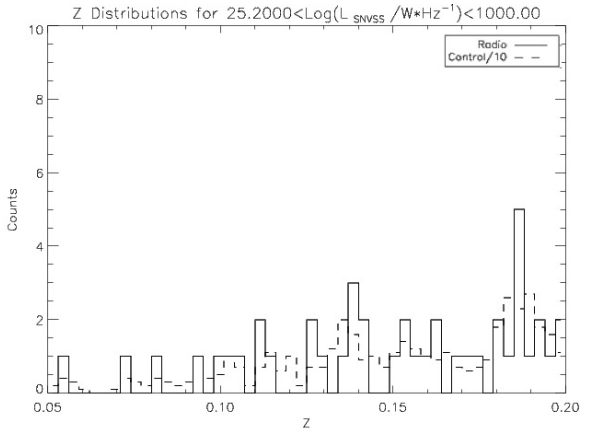
(c) 3rd Radio Bin



(d) 4th Radio Bin



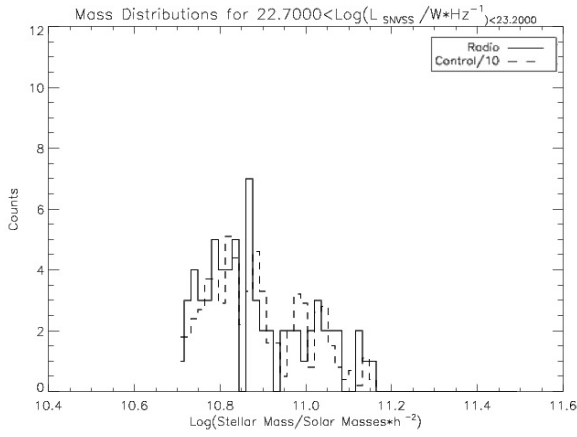
(e) 5th Radio Bin



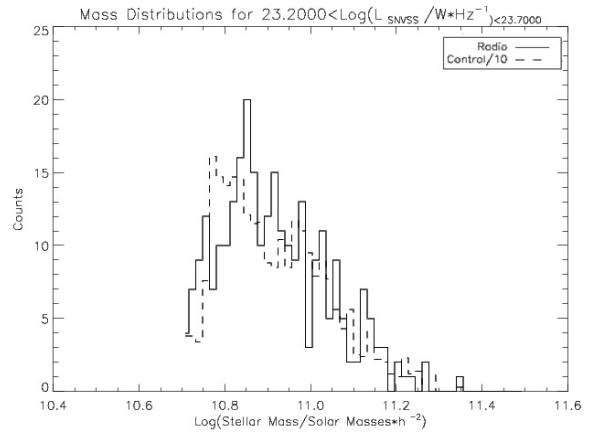
(f) 6th Radio Bin

Figure 3.5: See next page for caption.

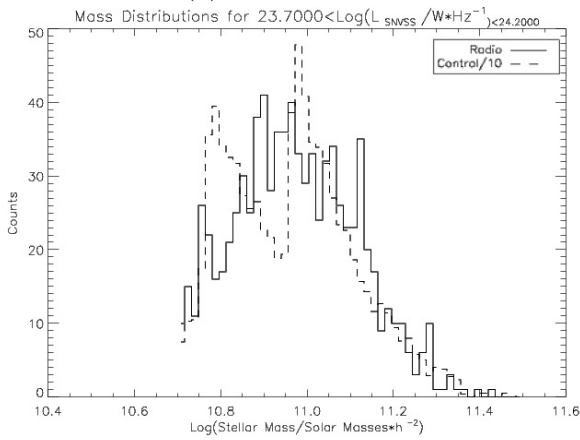
Figure 3.5: (Figure on previous page.) These histograms depict redshift distributions of both the radio samples and their corresponding control samples after redshift matching under the czm matching scheme. The horizontal axes depict redshift, and the vertical axes depict counts within a redshift bin. Note that, for comparison purposes, the count for each control sample have been divided by 10. The solid lines show the radio sample redshift distributions, and the dotted lines show the corresponding control sample redshift distributions. While there are naturally some differences between two corresponding distributions due to the histogram binning being finer than the redshift matching bins, the overall control redshift distributions are similar to their respective radio redshift distributions.



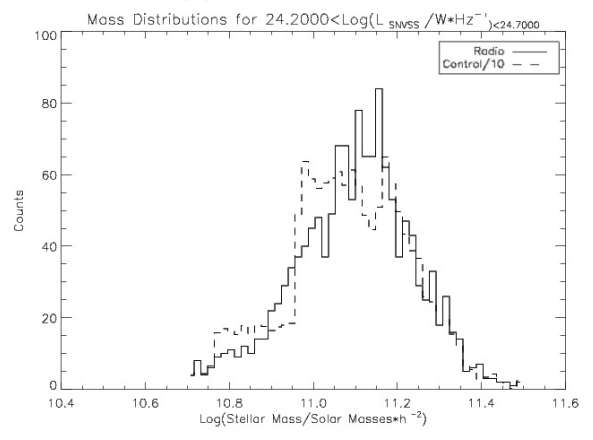
(a) 1st Radio Bin



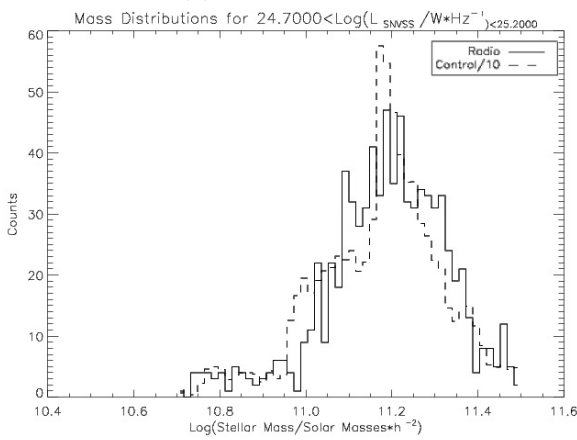
(b) 2nd Radio Bin



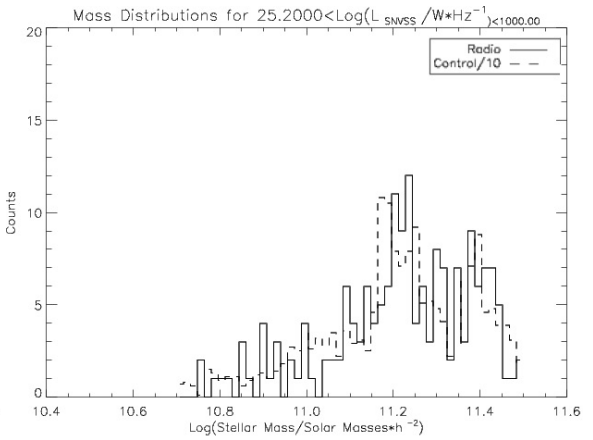
(c) 3rd Radio Bin



(d) 4th Radio Bin



(e) 5th Radio Bin



(f) 6th Radio Bin

Figure 3.6: See next page for caption.

Figure 3.6: (See Figure on previous page.) These histograms depict stellar mass distributions of both the radio samples and their corresponding control samples after matching under the czm matching scheme. The horizontal axes depict logarithm of the stellar masses in solar luminosities/ h^2 , and the vertical axes depict counts within a stellar mass bin. Note that, for comparison purposes, the counts for each control bin have been divided by 10. The solid lines show the stellar mass distributions for the radio samples, and the dotted lines show the distributions for the corresponding control samples. As with the redshift matching, there are naturally some differences between two corresponding distributions due to the histogram binning being finer than the mass matching bins. The overall control mass distributions are similar to their respective radio sample stellar mass distributions.

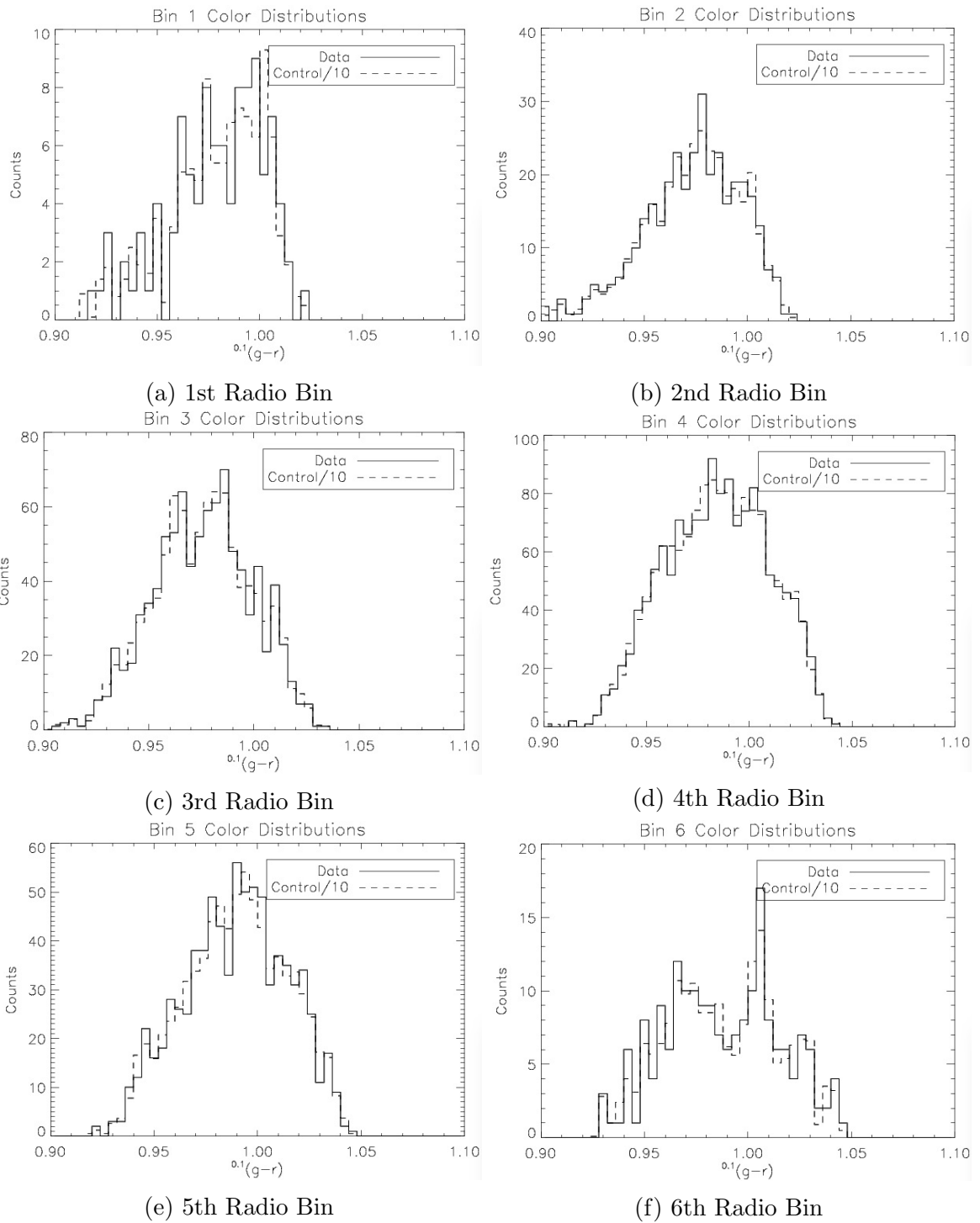


Figure 3.7: See next page for caption.

Figure 3.7: (Figure on previous Page) These histograms show the color distributions of both the radio samples and their corresponding control samples after $^{0.1}(g - r)$ matching radio and control samples under the czm matching scheme. The horizontal axes represent the red-band magnitude subtracted from the green-band magnitude, and the vertical axes depict counts within a stellar mass bin. As with the redshift and stellar mass histograms, the counts for the control bins have been divided by 10 for easy comparison with the radio samples. The solid lines show the radio sample color distributions, and the dotted lines depict the corresponding control sample color distributions.

Chapter 4 Preliminary Results

4.1 Recreating Previous Results

Similar cuts and matching techniques were used to recreate the Best et al. (2005)[OIII] versus radio luminosity plot. Figure 4.1 shows this recreation of the Best et al. (2005) results within the $0.03 < Z < 0.1$ range. Note that our recreation of the results of Best et al. (2005) does not contradict the original paper in that, seemingly, no correlation exists between emission line luminosity and radio luminosity within the lower radio luminosity ranges. However, because the radio AGN energy output is expected to be relatively small at low radio luminosity ranges, it is possible that the non-AGN-powered emission line luminosities are simply overwhelming any AGN-powered emission.

4.2 Differences in Stacked Spectra

We coadded the spectra of galaxies in each radio and control samples to examine any difference in emission line spectra between them. Before stacking, we normalized each spectrum by dividing it by the median flux between 6000\AA and 6100\AA . Figures 4.2 and 4.3 depicts the differences in the stacked normalized spectra between corresponding radio and control samples. The left panels show the stacked spectra for all radio luminosity bins. The right panels show the differences, where we only have significant residual around emission lines. As one can see from the positive flux differences, the radio samples have higher average emission line fluxes than their control samples. The flux differences vary with radio luminosity. However, the trend of how this flux difference vary with radio luminosity is counterintuitive in that it is not monotonic. Both the highest and lowest radio luminosity bins show significant emission line flux differences, more than those shown by the intermediate radio luminosity bins. For several lines, there appears to be a peculiar pattern in that, as one increases in radio luminosity, the emission line flux difference tends to decrease until it reaches a minimum around the third or fourth radio sample. Then, the emission line flux difference tends to increase with radio luminosity, as one would expect for high radio luminosities. As detailed below, we investigated this result through a few statistical measurements.

4.3 Differences in Cumulative Distributions

We examined the differences in cumulative emission line luminosity distributions between the radio and the control samples, as depicted in Figures 4.4 to 4.10). In these plots, the vertical axes show the fraction of galaxies in each control or radio sample with an emission line luminosity at or below the corresponding value on the horizontal axes. The horizontal axis is in logarithmic space. All negative emission line

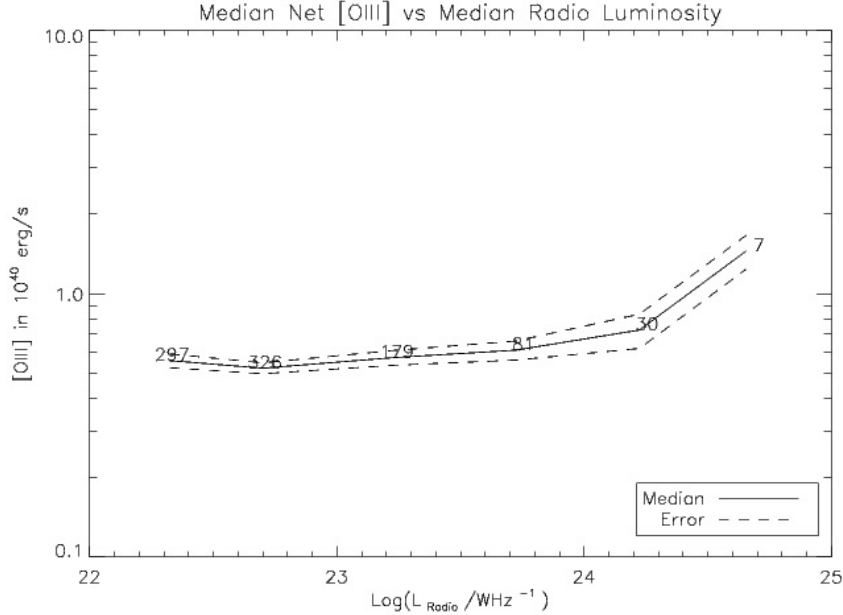
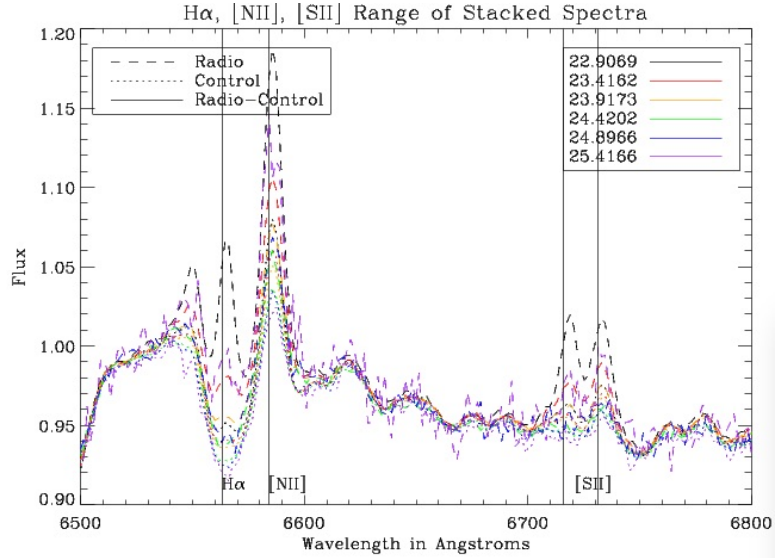


Figure 4.1: This plot shows our efforts to reproduce the Best et al. (2005) [OIII] versus radio luminosity plot. In making this plot, we imposed the same redshift restrictions upon our data which were used in the Best et al. (2005) paper. The horizontal axis shows the logarithm of the radio luminosity in W/Hz . The vertical axis shows the logarithm of [OIII] in 10^{40} erg/s. The solid line represents the [OIII] median plotted against the radio luminosity median for each radio bin. The dashed lines represent the errors in the [OIII] medians.

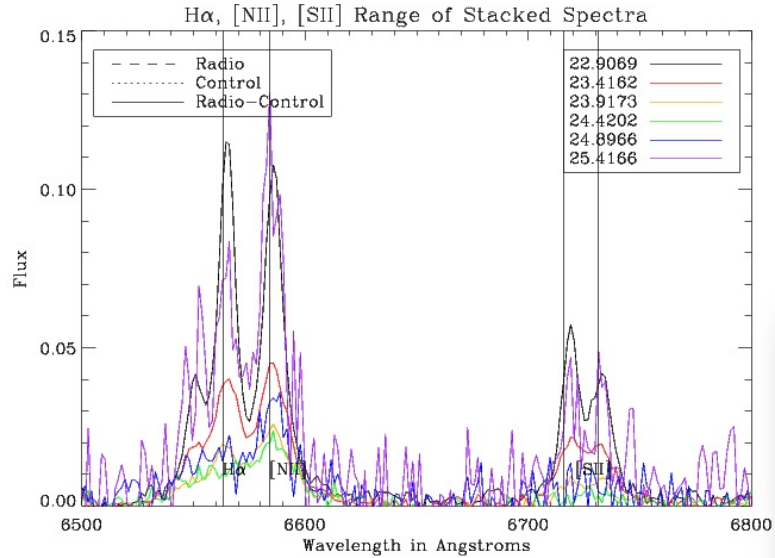
luminosities cannot be displayed, but they are included in the cumulative fractions. This is why all curves appear to start with a positive fraction rather than zero.

As the lower fraction regions of the cumulative curves tend to be noisy, we visually assessed the cumulative profiles near the 50th percentile regions. Paying attention to the difference between each pair of cumulative fraction curves from a radio sample and its corresponding control sample, we can see that the differences are strong for both high (blue and purple curves) and low radio luminosity bins (red and black curves), but are small for the two intermediate luminosity bins (yellow and green curves). Such trend is consistent among all emission lines. This is the same as what we saw above from stacked spectra.

Correlation between AGN-powered emission line luminosity and radio luminosity has been shown before at radio luminosities higher than about 10^{32} erg/s/Hz (or 10^{25} W/Hz) at 1.4 GHz (McCarthy, 1993). Therefore, it is reasonable to see that there is extra line emission in the radio sample than the control sample for the top two radio luminosity bins. It also seems reasonable for this extra emission to decrease in strength with a decreasing radio luminosity as we see in the intermediate radio luminosity bins. However, it is very surprising to see the difference can get stronger again at the low radio luminosities. Could this be explained by small sample size

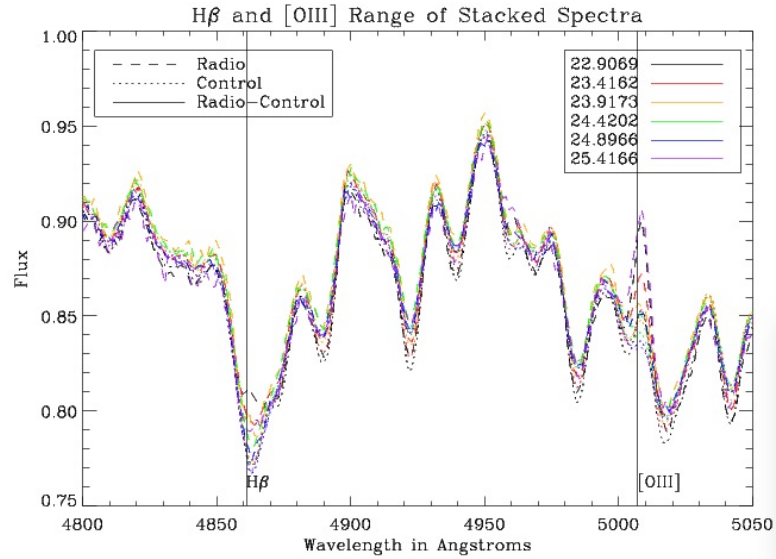


(a) $H\alpha$, [NII], and [SII] Lines

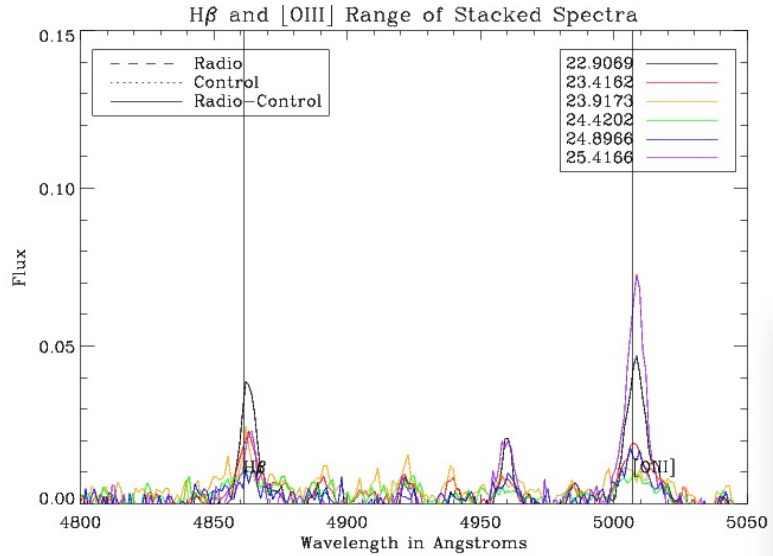


(b) Differences in Lines

Figure 4.2: The upper plot shows the stacked spectra for both the radio and the control samples in one wavelength window around strong emission lines ($H\alpha$, [NII], and [SII]). The vertical axis shows the normalized flux, and the horizontal axis depicts the spectral wavelengths in Angstroms. Emission lines are marked according to their wavelengths. The various colored lines represent specific radio galaxy samples and their corresponding control samples, as indicated in the legends, which associate the colors with the logarithms of median radio luminosities (in WHz^{-1}). The lower panel shows the difference in stacked spectra between the radio and the control samples. The differences should give us an idea of AGN-powered spectra of the samples. Note the flux difference does *not* monotonically increase with radio luminosity.



(a) $H\beta$ and [OIII] Lines



(b) Differences in Lines

Figure 4.3: .

]The upper plot shows the stacked spectra of radio and control samples for the wavelength window including $H\beta$ and [OIII]. The lower plot shows the differences in stacked spectra between radio and control samples. See the caption for 4.2 for details.

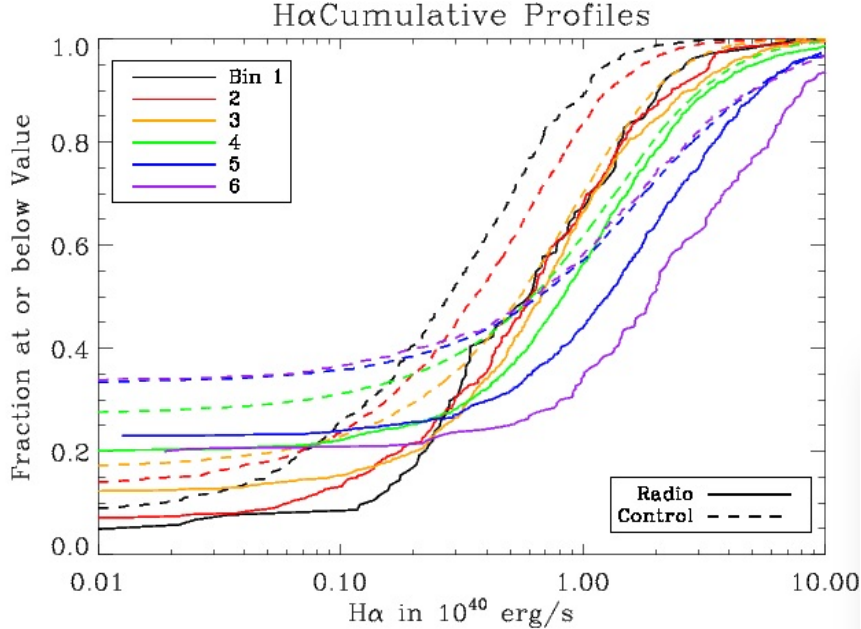


Figure 4.4: This plot depicts the cumulative distributions of $H\alpha$ for the radio and control samples in each luminosity bin. Each panel shows that for a different emission line. The y-axis shows the fraction of galaxies at or below a given emission line luminosity, and the horizontal axes depict emission line luminosities in 10^{40} erg/s . The radio samples are shown by solid lines, with each color represent a different radio luminosity bin (which are labeled in ascending order according to radio luminosity). Their corresponding control samples are represented by dashed lines with the same color. Note the differences between the radio and the control samples are largest for the high and low luminosity bins but are small for the intermediate luminosity bins.

statistics?

To test the robustness of the difference between the radio and the control samples, we conducted simulations to see how likely it is to have a median emission line luminosity as large as that in the radio sample if the radio sample were drawn from the same distribution as the control sample. For each radio sample, we randomly drew from its corresponding control sample the same number of galaxies as there were in the radio sample. Then, we compared the median emission line luminosity of this sample with that of the radio sample. We conducted such random drawings 10,000 times and checked the fraction of times the given radio samples had larger medians than those of the randomly-drawn control subsamples. The results are tabulated in Table 4.1 for each radio luminosity bin and for each emission line. In most cases, we can rule out the hypothesis that the radio sample is drawn from the same distribution as the control sample with a confidence level of 99% or better. Notable exceptions are found for [OII] in the intermediate radio luminosity bins. [OII] is actually a fairly strong line among these quiescent galaxies. It is usually stronger than $H\beta$, [OIII], and [OI]. Thus this cannot be explained by insufficient signal-to-noise ratios. A remaining explanation is that radio AGN with intermediate luminosity has very little or nearly

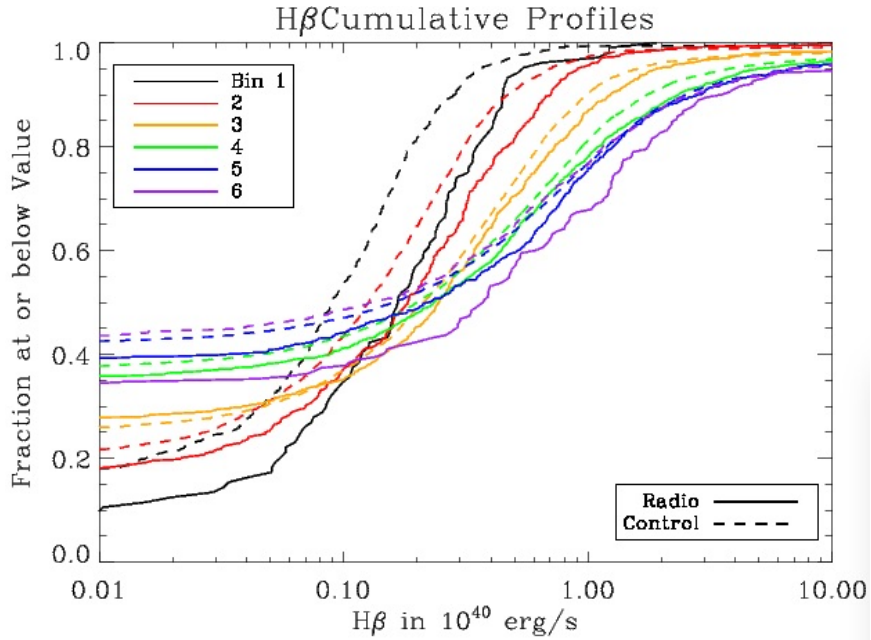


Figure 4.5: This plot depicts the cumulative distributions of $H\beta$ for the radio and control samples in each luminosity bin. See the caption of Figure 4.4 for thorough descriptions of the plot.

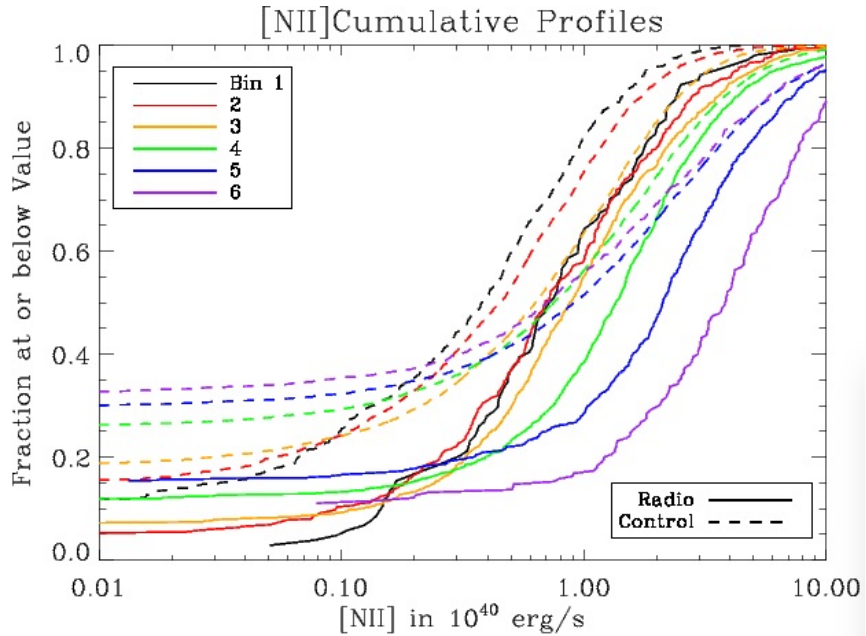


Figure 4.6: This plot depicts the cumulative distributions of $[NII]$ for the radio and control samples in each luminosity bin. See the caption of Figure 4.4 for thorough descriptions of the plot.

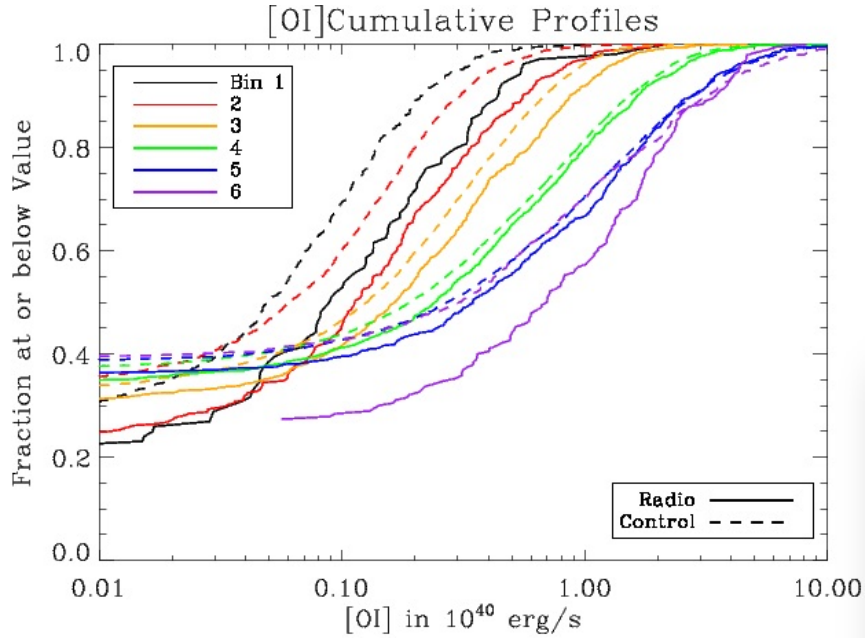


Figure 4.7: This plot depicts the cumulative distributions of [OI] for the radio and control samples in each luminosity bin. See the caption of Figure 4.4 for thorough descriptions of the plot.

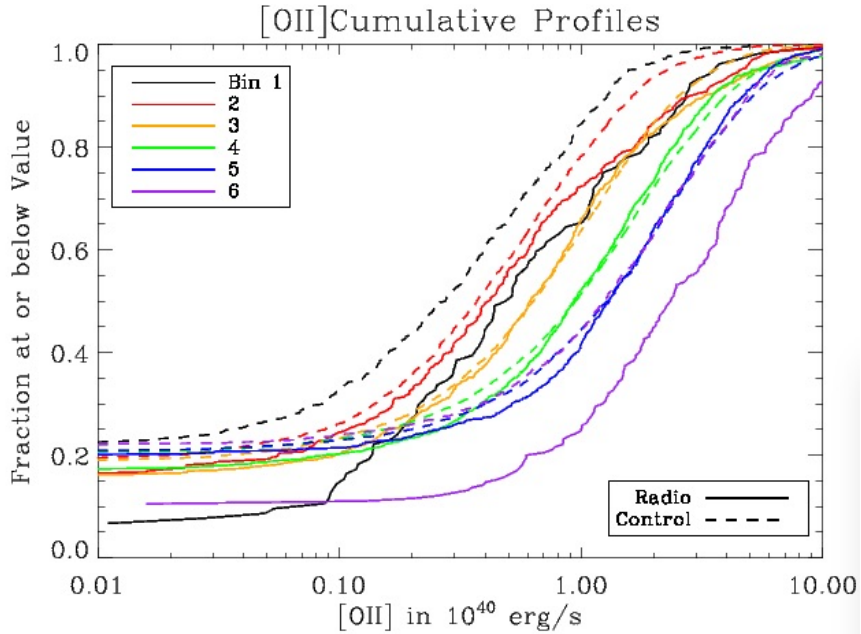


Figure 4.8: This plot depicts the cumulative distributions of [OII] for the radio and control samples in each luminosity bin. See the caption of Figure 4.4 for thorough descriptions of the plot.

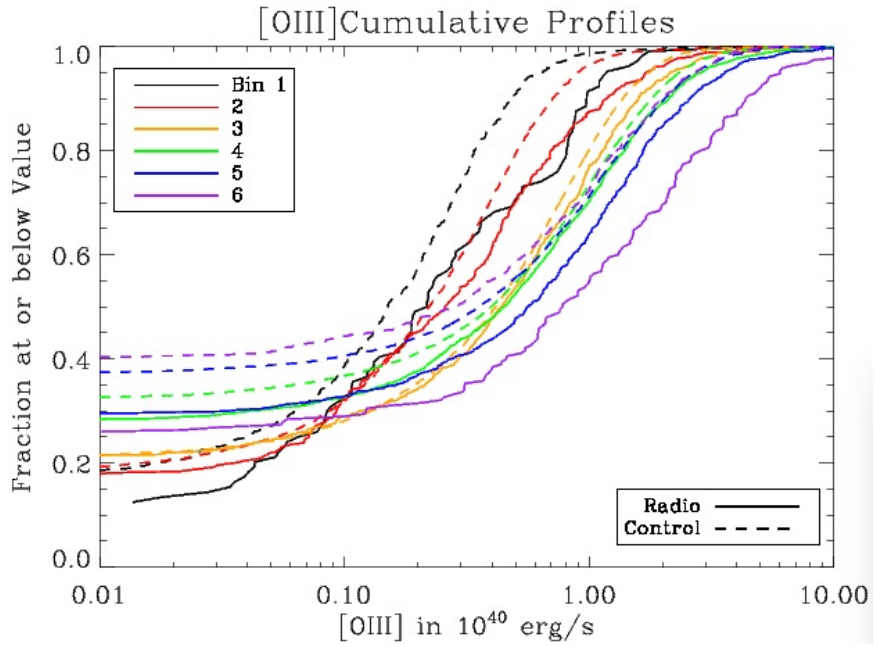


Figure 4.9: This plot depicts the cumulative distributions of [OIII] for the radio and control samples in each luminosity bin. See the caption of Figure 4.4 for thorough descriptions of the plot.

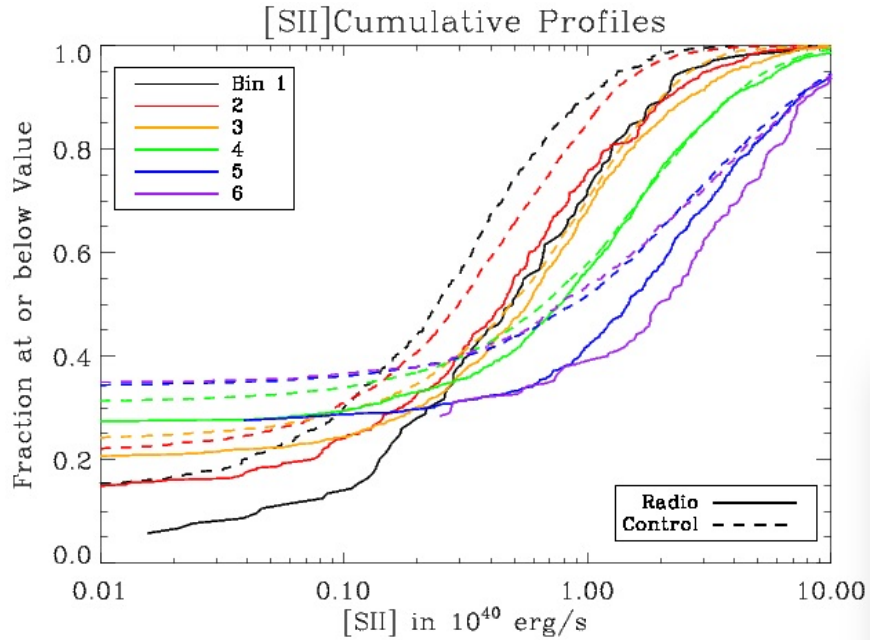


Figure 4.10: This plot depicts the cumulative distributions of [SII] for the radio and control samples in each luminosity bin. See the caption of Figure 4.4 for thorough descriptions of the plot.

Table 4.1: Percentage of times that Medians of the randomly-drawn control subsets are smaller than the medians of the corresponding radio sample.

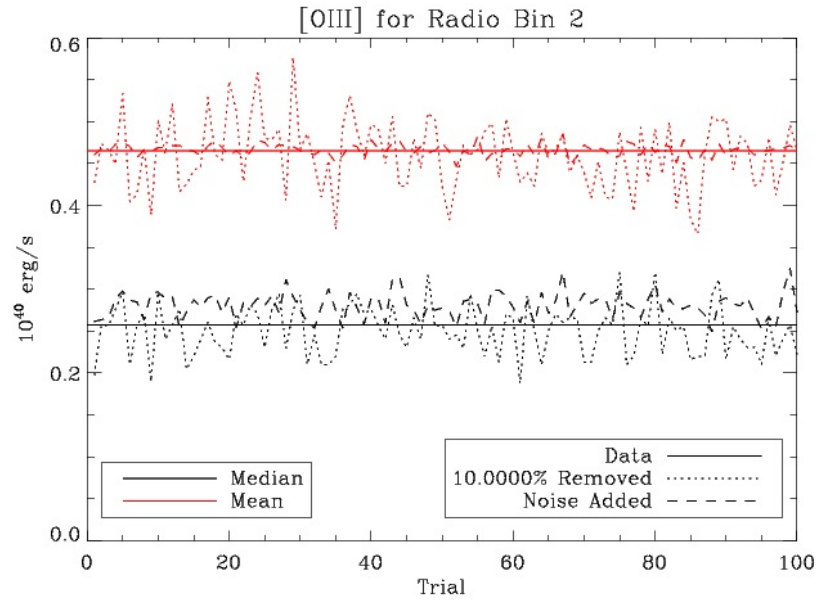
Radio Bin	$H\alpha$	$H\beta$	[NII]	[SII]	[OI]	[OII]	[OIII]
1 (lowest L)	100.0	100.0	100.0	100.0	99.9	100.0	99.4
2	100.0	100.0	100.0	100.0	100.0	85.5	96.9
3	100.0	99.5	100.0	99.4	100.0	21.6	93.4
4	100.0	97.8	100.0	99.3	99.8	43.8	97.5
5	100.0	92.8	100.0	100.0	97.8	64.8	100.0
6 (highest L)	100.0	99.4	100.0	100.0	100.0	100.0	100.0

no excess in [OII] emission compared to radio-faint galaxies with similar properties.

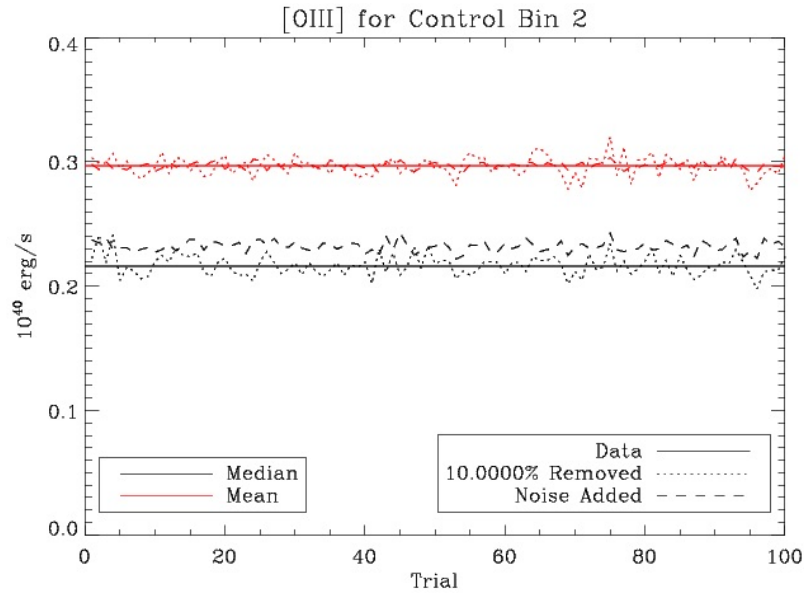
4.4 Quantifying the Differences

After verifying the existence of a spectral differences between radio and control samples, the next logical step is to quantify the differences and search for patterns. When comparing samples, two obvious parameters—median and mean—emerge. While both are valid measures, we considered stability with regard to sample completeness and noise in determining which to use. To test the stability of mean and median with regard to noise, random Gaussian noise was added to both radio and control emission line luminosities in a series of 100 trials, and the new trial means and medians were plotted in relation to the original means and medians, as seen in Figures 4.11 and 4.12. To test these stabilities with regard to completeness, 10% of each radio and control sample were randomly removed (with replacement) during 100 trials. The resulting means and medians were also plotted in Figures 4.11 and 4.12. Most of the time (as would be expected), both parameters appear more stable in the larger control samples than in the smaller radio samples. Moreover, the median generally seemed to vary as much as or less than the mean does in the completeness trials. In the noise tests, the medians and means seem to have roughly equivalent stability, as judged by the amount that each parameter varied. However, we must note that adding noise to these distributions introduces a positive shift in several of the medians. Thus, we initially chose the median as our parameter by which to evaluate the differences between distributions with the understanding that we would eventually need to account for the effects of noise on medians.

Given their obvious skewness, the emission line luminosity distributions of all these samples are very different from Gaussian distributions. However, they are similar to lognormal distributions, with some noise added. We show an example of this in Figure 4.13. Because of this, we needed to be careful with the choice of statistics. The median seemed to be a more robust statistics than the mean because it is less sensitive overall to factors such as incompleteness and noise. However, the median has significant drawbacks when dealing with lognormal distributions or similar asymmetric distributions. The first issue is that adding noise to a lognormal distribution will introduce a non-zero systematic offset to its median because lognormal distributions

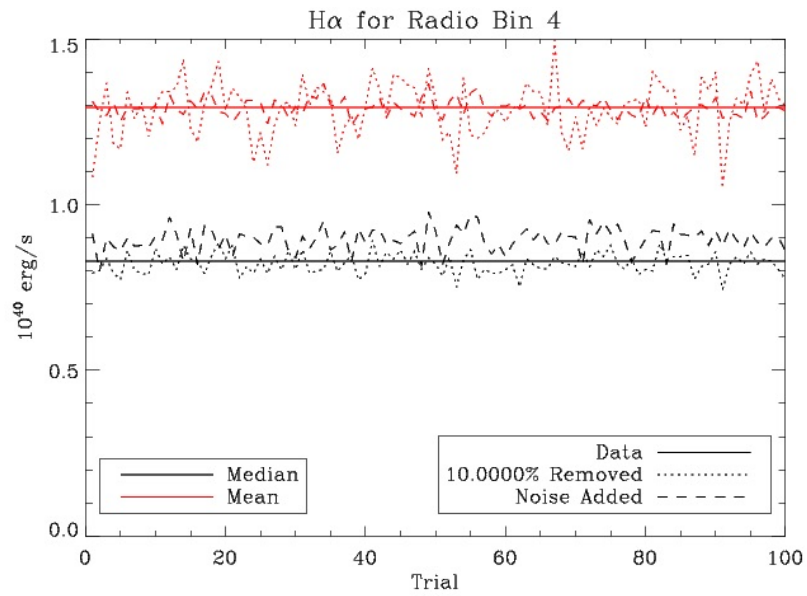


(a) Radio Bin 2 [OIII] Stability Test

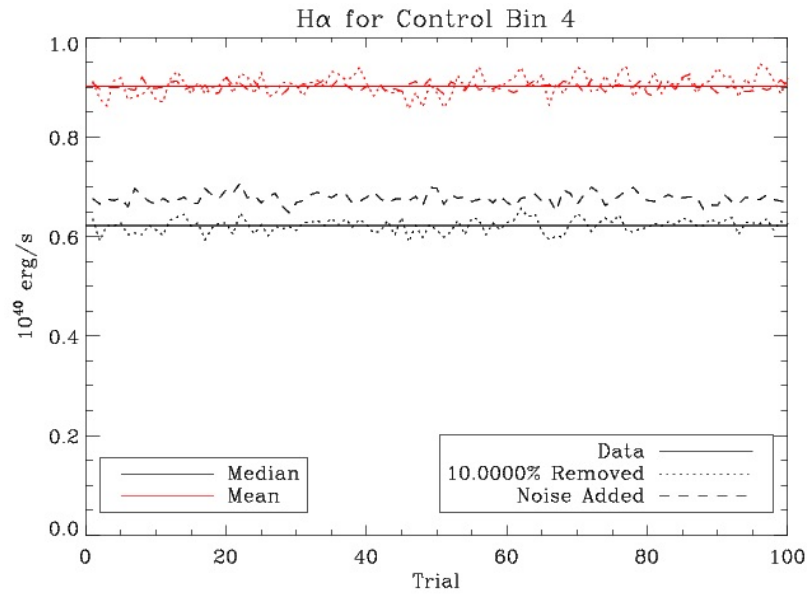


(b) Control Bin 2 [OIII] Stability Test

Figure 4.11: These plots depict the results of the stability tests for radio and control sample [OIII] means and medians. The vertical axes show emission line luminosities in 10^{40} erg/s , and the horizontal axes give the trial numbers. The red lines represent means, and the black represent medians. The solid horizontal lines show the original parameters (median and mean) of each radio or control sample. The dotted lines indicate the parameters when 10% of the sample is randomly removed (with replacement) at each trial. The dashed line shows what happens when random Gaussian noise is added to the samples.



(a) Radio Bin 4 $H\alpha$ Stability Test



(b) Control Bin 4 $H\alpha$ Stability Test

Figure 4.12: These plots depict the results of the stability tests for radio and control sample $H\alpha$ luminosity means and medians. The plot legend is the same as that of Figure 4.11

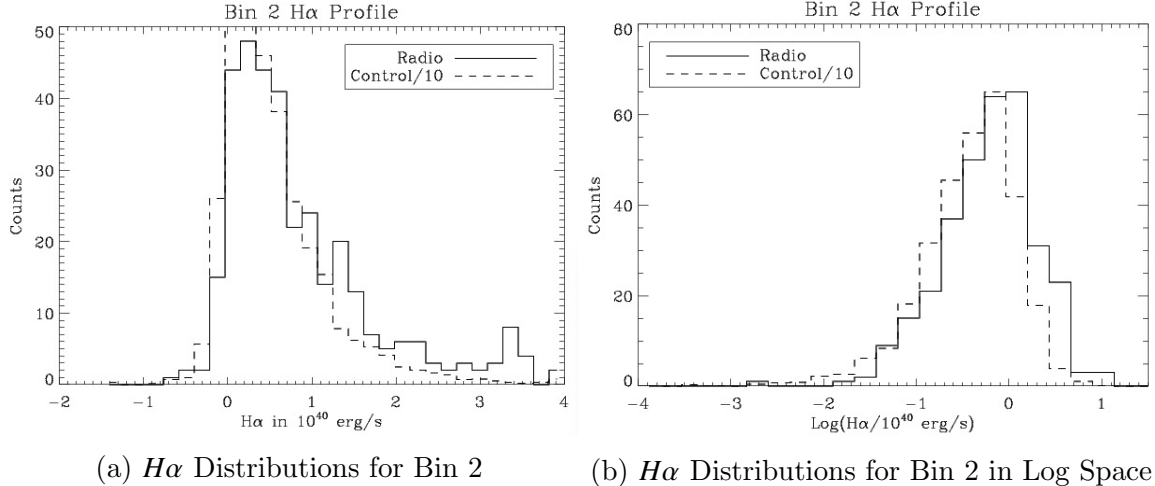


Figure 4.13: These plots depict histograms of the $H\alpha$ luminosity distributions for Bin 2. The horizontal axis of the left plot shows $H\alpha$ in 10^{40} erg/s, while the horizontal axis of the right plot shows luminosity in terms of $\log(H\alpha/10^{40} \text{ erg/s})$. The vertical axes show the counts for the histograms. The solid lines portray the histograms for the Bin 2 radio sample. The dashed lines show the histograms for the corresponding control sample, albeit with the counts divided by 10 so as to be more easily compared to the radio sample. Note the obvious skewness of the histograms on the left.

are not symmetric. Therefore, there are always more points that scatter to higher values than there are that scatter downwards across the intrinsic median value. This effect can be seen in Figures 4.11 and 4.12, in which the noise-added medians are consistently higher than the original medians. The second issue is that, when you add two lognormal distributions together, the medians do not add up to the median of the final distribution. When the two lognormal distributions have comparable values, the final lognormal distribution tend to have a larger median than the sum of the medians of the two original distributions. However, the mean is somewhat sensitive to noise, sample completeness, and stochastic sampling at the right tail of the distribution where the data points can have very large values. Thus, the mean is not perfectly desirable, either.

In the effort of quantifying the difference, the medians of the radio samples' emission line luminosities were subtracted from those of the corresponding control samples. In Figures 4.14 through 4.20, we show the difference in medians between the radio samples and their corresponding control samples, as a function of radio luminosity, for the six different emission lines. However, as discussed above in the drawbacks for medians, these should NOT be interpreted as the medians of excess line emissions radio-AGN have relative to their radio-faint counterparts. We show this simply to visually illustrate the surprising trend we found in the cumulative distribution plots. The error bars are obtained from quadratic combinations of the uncertainty on the individual medians. We disclose that the apparent differences in medians could be larger than the intrinsic differences due to the phenomenon of noise increasing medians (more so in the smaller radio samples than in the larger control samples).

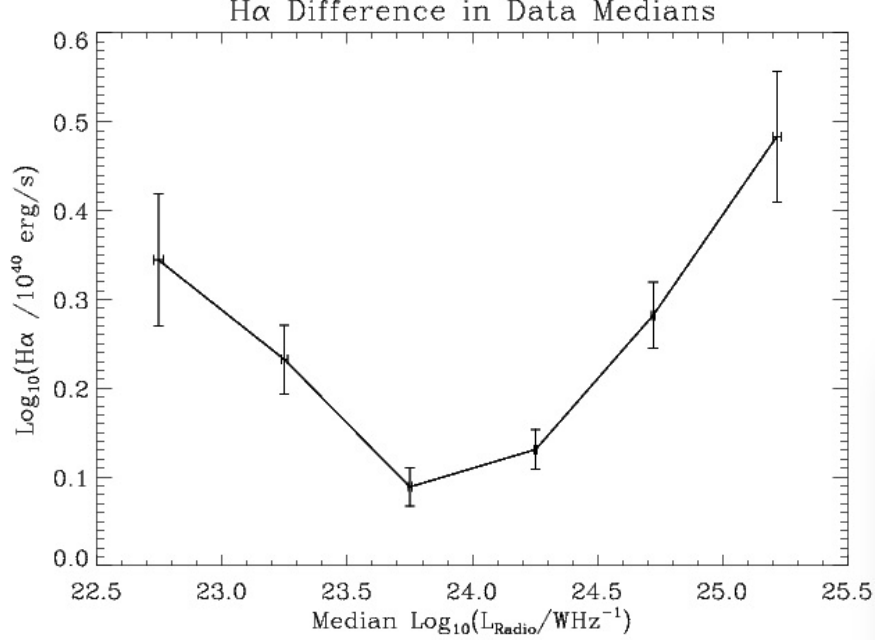


Figure 4.14: This plot show the differences in $H\alpha$ medians between radio samples and their corresponding control samples. The horizontal axes shows logarithm of the median radio luminosities (in W/Hz) of the radio samples. The vertical axes show the differences of emission line luminosity medians in 10^{40} erg/s . The error bars illustrate the propagated uncertainties in the median difference.

Notice that, even considering the error bars on the differences in medians, many lines show an interesting pattern of having the distances of emission line medians greater at the upper and lower ends of the radio luminosity ranges and smaller near the middle of the radio luminosity ranges. This pattern is striking in [OII], which shows significant differences in medians for the first and last radio bins, but not for the middle bins. $H\alpha$, [NII], and [SII] also show some degree of the "dipping" pattern while retaining some differences in medians for the middle bins. [OIII] seems more ambiguous. While it seems possible that an underlying "dipping" pattern could exist with [OIII] as well, the preliminary differences in medians are fairly consistent with no correlation between median differences and radio luminosity until approaching $10^{24.3} \text{ W}/\text{Hz}$, at which point a positive correlation becomes apparent.

4.5 Statistically Extracting the Excess Line Emission from Radio-AGN

In light of the interesting median patterns, we would like to extract the distribution of the excess line emission associated with radio-AGN by subtracting the distribution of the control sample from the distribution of the radio sample. A naive approach would be to simply calculate the means (M_r and M_s) and standard deviations (S_r and S_s) of the radio and control samples before plugging them into the following general distribution-adding formulas:

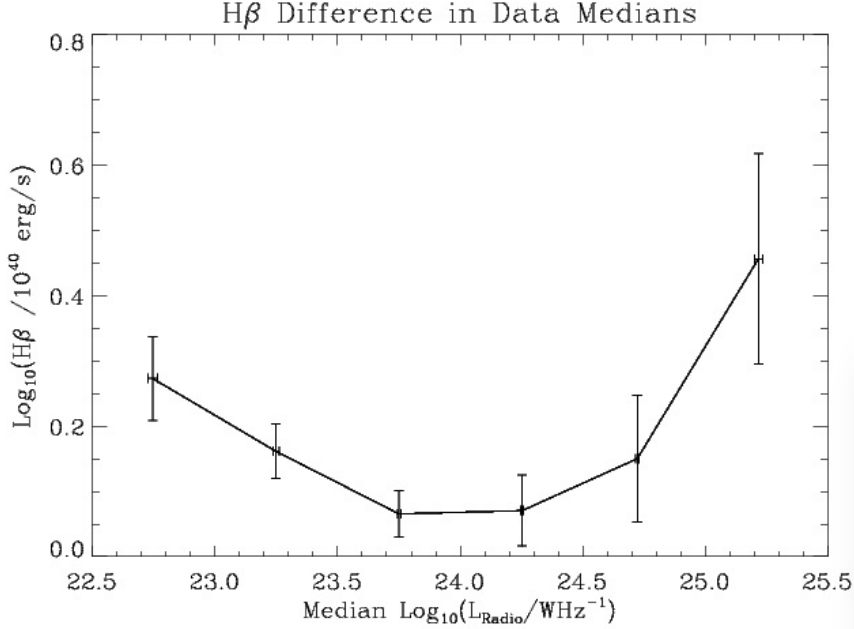


Figure 4.15: This plot show the differences in $H\beta$ medians between radio samples and their corresponding control samples. The horizontal axes shows logarithm of the median radio luminosities (in W/Hz) of the radio samples. The vertical axes show the differences of emission line luminosity medians in 10^{40} erg/s . The error bars illustrate the propagated uncertainties in the median difference.

$$M_{agn} = M_r - M_s \quad (4.1)$$

$$S_{agn} = \sqrt{S_r^2 - S_s^2} \quad (4.2)$$

These AGN-associated mean emission line luminosities (along with spreads of $M_{agn} \pm S_{agn}$) were plotted against the mean radio luminosities of each radio sample in Figures 4.21 through 4.31. While some of the AGN emission line means seem to suggest a pattern of increasing emission luminosities toward higher radio luminosities, the spreads (standard deviations) are often wide. In fact, the standard deviation is larger than the mean for many of the lines and bins, despite relatively few galaxies showing negative emission line luminosities. This sometimes occurs as a byproduct of skewness in the distributions. In short, this simplistic approach fails because it doesn't account for obvious skewness in the distributions, which can be seen in the histograms of Figure 4.13. Secondly, this simplistic approach fails to extract the AGN-powered distributions because, on first glance, a few of the control samples have larger standard deviations than their corresponding radio samples. This results in imaginary S_{agn} values (located by missing vertical error bars in Figures 4.21 through 4.31) and is unphysical if the control samples accurately represent the stellar contributions. This problem likely arises from too much noise in the measurements. Despite the problems with this straight-forward approach, the means of emission lines like [OIII] and [SII]

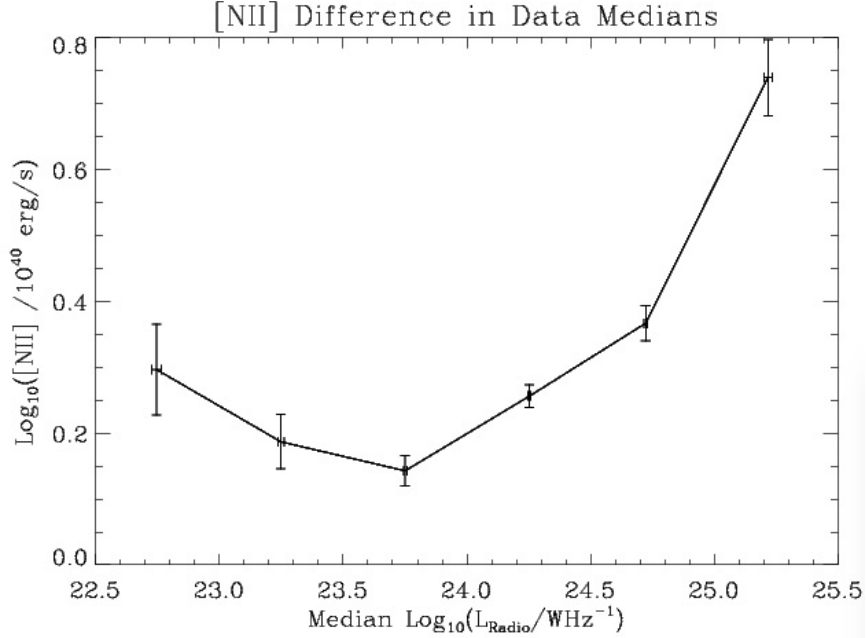


Figure 4.16: This plot show the differences in [NII] medians between radio samples and their corresponding control samples. The horizontal axes shows logarithm of the median radio luminosities (in W/Hz) of the radio samples. The vertical axes show the differences of emission line luminosity medians in 10^{40} erg/s . The error bars illustrate the propagated uncertainties in the median difference.

show intriguing "dipping" patterns in log space. One might wonder if the statistical spreads could be reduced in order to more-clearly define this pattern, especially since similar patterns were noted among the medians (as in Figures 4.14 through 4.20. For these reasons, we attempted more sophisticated techniques to extract the AGN-powered distributions.

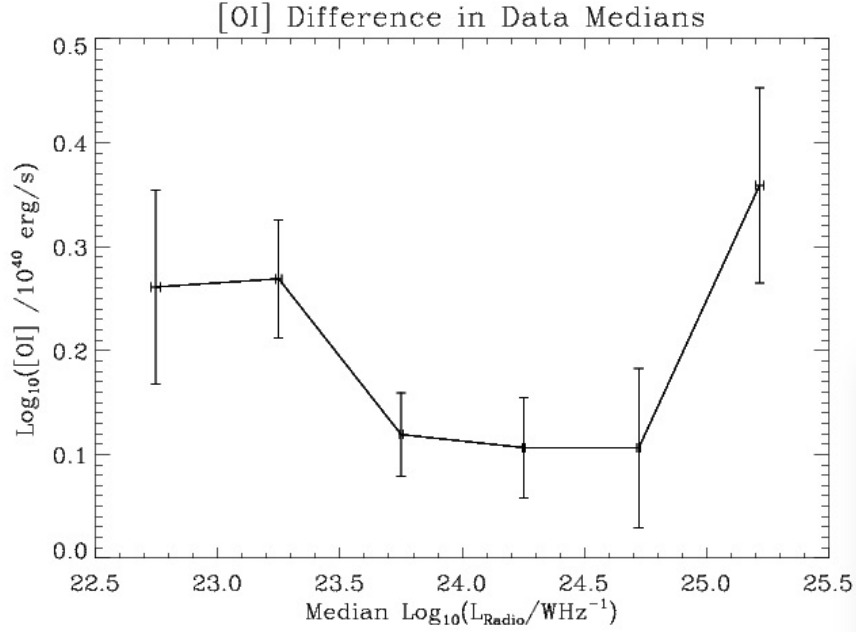


Figure 4.17: This plot show the differences in [OI] medians between radio samples and their corresponding control samples. The horizontal axes shows logarithm of the median radio luminosities (in W/Hz) of the radio samples. The vertical axes show the differences of emission line luminosity medians in 10^{40} erg/s . The error bars illustrate the propagated uncertainties in the median difference.

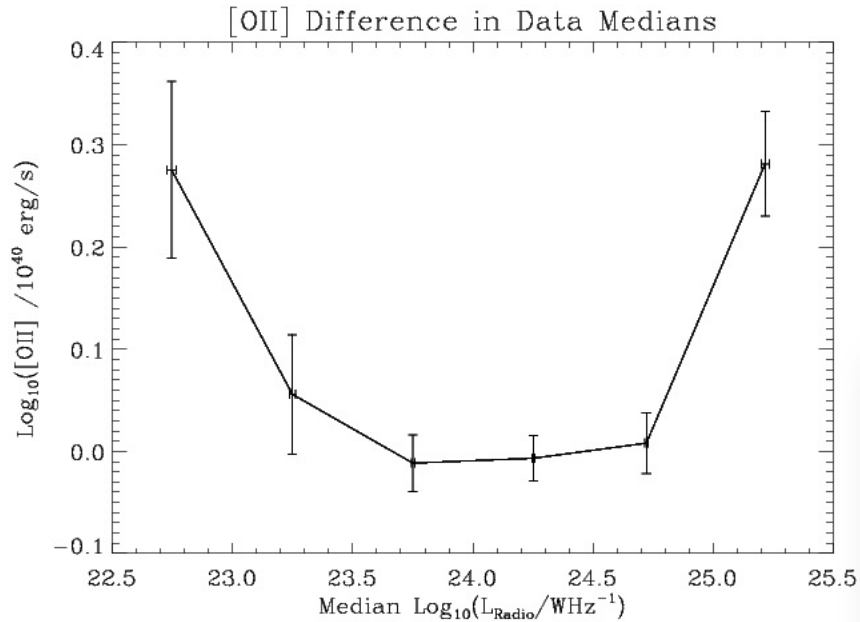


Figure 4.18: This plot show the differences in [OII] medians between radio samples and their corresponding control samples. The horizontal axes shows logarithm of the median radio luminosities (in W/Hz) of the radio samples. The vertical axes show the differences of emission line luminosity medians in 10^{40} erg/s . The error bars illustrate the propagated uncertainties in the median difference.

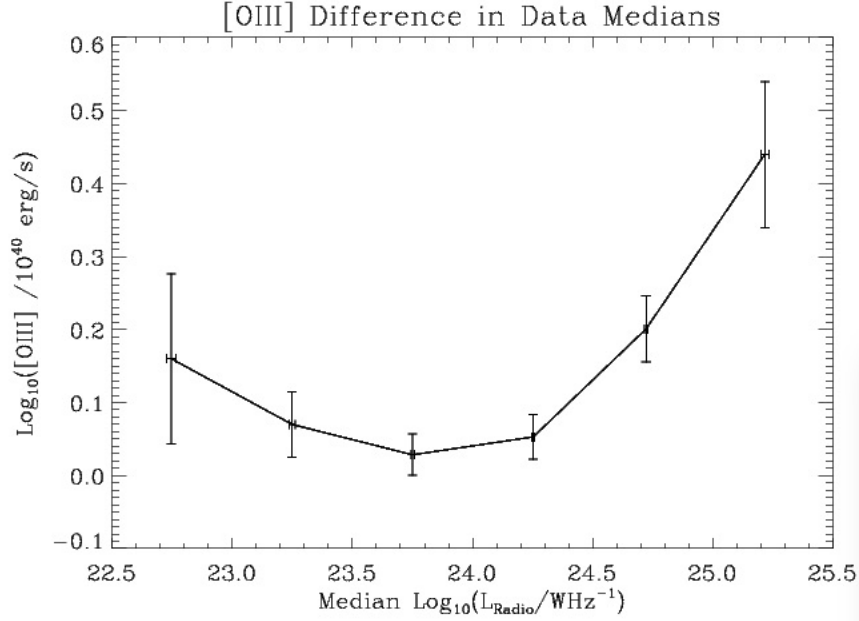


Figure 4.19: This plot show the differences in [OIII] medians between radio samples and their corresponding control samples. The horizontal axes shows logarithm of the median radio luminosities (in W/Hz) of the radio samples. The vertical axes show the differences of emission line luminosity medians in 10^{40} erg/s . The error bars illustrate the propagated uncertainties in the median difference.

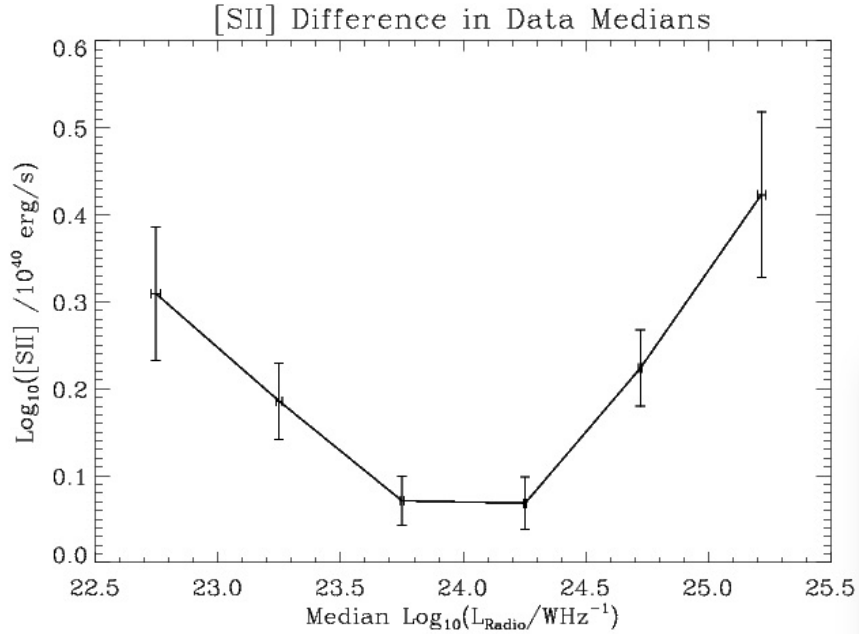


Figure 4.20: This plot show the differences in [SII] medians between radio samples and their corresponding control samples. The horizontal axes shows logarithm of the median radio luminosities (in W/Hz) of the radio samples. The vertical axes show the differences of emission line luminosity medians in 10^{40} erg/s . The error bars illustrate the propagated uncertainties in the median difference.

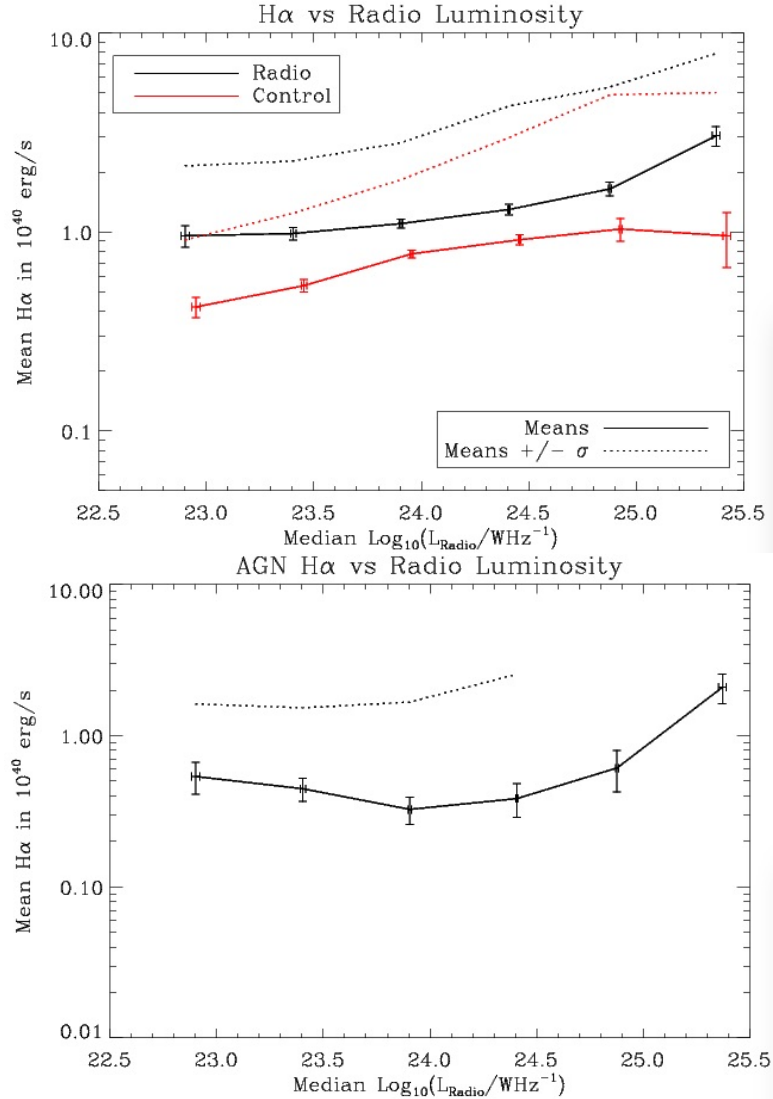


Figure 4.21: These images show the mean $H\alpha$ plotted against the median radio luminosity for each radio bin. The horizontal axes show the logarithm of radio luminosity in W/Hz, while the vertical axes display the logarithms emission line luminosities in erg/s. As indicated by the legend, the upper plot shows the radio sample means connected by solid a black line, whereas the control sample means are connected by a solid red line and are slightly offset along the horizontal axes (for easy viewing). The solid line in the lower plot shows the AGN-powered emission line means as derived by simplistic statistical subtraction of control distributions from the radio sample distributions. The error bars represent the statistical errors in means. The dotted lines represent one standard deviation symmetrically placed above and below the means. These plots are in log scale to distinguish the patterns in data, which has the side effect of hiding the bottom standard deviation lines. However, note that missing upper standard deviation bounds on the AGN-powered distribution plot indicate an inability to find a physically-meaningful standard deviation due to the control sample standard deviation being larger than that of the radio distribution.

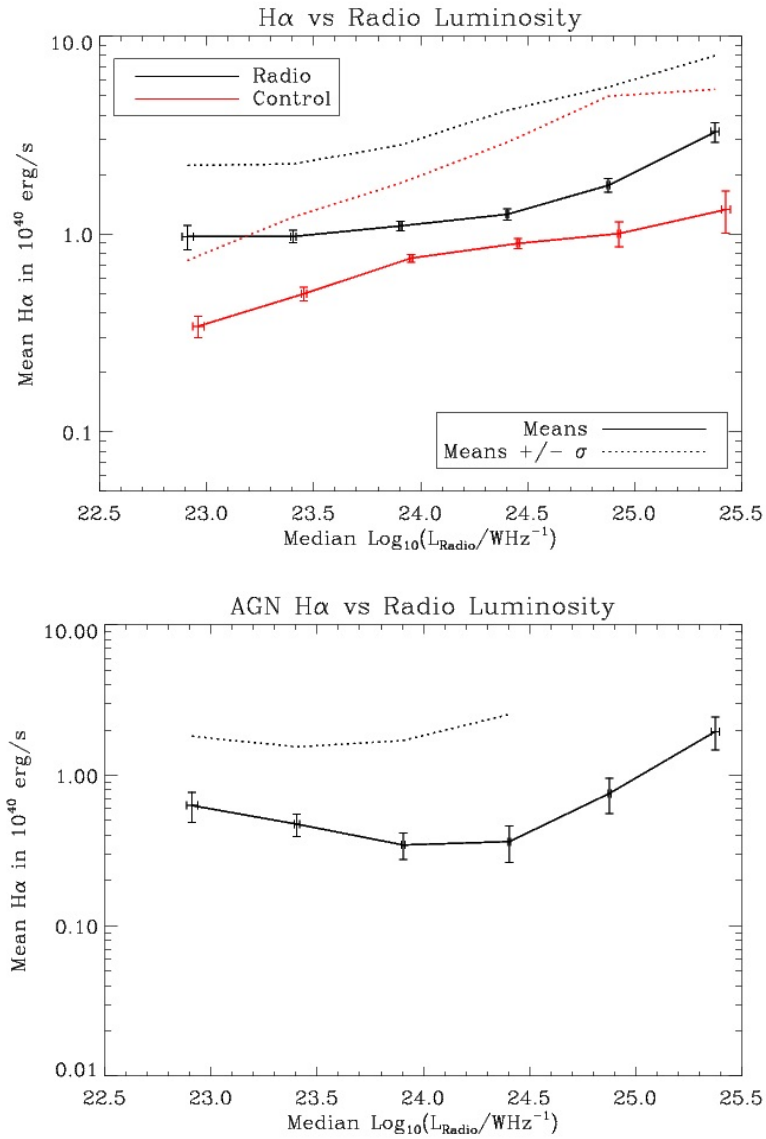


Figure 4.22: These images show the mean $H\alpha$ plotted against the median radio luminosity for each radio bin under the czv matching scheme. Compare to Figures 4.21 and 4.23, which were created under the czm and czmv matching schemes, respectively.

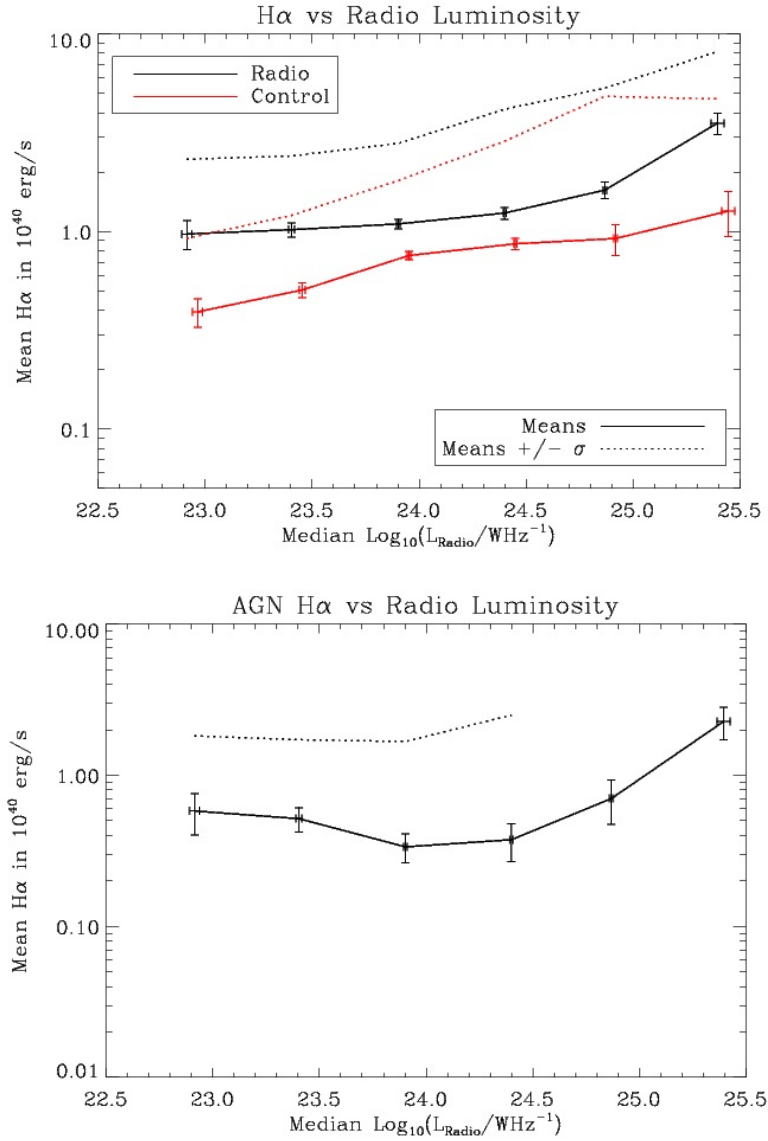


Figure 4.23: These images show the mean $H\alpha$ plotted against the median radio luminosity for each radio bin under the czmv matching scheme. Compare to Figures 4.21 and 4.22, which were created under the czm and czv matching schemes, respectively.

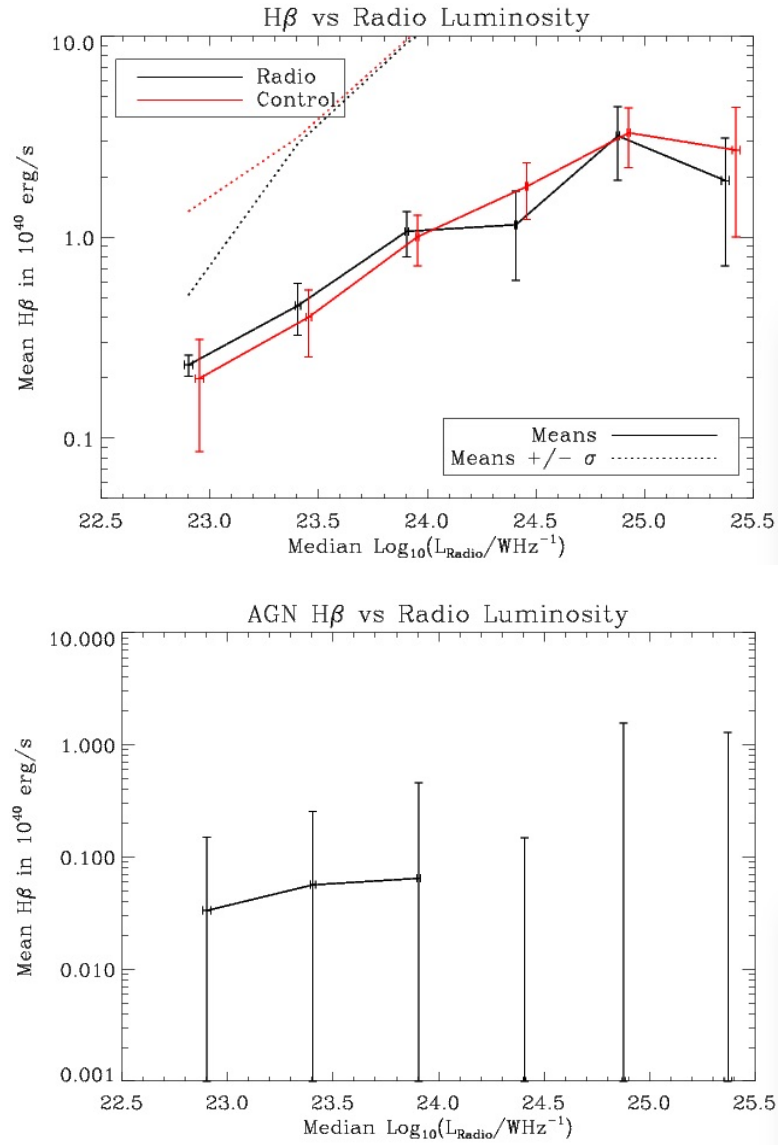


Figure 4.24: These images show the mean $H\beta$ plotted against the median radio luminosity for each radio bin. See the caption for Figure 4.21 for further plot details.

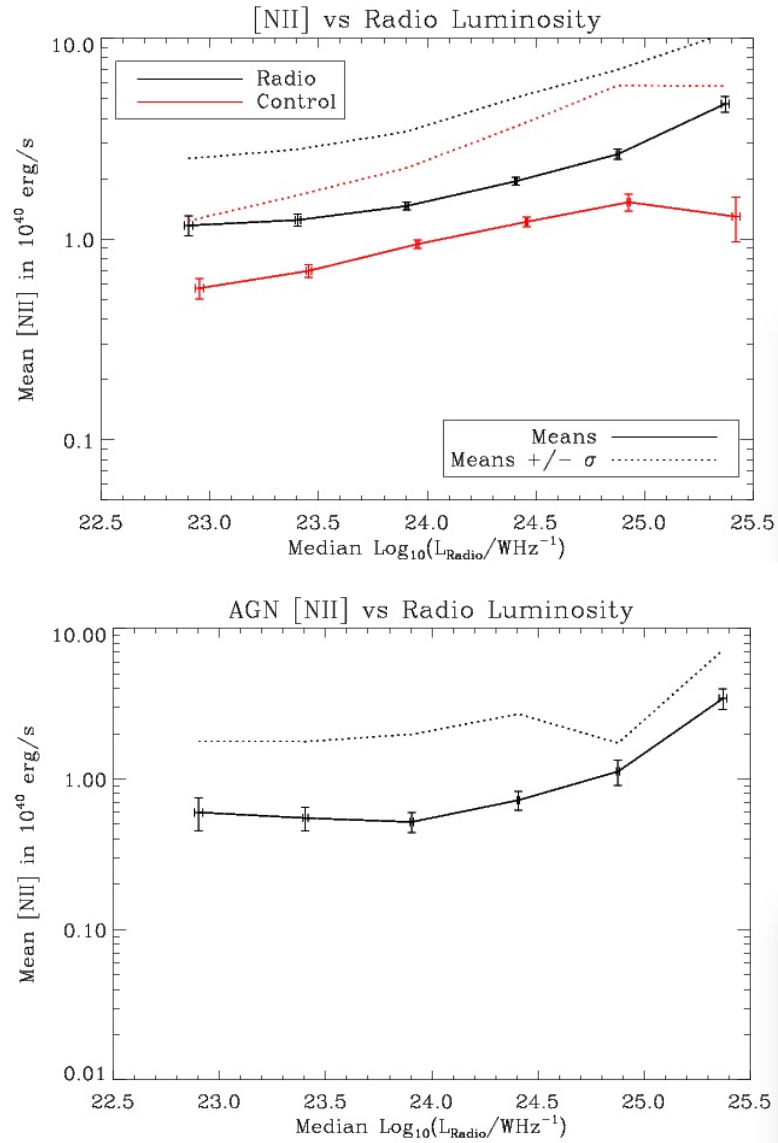


Figure 4.25: These images show the mean [NII] plotted against the median radio luminosity for each radio bin. See the caption for Figure 4.21 for further plot details.

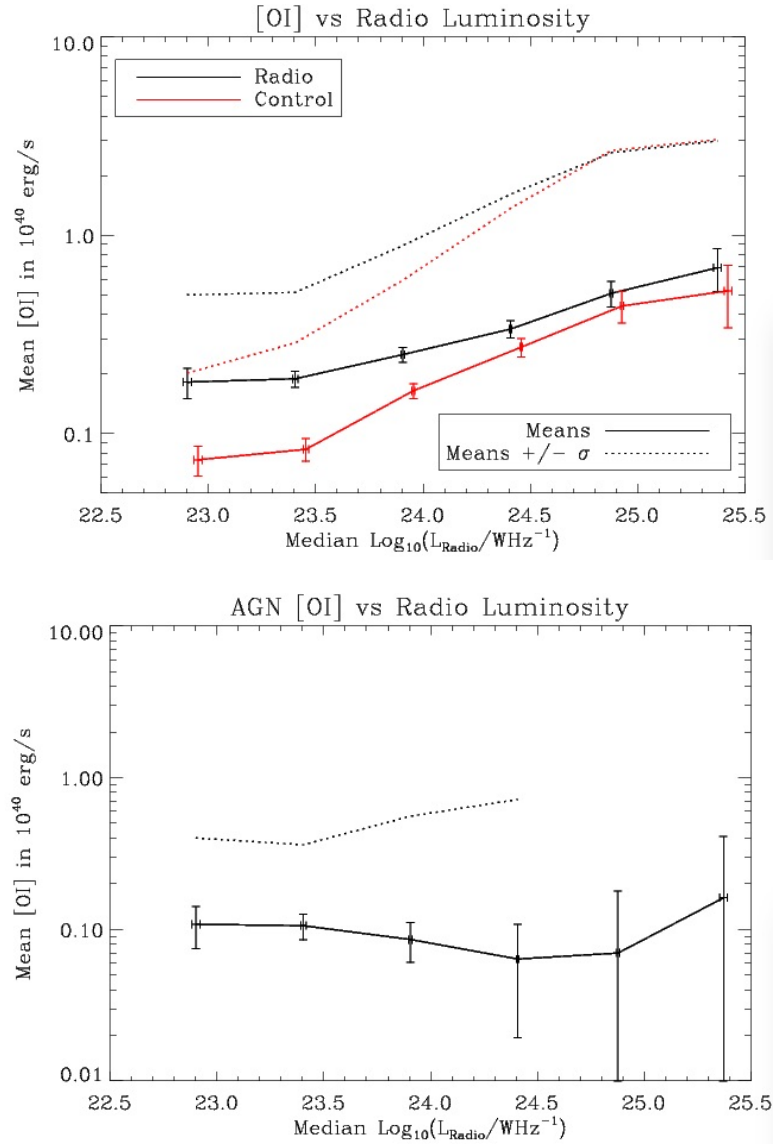


Figure 4.26: These images show the mean [OI] plotted against the median radio luminosity for each radio bin. See the caption for Figure 4.21 for further plot details.

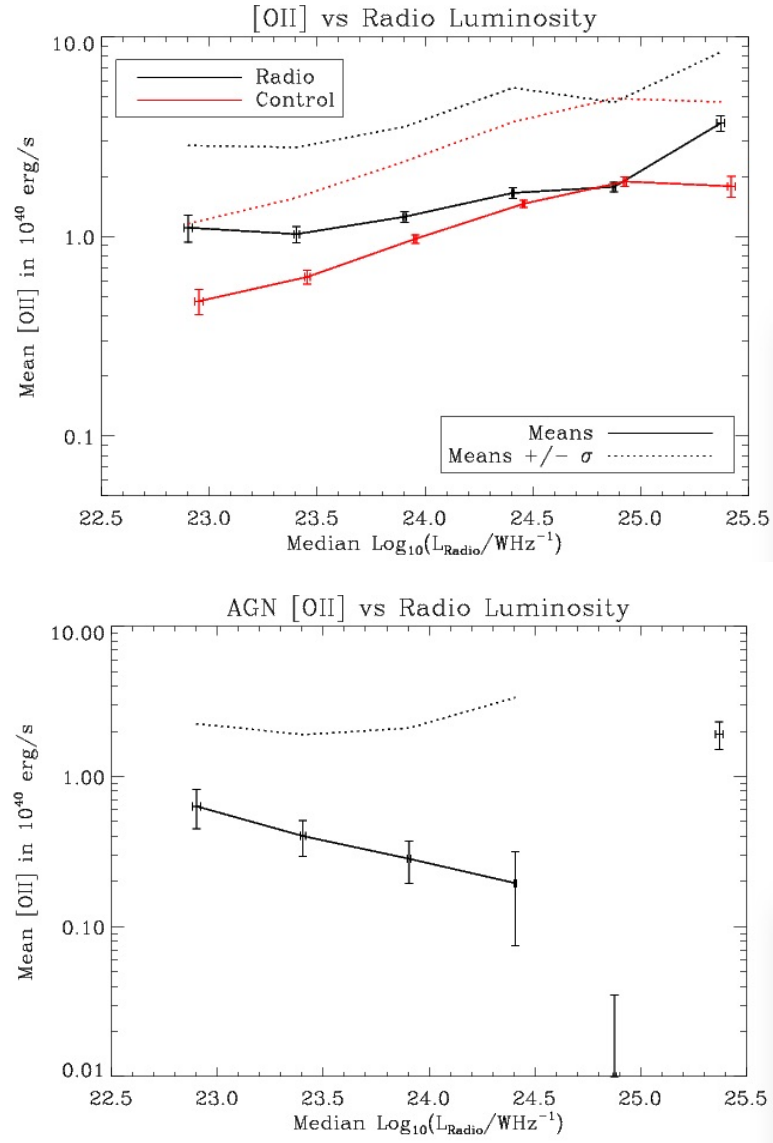


Figure 4.27: These images show the mean [OII] plotted against the median radio luminosity for each radio bin. See the caption for Figure 4.21 for further plot details.

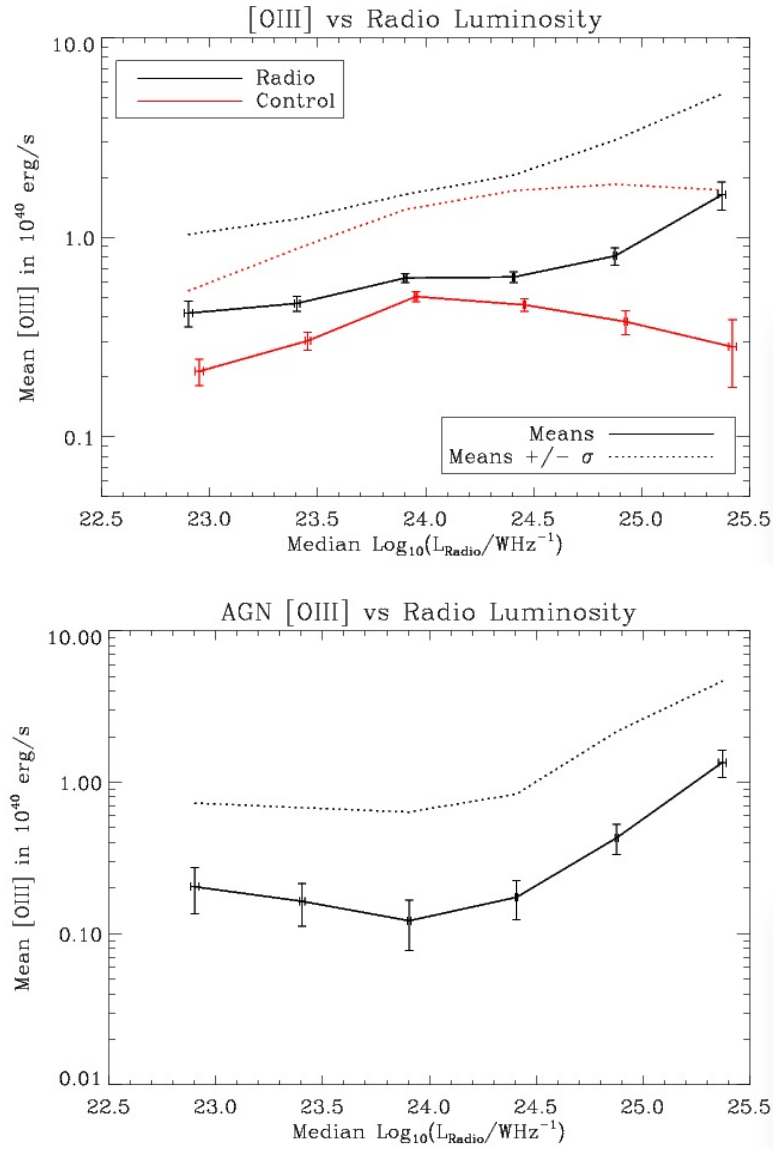


Figure 4.28: These images show the mean [OIII] plotted against the median radio luminosity for each radio bin. See the caption for Figure 4.21 for further plot details.

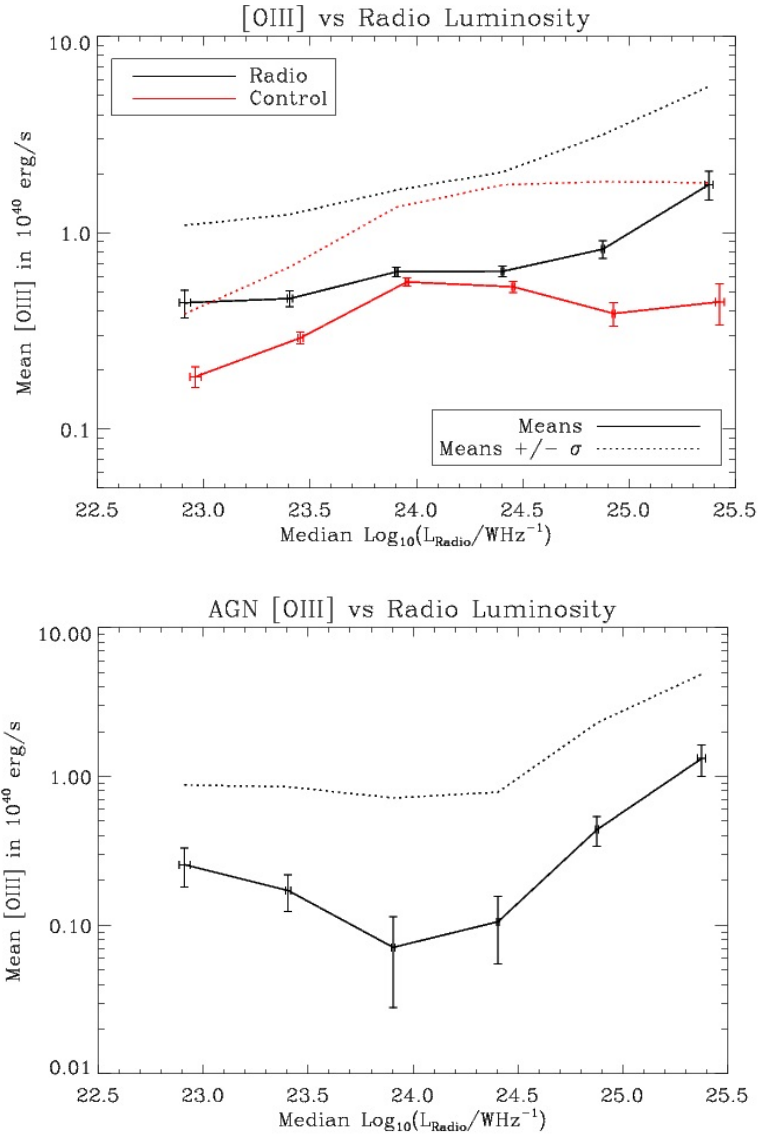


Figure 4.29: These images show the mean [OIII] plotted against the median radio luminosity for each radio bin under the czv matching scheme. Compare to Figures 4.28 and 4.30, which were created under the czm and czmv matching schemes, respectively.

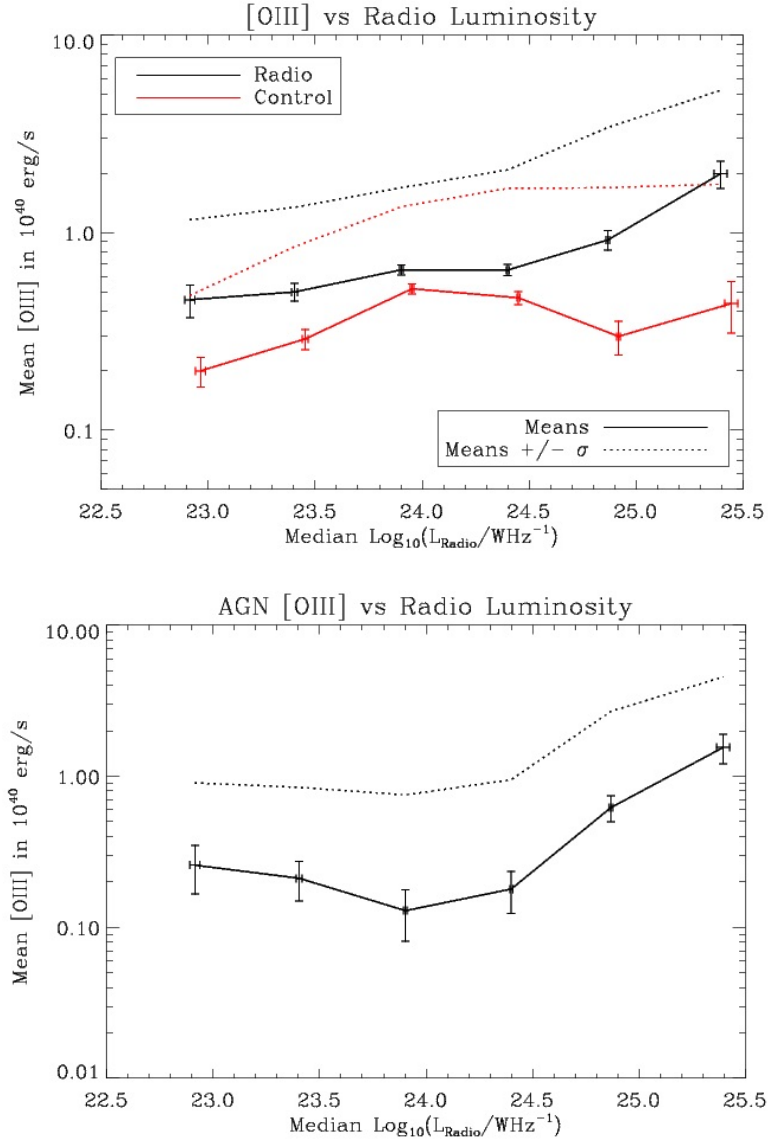


Figure 4.30: These images show the mean [OIII] plotted against the median radio luminosity for each radio bin under the czmv matching scheme. Compare to Figures 4.28 and 4.29, which were created under the czm and czv matching schemes, respectively.

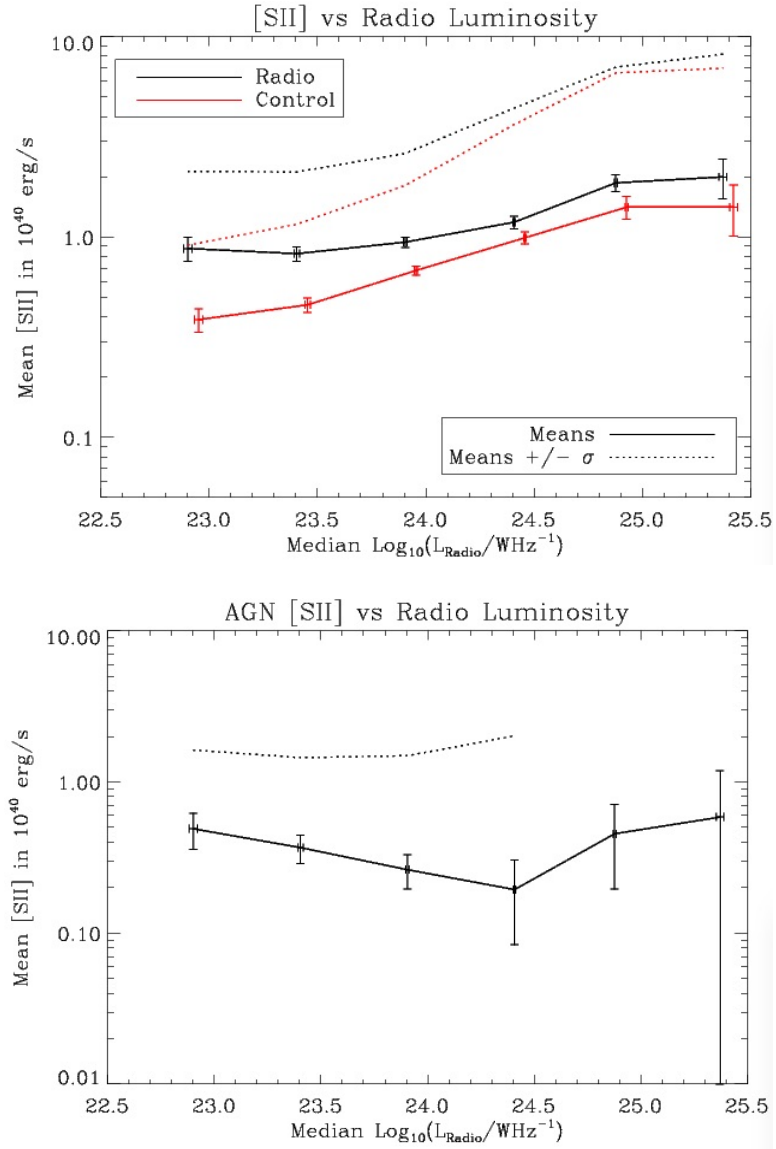


Figure 4.31: These images show the mean [SII] plotted against the median radio luminosity for each radio bin. See the caption for Figure 4.21 for further plot details.

Chapter 5 Results from Lognormal Modeling

5.1 Derivation of AGN Contribution from Fenton-Wilkinson Approximation

As illustrated by Figure 4.13, the emission line luminosity distributions for both the radio and the control samples resemble noisy log-normal distributions. Therefore, we assume their difference, which is the excess line emission associated with radio-AGNs also follows a lognormal distribution. For confirmation of this observation, compare the control sample histograms of Figure 4.13 (histograms of the $H\alpha$ distributions of Bin 2) and Figure 5.1 (a noise-added log-normal distribution based on the $H\alpha$ distribution of the Bin 2 control sample).

Under the premise that the AGN and stellar contributions can both be approximated as log-normal distributions,

$$X_r = X_{agn} + X_s = e^{Y_s} + e^{Y_{agn}} \quad (5.1)$$

where X_r , X_s , and X_{agn} represent the emission line luminosity distributions of the radio sample, the emission line distribution of the control sample (including non-AGN powered and radio-quiet AGN powered emission), and the distribution of excess line emission from radio-AGN, respectively. Moreover, under our log-normal assumptions, both Y_s and Y_{agn} are Gaussian distributions.

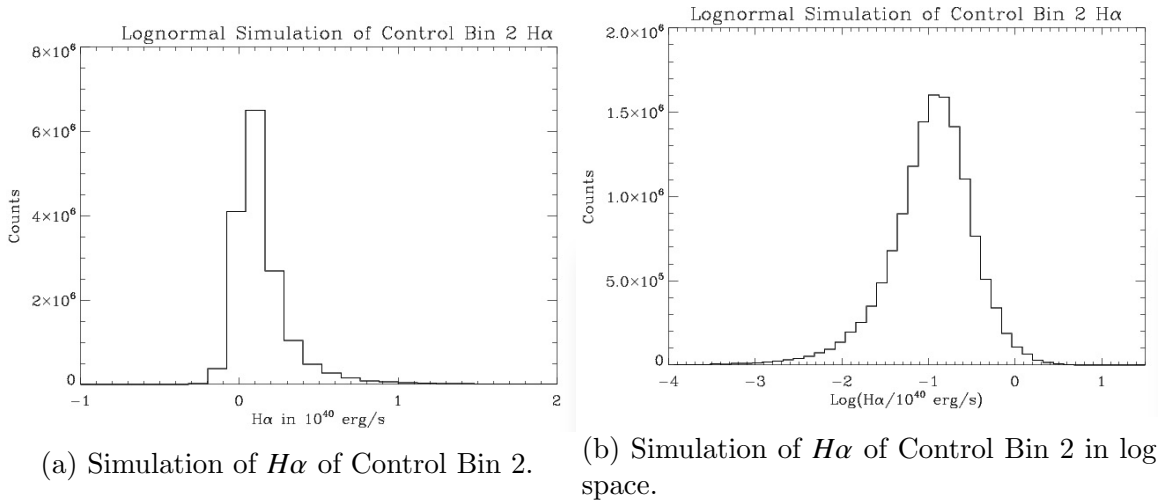


Figure 5.1: These histograms show the noise-added log-normal distributions meant to approximate the $H\alpha$ control distribution for Bin 2. The horizontal axis of the left plot shows $H\alpha$ in 10^{40} erg/s, while the horizontal axis of the right plot shows luminosity in terms of $\log(\frac{H\alpha}{10^{40} \text{ erg/s}})$. The vertical axes show the counts for the histograms. Notice that the counts for this noise-added log-normal distribution are much larger than those for the data histograms on which this is based.

From statistics, we know that X_r , a sum of log-normal distributions, generally has no closed form. Nonetheless, it can be reasonably approximated by a log-normal distribution, which is called the Fenton-Wilkinson Approximation and described by Fenton (1960) and Marlow (1967).

According to the Fenton-Wilkinson Approximation, this log-normal approximation of X_r has the following natural log space standard deviation (σ_r) and natural log space median/mean (μ_r):

$$\sigma_r^2 = \ln\left(\frac{e^{2\mu_s + \sigma_s^2}(e^{\sigma_s^2} - 1) + e^{2\mu_{agn} + \sigma_{agn}^2}(e^{\sigma_{agn}^2} - 1)}{(e^{\mu_s + \frac{\sigma_s^2}{2}} + e^{\mu_{agn} + \frac{\sigma_{agn}^2}{2}})^2} + 1\right) \quad (5.2)$$

$$\mu_r = \ln\left(e^{\mu_s + \frac{\sigma_s^2}{2}} + e^{\mu_{agn} + \frac{\sigma_{agn}^2}{2}}\right) - \frac{\sigma_r^2}{2} \quad (5.3)$$

We can substitute:

$$A = e^{\mu_s + \frac{\sigma_s^2}{2}} \quad (5.4)$$

$$B = e^{\frac{\sigma_s^2}{2}} \quad (5.5)$$

to get the equations:

$$e^{\sigma_r^2} - 1 = \frac{A^2(B^2 - 1) + e^{2\mu_{agn} + \sigma_{agn}^2}(e^{\sigma_{agn}^2} - 1)}{(A + e^{\mu_{agn} + \frac{\sigma_{agn}^2}{2}})^2} \quad (5.6)$$

$$\mu_r = \ln\left(A + e^{\mu_{agn} + \frac{\sigma_{agn}^2}{2}}\right) - \frac{\sigma_r^2}{2} \quad (5.7)$$

From the equation 5.7, that we can easily see that

$$e^{\mu_{agn} + \frac{\sigma_{agn}^2}{2}} = e^{\mu_r + \frac{\sigma_r^2}{2}} - A \quad (5.8)$$

Using this third substitution of equation 5.8 into equation 5.6, we find:

$$e^{\sigma_r^2} - 1 = \frac{A^2(B^2 - 1) + (e^{\mu_r + \frac{\sigma_r^2}{2}} - A)^2(e^{\sigma_{agn}^2} - 1)}{e^{2\mu_r + \sigma_r^2}} \quad (5.9)$$

Or:

$$(e^{\sigma_{agn}^2} - 1) = \frac{(e^{\sigma_r^2} - 1)e^{2\mu_r + \sigma_r^2} - A^2(B^2 - 1)}{(e^{\mu_r + \frac{\sigma_r^2}{2}} - A)^2} \quad (5.10)$$

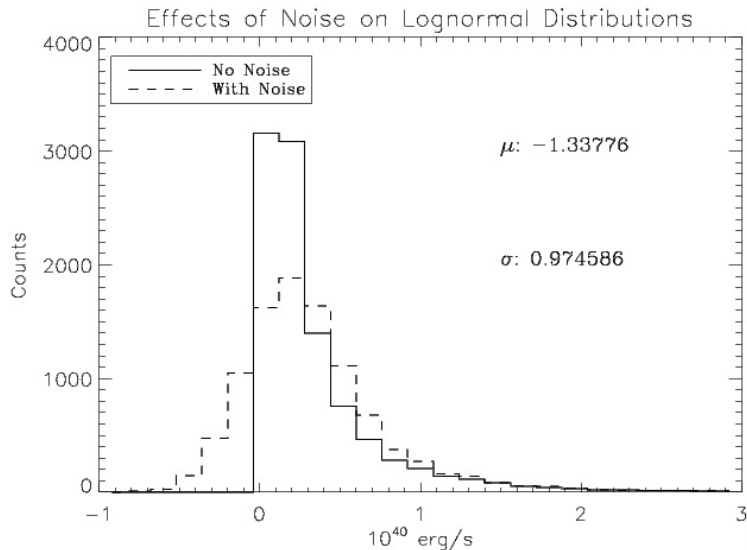


Figure 5.2: This histogram demonstrates the effects of random Gaussian noise on lognormal distributions. The lognormal distribution (shown by a solid line) was set to have a median of -1.6 and a standard deviation of 1.1 in natural log space. The dashed line shows what happened when Gaussian noise was added to this distribution. In natural log space, the median increased to roughly -1.3, and the standard deviation decreased to nearly 1.0.

Solving for our unknown σ_{agn}^2 :

$$\sigma_{agn}^2 = \ln\left(\frac{(e^{\sigma_r^2} - 1)e^{2\mu_r + \sigma_r^2} - A^2(B^2 - 1)}{(e^{\mu_r + \frac{\sigma_r^2}{2}} - A)^2} + 1\right) \quad (5.11)$$

Once we plug in values to obtain σ_{agn}^2 , we can go back to equation 5.8 and solve for μ_{agn} :

$$\mu_{agn} = \ln(e^{\mu_r + \frac{\sigma_r^2}{2}} - A) - \frac{\sigma_{agn}^2}{2} \quad (5.12)$$

5.2 Effects of Noise on Median and Standard Deviation

With this closed-form approximation of X_r , one might naively think that finding μ_{agn} and σ_{agn} would be a simple matter of taking the median and standard deviation of the control and radio emission line distributions in natural log space. The first problem becomes obvious very quickly. Noise shifts some luminosity measurements below zero, which is not physical. Nonetheless, as these distributions should be roughly lognormal, we can still estimate σ by subtracting the 50th percentile from the 84.135th percentile in natural log space.

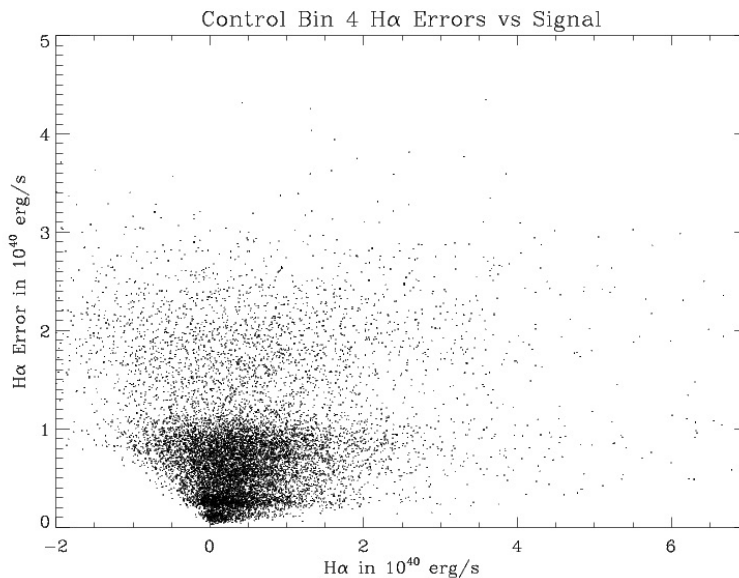


Figure 5.3: This scatter plot shows the reported error and signal for $H\alpha$ of Control Bin 4. The horizontal axis shows signal and the vertical axis shows the reported error. Both values are in 10^{40} erg/s. Notice how the negative signal values fan out, spreading to more negative values as reported measurement errors grow.

In addition to adjusting our methods of taking the standard deviation, we must also take into account the effects of noise on log-normal medians and standard deviations. Figure 5.2 demonstrates an example of such effects. In this plot, the solid line represents the noise-free distribution, which is a random lognormal distribution with a σ set to 1.1 and a median set to -1.6 in natural log space (not atypical values for the data). The dashed line shows what happens when we add Gaussian noise of randomly-assigned error values between .2 and .3 (reasonably close to data error values). Notice that the log space σ decreased by about 9%, whereas the log space median was shifted higher by roughly 18%. Thus, any methods of lognormal modeling must account for noise-induced shifts in median and standard deviation.

5.3 Testing Error Measurements

When modeling noise-added distributions, it is essential to have accurate noise measurements. So, when the lognormal simulations weren't fitting the data well, we decided to check our noise measurements. Independent of the particulars of the emission line luminosity distributions, the galactic luminosities physically must be non-negative. Thus, any negative luminosity measurements must result from noise scattering. So, in general terms and without outliers, one would expect any statistically-significant rms of negative luminosity measurements to be equal to or less than the mean (and median) recorded error of the same galaxies.

To evaluate our samples in this manner, we wanted to compare only statistically-significant rms values to the mean/median error values. Looking at the error versus

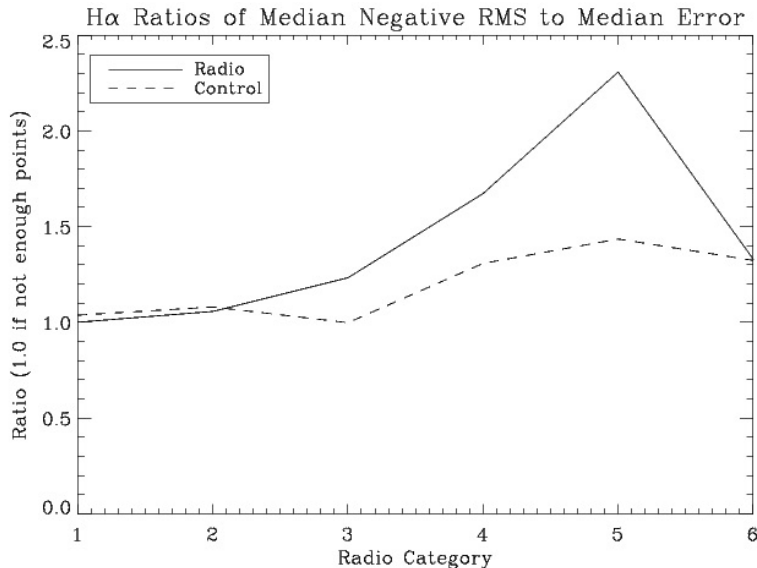


Figure 5.4: This plot shows the rms of negative $H\alpha$ values divided by the median reported errors as a function of radio bin. The vertical axis gives the value of the rms divided by the median reported error. The horizontal axis shows the radio bin number in order of increasing radio luminosity. The radio bins are connected by a solid line, while the control bins are connected by a dashed line. A ratio of 1 was assigned to any bin in which there were not enough negative values for our analyses.

signal plots for the data, such as in Figure 5.3, one can see that the distribution of negative luminosities fans out with increasing measured error, as one would expect. So, to limit our study to significantly negative luminosity rms values, we studied only the galaxies with negative luminosity values and measured errors between the 70th and 90th error percentiles. Moreover, to minimize uncertainty from small number statistics, we only considered the samples with ten or more galaxies fitting these constraints.

As depicted for $H\alpha$ in 5.4, several radio and control samples showed negative rms luminosity values which were larger than the median reported errors for the same galaxies. (Although not depicted here, the same could be said of the mean reported errors.) For example, look at Control Bin 5. The negative rms luminosity value was approximately 1.3 times the median reported error. These values notify us that the reported errors for these luminosities were likely underestimated. Notice that, since the true emission line luminosities can be positive, the noise may be scattering the luminosity measurements from positive values instead of from zero. Thus, the instances wherein the negative luminosity rms values are less than or equal to the mean/median error values don't necessarily have properly-estimated errors. Instead, from the rms analysis, we could only conclude that underestimated error values most likely exist in some samples (but may be present in any of the samples).

This prompted us to reanalyze the reported emission line errors. Initially, the flux error was simply taken to be the formal measurement error resulting from the inverse of the variance for the spectrum and the continuum. To represent the actual uncer-

tainty, these error measurements were scaled up according to the spreads of repeated observations, which resulted in more logically consistent error-to-signal estimates.

5.4 Lognormal Modeling through Random Walks

The modeling algorithm used a random walk to find the optimal fit to the data for each radio sample and its corresponding control sample. During the random walks, we use the Kolmogorov–Smirnov distance metric as a goodness of fit indicator. For each emission line of every sample, the walk began at the original estimate of μ and σ . These values of μ and σ were used to build a random lognormal distribution to represent the emission line luminosity distribution of the data. As mentioned before, we wanted the random walks to account for the effects of noise. So, using the noise found in the luminosity data, we added randomized Gaussian noise to the representative log-normal distribution (the process of which will be described below in detail). Finally, the KS metric was found for the noise-added log-normal distribution in relation to the data.

After finding the KS metric for the initial simulated distribution, the modeling algorithm took a random-walk step—the size and sign of which were set with a Gaussian random number generator of standard deviation 0.3—in both the μ and σ dimensions. A lower limit of insignificant positive value was chosen for σ so as to prevent negative σ values. Given the new values of μ and σ , the algorithm created a new noise-added random log-normal distribution and found the corresponding KS metric in relation to the data. If the new KS metric was smaller (thus representing a better fit), the new μ and σ values replaced the old the old values in the simulated distribution. If the new KS metric was larger than the old, the new σ and μ values were accepted at a rate of $e^{400(k_{old}-k_{new})}$ where k represents the KS metrics. The selection of 400 as the coefficient was based on individual judgment regarding experimental random walks. The motive behind allowing acceptances of distributions with slightly larger KS metrics is to allow the random walk to escape possible local minima in the attempt to find the absolute minimum of the KS metrics. The random walk was done for 2000 steps. If the coefficient was too small, the dependence in differences in KS metrics would be diminished, thus allowing random walks to “wander” over a large region without sufficient confinement to areas of low KS metrics. Contrastingly, if the coefficient was too large, the role of the differences in KS metrics could become too pronounced—thus disallowing much movement during the random walks and potentially trapping the random walks in local minima without finding the absolute minimum KS metric. So, with trial and error, we set the random walk coefficient to 400 to balance meaningful confinement with sufficient freedom of movement. One example of such random walks is shown in Figure 5.5.

During the analysis of the random walk, the first 250 steps were disregarded to account for the time the random walk needed to reach a low KS metric region away from the starting points. Then, the medians of the unique values of μ and σ were taken as the fit values for that particular data sample.

For fitting purposes, it is essential to simulate the data noise well. To build the noise distribution for the simulations, it is important to consider possible redshift-

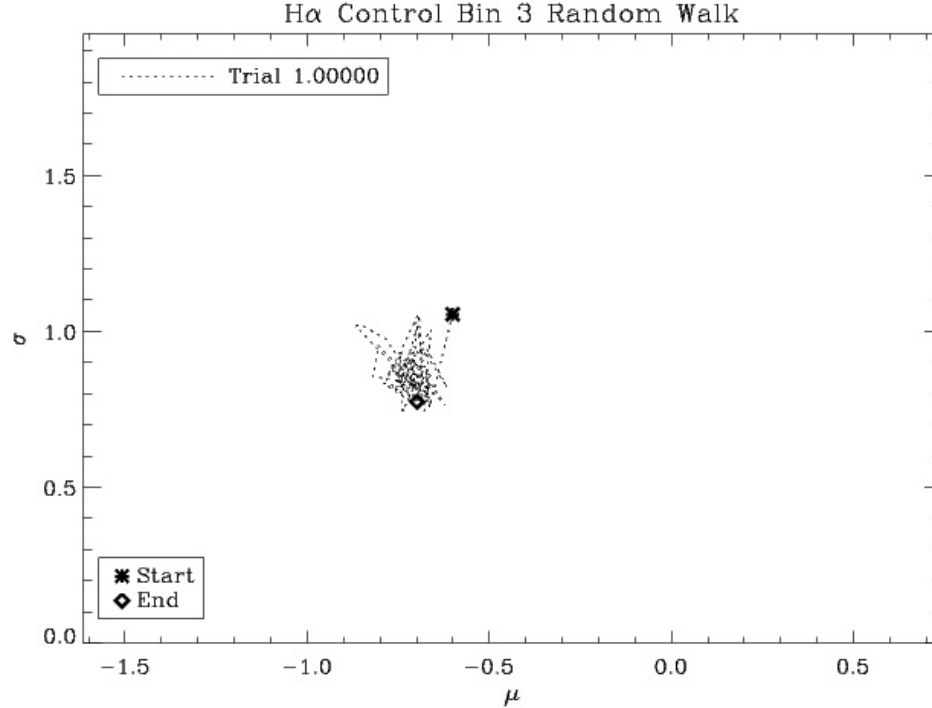
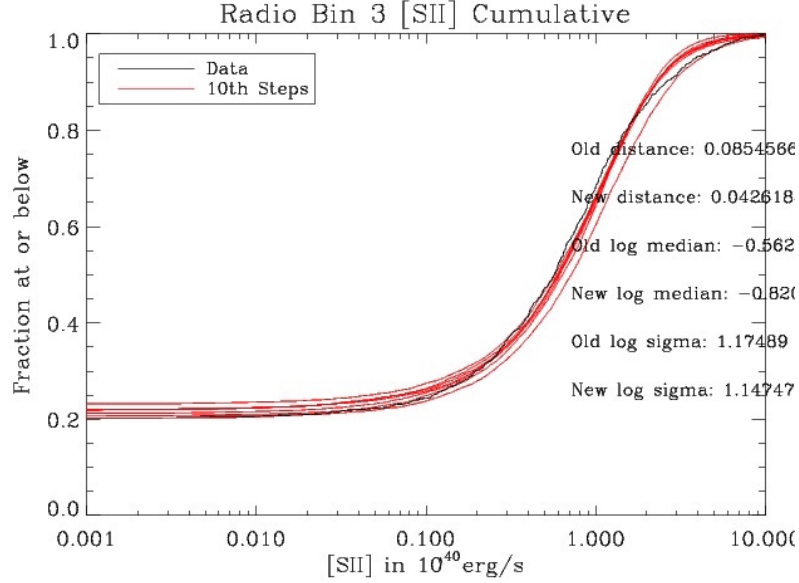


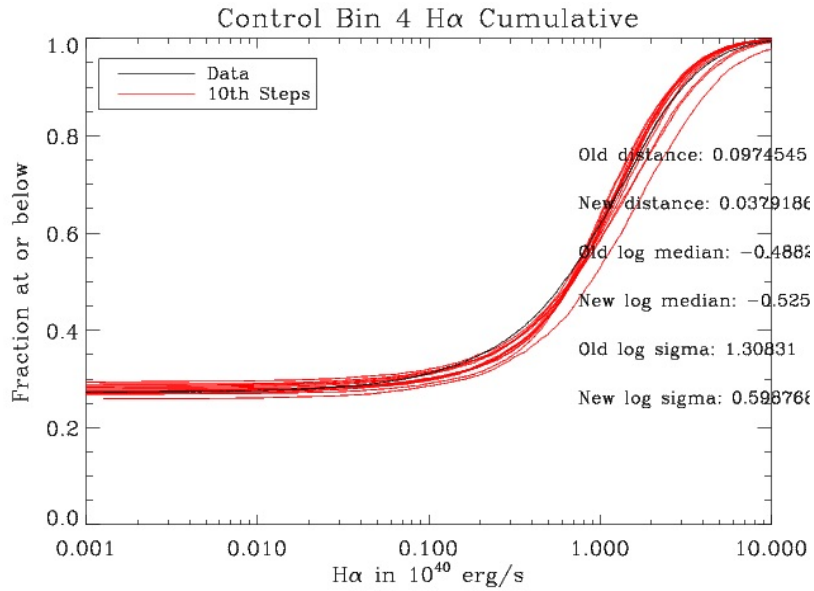
Figure 5.5: This plot shows an example of a random walk as described in the text. The horizontal axis shows μ values, while the vertical axis indicate values of σ . The asterick symbol depicts the beginning of the random walk segment after the "settling" period, whereas the diamond indicates the end of the random walk. The dashed line shows the path taken as the algorithm searches for the optimal log-normal fit to the data (which happens to be the $H\alpha$ control distribution for Bin 3).

noise correlations. So, first, redshifts from the data sample were randomly assigned to the simulated galaxies. Then, the measured errors of the sample galaxies were assigned to the simulated galaxies according to the previous redshift assignment. Finally, the error assignments were multiplied by a random Gaussian distribution to create a Gaussian noise distribution. This noise distribution was added to the log-normal simulations during the random walk.

A couple of fits are shown in Figure 5.6. Notice that the lines are fairly well fitted. Because the Fenton-Wilkinson approximation best depicts the right side of the sum of log-normal distributions (Fenton, 1960), it is more important for the simulations to fit the right side of the radio sample distributions than to necessarily fit the entire radio sample distribution. The resulting fittings were used in conjunction with the Fenton-Wilkinson approximation to estimate the AGN-powered emission line approximations are shown in. Admittedly, all lines are missing one or more values for the AGN-powered distributions. This has two likely explanations: the means of the radio and control bins were too close in value and/or the unusual dependence on σ , which is a result the Fenton-Wilkinson approximation. When $e^{\mu + \frac{\sigma^2}{2}}$ is larger for the control than for the radio samples, this approximation gives non-real values of μ_{agn} .



(a) Fit for [S] in Radio Bin 3.



(b) Fit for $H\alpha$ in Control Bin 4.

Figure 5.6: These plots show lognormal fittings for [S] in Radio Bin 3 and $H\alpha$ in Control Bin 4. The horizontal axes give the emission line luminosities in 10^{40} erg/s, and the vertical axes give the fraction of the sample or distribution at or below a given emission line luminosity. The data is shown by a black line, and every 10th step of the random walk is depicted by a red line. The KS-metric comparing the simulations to the data is labeled as "Distance" with "Old" referring to an early attempt wherein we did not add noise to our lognormal distributions during simulations and "New" referring to our current methods. Notice that our current methods give much better fits (as measured by smaller KS-metrics), illustrating the importance of taking noise into account when using this method.

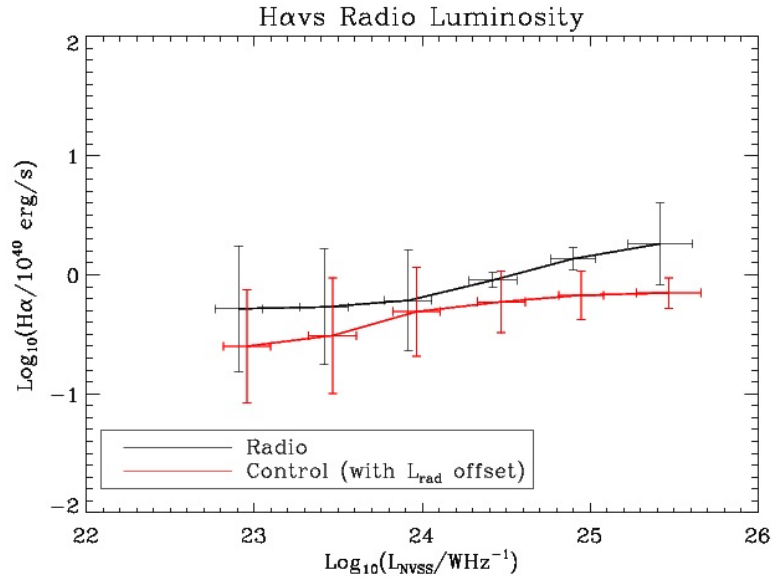
Thus, a rather large σ in a control sample can easily result in being unable to obtain a meaningful AGN-powered distribution estimate for that particular bin. Nonetheless, looking at the AGN-powered $H\alpha$, [OII], [OIII], and [SII] trends for which we found valid AGN-powered luminosity values, the means follow the "dipping" trend when plotted against radio luminosity in log space.

5.5 Revisiting the Differences in Medians

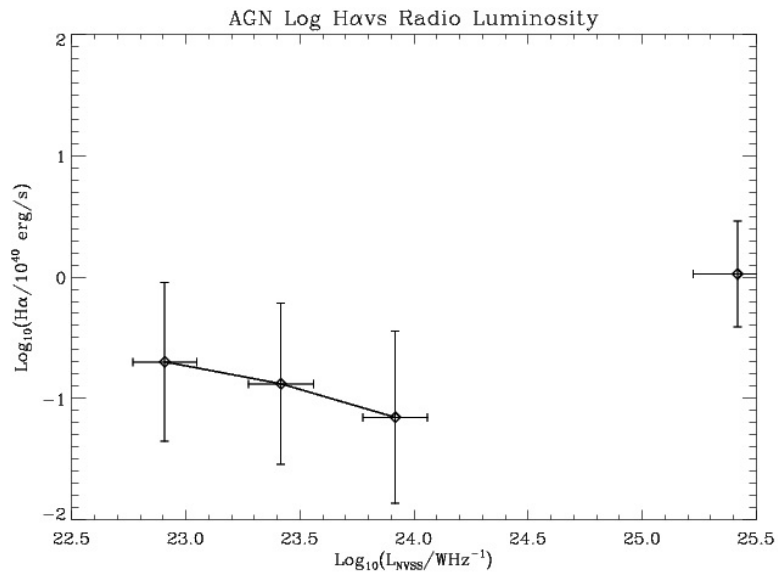
In light of noise effects on log-normal μ values, we revisited the differences between radio sample and control medians using the fitted median values instead of the data median values. As you can see from Figures 5.14 through 5.20, there are a few differences between these plots and Figures 4.14 through 4.20, but the results for several lines qualitatively remain the same with "dipping" patterns. With the notable examples of $H\beta$ and [NII], the "dipping" pattern in differences of medians mainly changes in the error estimations—becoming more defined at the low radio luminosity and and less defined for a few of the higher bins. The simulated $H\beta$ dipping pattern is notably more shallow at the low radio luminosity end than is the pattern resulting directly from $H\beta$ data. On first glance, the simulated [OI] dipping pattern likewise seems more shallow on the left than is the data-derived [OI] pattern, but forming definite conclusions about this particular change in plots is difficult due to the size of the vertical error bars on the left side of the data-generated differences in [OI] medians.

5.6 Discussion

A natural question that arises is whether the upturn in emission line luminosities at the lower radio luminosities may be due to star formation contamination. After all, if one considers Table 5.1, Best & Heckman (2012) classified nearly five percent of the radio galaxies in the first radio bin as "star forming." However, we believe that including these galaxies in our analysis affects the results negligibly. To prove this is the case, we present three arguments. Firstly, our control samples were matched to their respective radio samples in color, meaning the control samples should have stellar ages and star formation rates that are comparable to the radio samples, thus negating any significant effect of star formation when the stellar component is removed from the composite emission line luminosities. Secondly, as shown in Table 5.1, Best & Heckman (2012) classified no more than 4.8% of any radio bin as "star forming," and our methods rely on median luminosity values, which are less affected by potential contamination than are mean values. Thus, after the subtraction of the control medians, the small amount of potential remaining star formation contamination should have a negligible effect on our result. Thirdly, borrowing one classification scheme mentioned by Best & Heckman (2012), we created scatter plots of galaxies' $H\alpha$ luminosities against radio luminosities. To preserve accuracy, we only plotted galaxies with a $H\alpha$ signal-to-noise ratio above two. While some galaxies appear above the suggested AGN-star formation separation line (as derived by Best & Heckman (2012)),

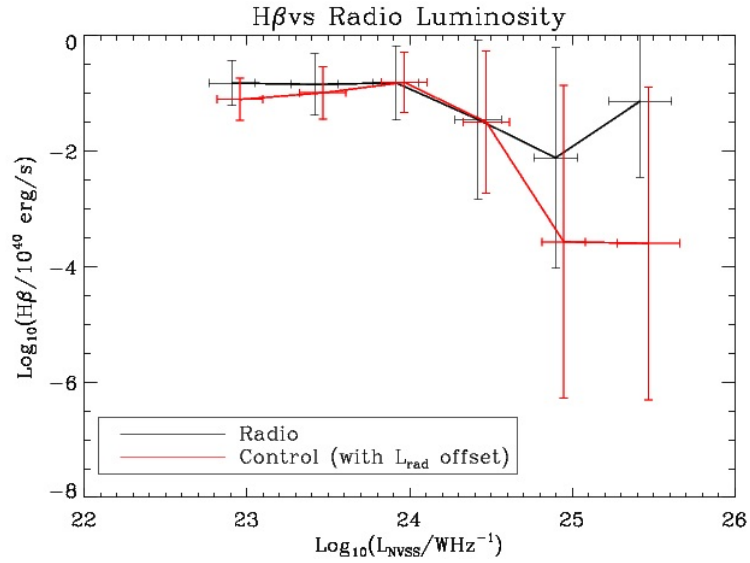


(a) Simulated Radio and Control Sample $H\alpha$

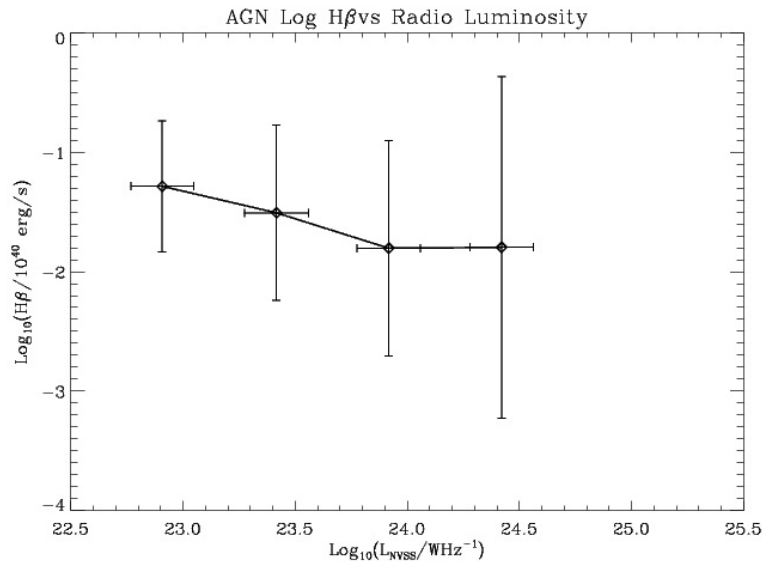


(b) Simulated AGN-powered $H\alpha$

Figure 5.7: These plots show the results of our lognormal modeling for $H\alpha$. The vertical axes show the log of the emission line luminosity in erg/s. The horizontal axes show the log of the median radio luminosity in W/Hz. For these plots, the data points are the distribution log-space means, and the error bars depict the log-space standard deviations. The top plot shows the simulated $H\alpha$ distributions for the radio (in black) and control samples (in red). The bottom plot shows the extracted AGN-powered $H\alpha$ distribution for each radio bin (when meaningful results were obtained).

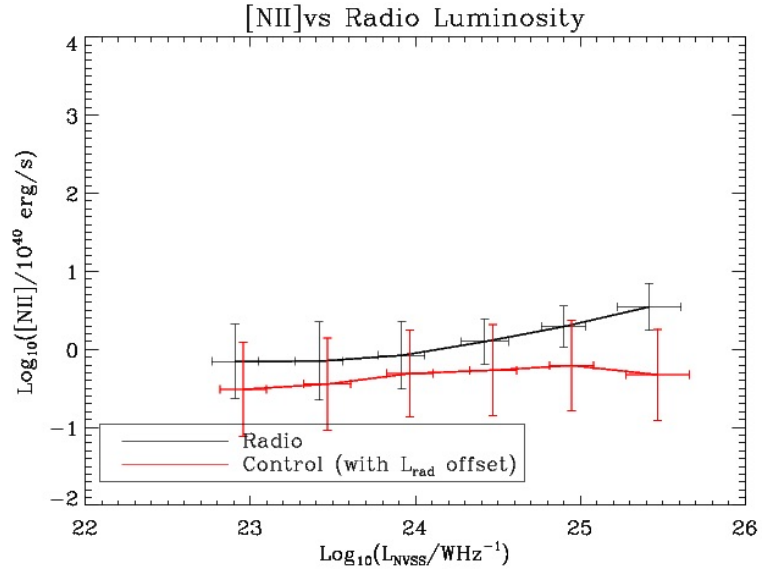


(a) Simulated Radio and Control Sample $H\beta$

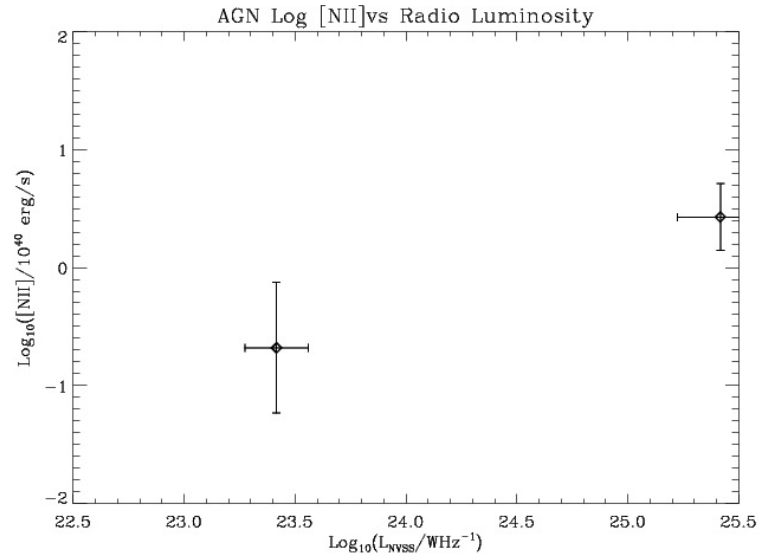


(b) Simulated AGN-powered $H\beta$

Figure 5.8: These plots show the results of our lognormal modeling for $H\beta$. Note that the error bars depict standard deviation. See the caption for Figure 5.7 for details.

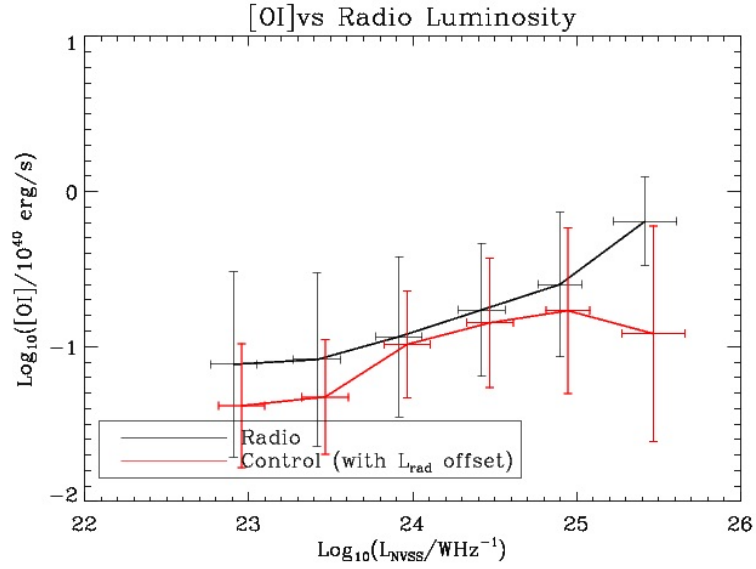


(a) Simulated Radio and Control Sample [NII]

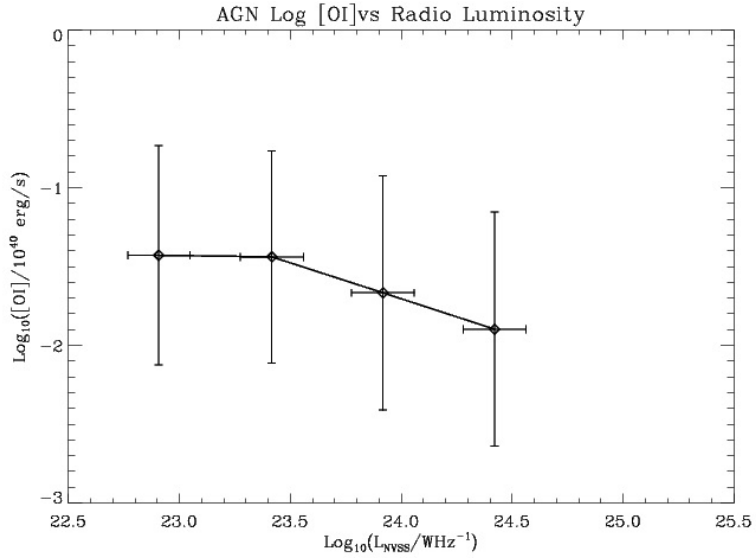


(b) Simulated AGN-powered [NII]

Figure 5.9: These plots show the results of our lognormal modeling for [NII]. Note that the error bars depict standard deviation. See the caption for Figure 5.7 for details.

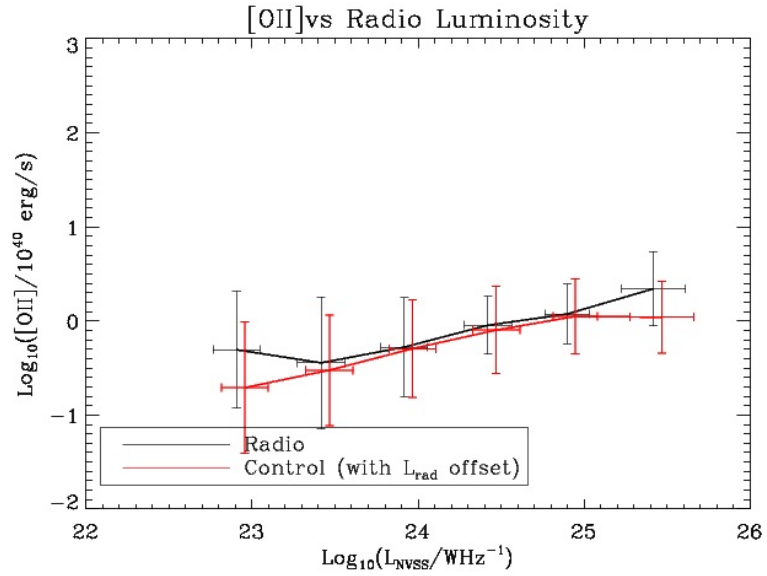


(a) Simulated Radio and Control Sample [OI]

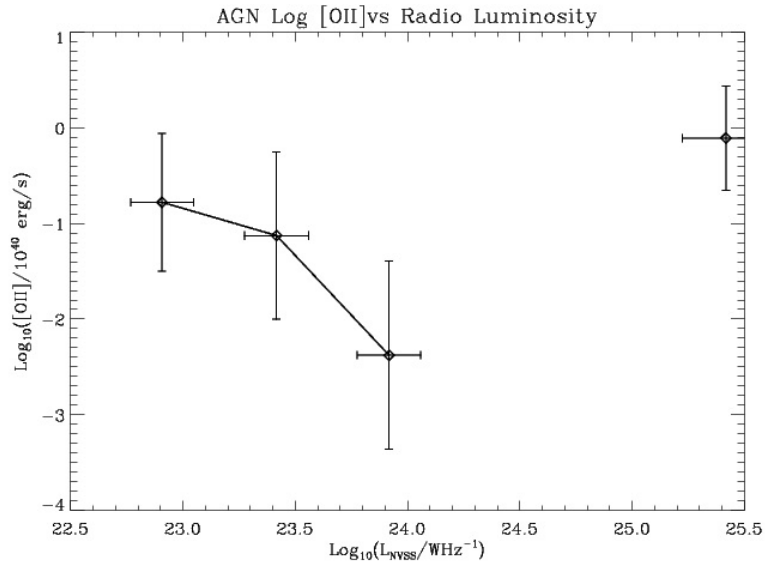


(b) Simulated AGN-powered [OI]

Figure 5.10: These plots show the results of our lognormal modeling for [OI]. Note that the error bars depict standard deviation. See the caption for Figure 5.7 for details.

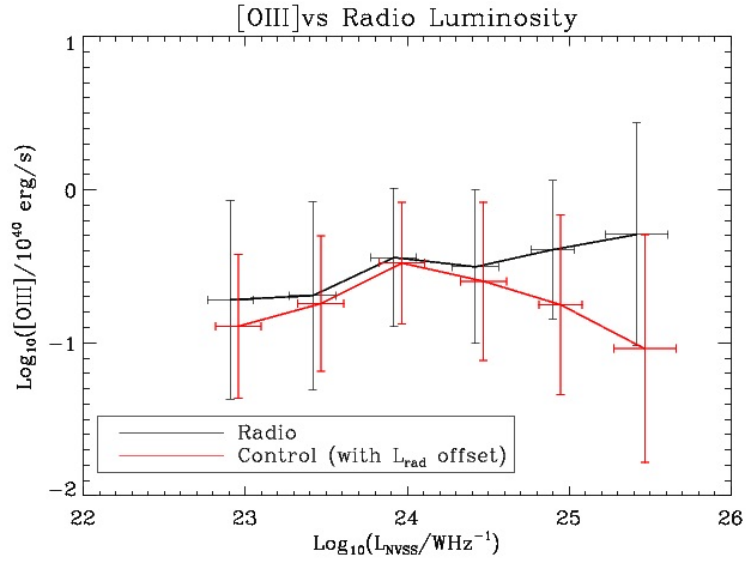


(a) Simulated Radio and Control Sample [OII]

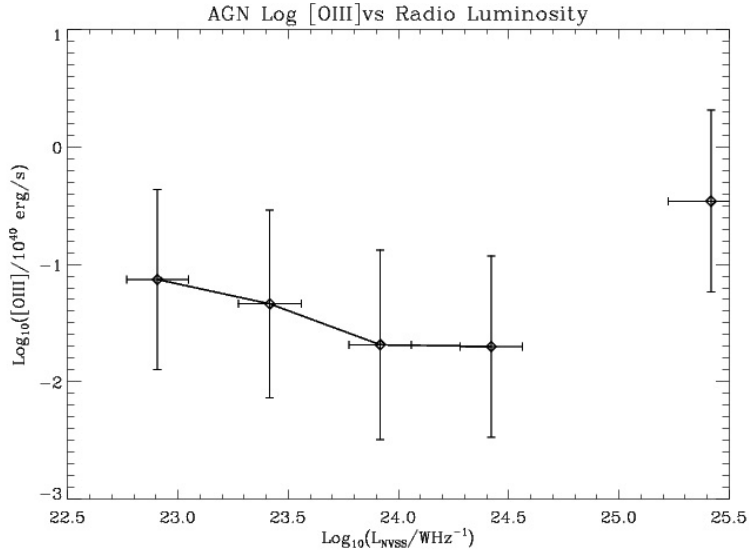


(b) Simulated AGN-powered [OII]

Figure 5.11: These plots show the results of our lognormal modeling for [OII]. Note that the error bars depict standard deviation. See the caption for Figure 5.7 for details.

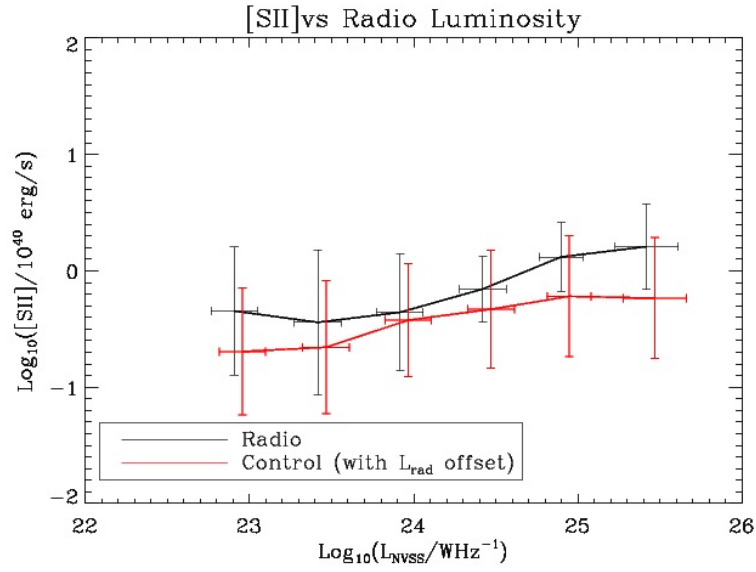


(a) Simulated Radio and Control Sample [O3II]

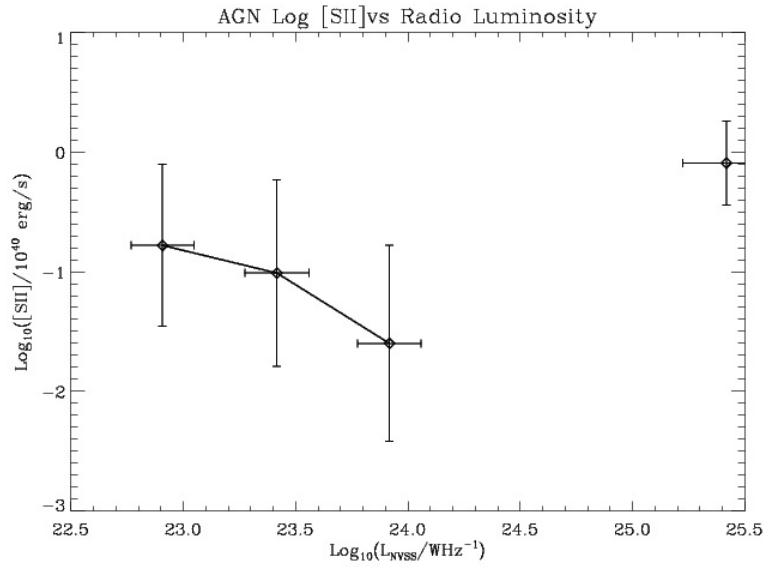


(b) Simulated AGN-powered [OIII]

Figure 5.12: These plots show the results of our lognormal modeling for [OIII]. Note that the error bars depict standard deviation. See the caption for Figure 5.7 for details.



(a) Simulated Radio and Control Sample [SII]



(b) Simulated AGN-powered [SII]

Figure 5.13: These plots show the results of our lognormal modeling for [SII]. Note that the error bars depict standard deviation. See the caption for Figure 5.7 for details.

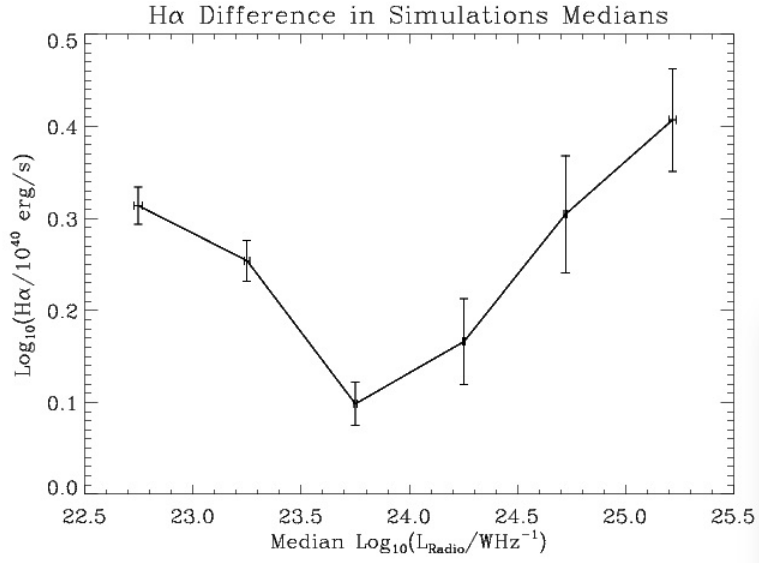


Figure 5.14: This plot shows the differences in $H\alpha$ medians between the log-normal models representing the radio samples and their corresponding control samples. The horizontal axes shows logarithm of the median radio luminosities (in W/Hz) of the radio samples. The vertical axes show the differences of emission line luminosity medians in 10^{40} erg/s . The error bars depict the errors in measuring medians.

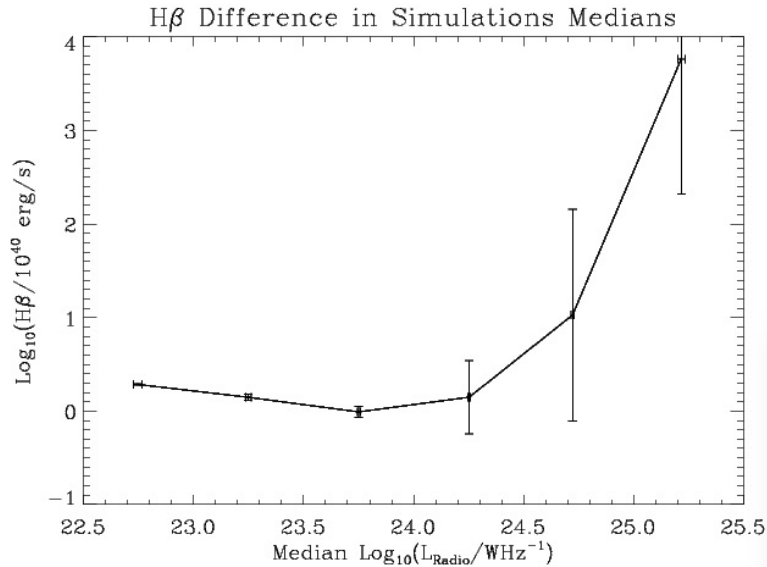


Figure 5.15: This plot shows the differences in $H\beta$ medians between the log-normal models representing the radio samples and their corresponding control samples. See the caption for Figure 5.14 for plot details.

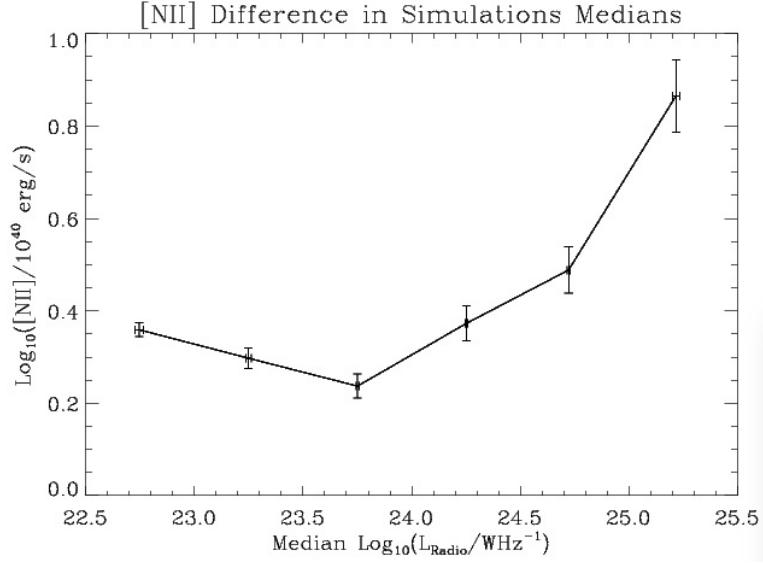


Figure 5.16: This plot shows the differences in [NII] medians between the log-normal models representing the radio samples and their corresponding control samples. See the caption for Figure 5.14 for plot details.

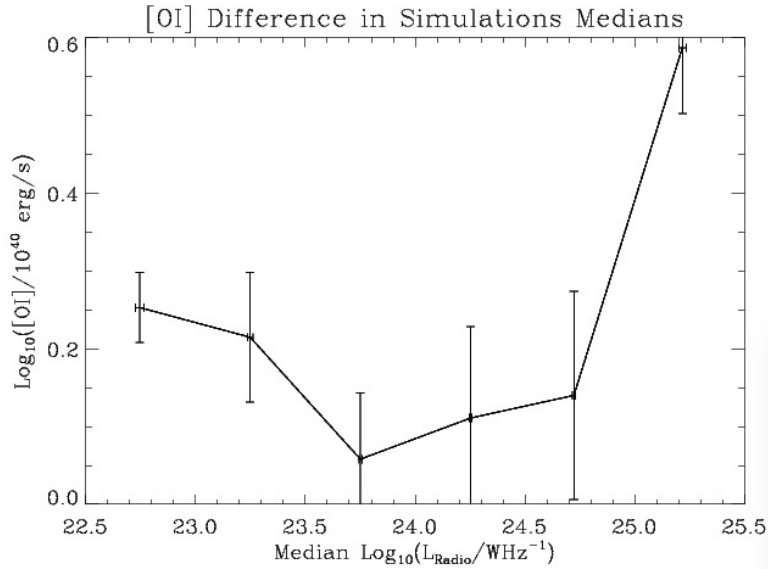


Figure 5.17: This plot shows the differences in [OI] medians between the log-normal models representing the radio samples and their corresponding control samples. See the caption for Figure 5.14 for plot details.

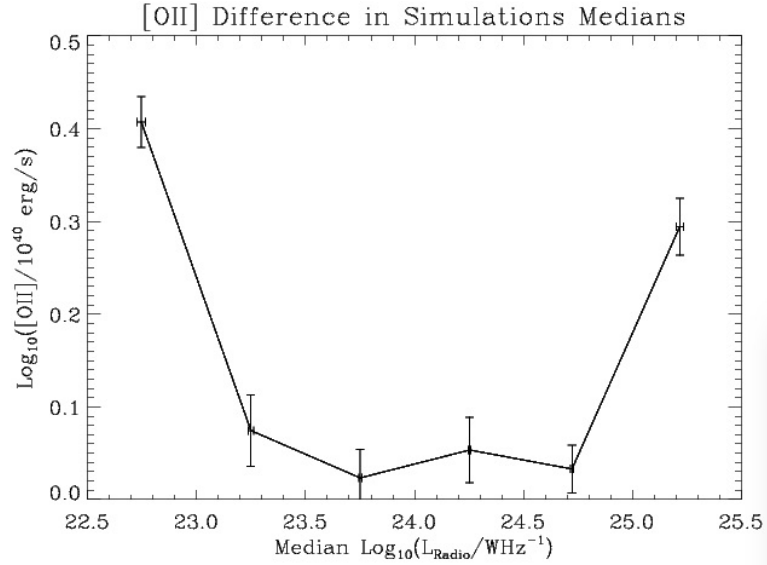


Figure 5.18: This plot shows the differences in [OII] medians between the log-normal models representing the radio samples and their corresponding control samples. See the caption for Figure 5.14 for plot details.

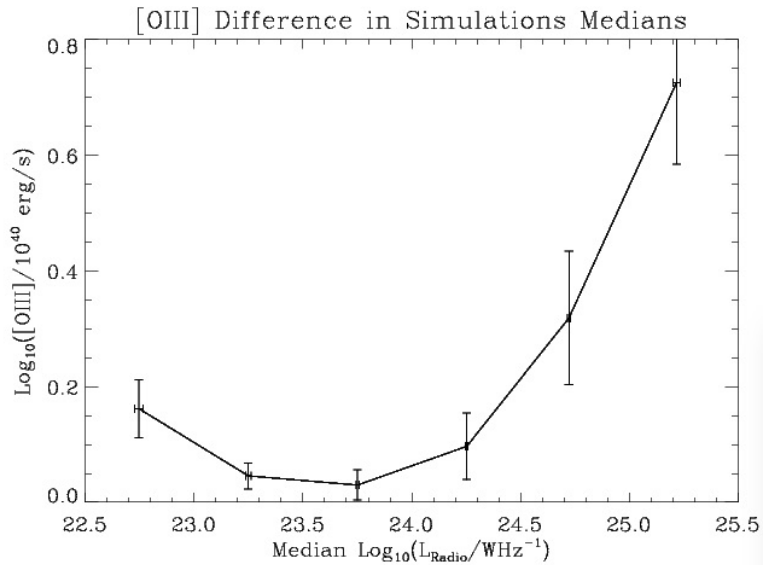


Figure 5.19: This plot shows the differences in [OIII] medians between the log-normal models representing the radio samples and their corresponding control samples. See the caption for Figure 5.14 for plot details.

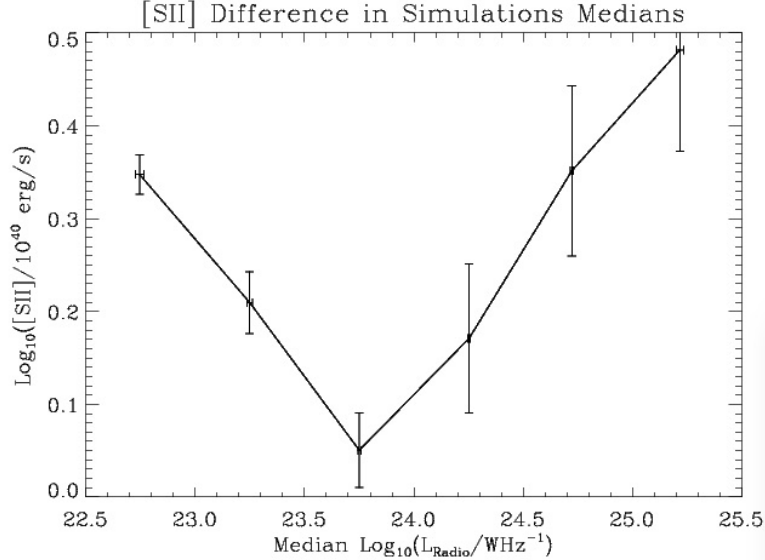


Figure 5.20: This plot shows the differences in [SII] medians between the log-normal models representing the radio samples and their corresponding control samples. See the caption for Figure 5.14 for plot details.

even the Best & Heckman (2012) scatter plot shows that this suggested line does not cleanly separate all AGN-classified galaxies from the star-forming galaxies. Moreover, all galaxies shown in our $H\alpha$ -radio luminosity scatter plots fall within the range of the AGN galaxies as classified by Best & Heckman (2012), and our samples show no significant bimodality in the scatter plots, as one would expect if there was significant star formation contamination. To confirm our assertions, the few galaxies designated as "star forming" by Best & Heckman (2012) were removed from the samples and the differences in control and radio emission luminosity medians were replotted. The results changed, at most, slightly from the previous differences of medians.

Another issue to consider is morphology. In general, FR-II galaxies tend to dominate at higher radio luminosities, most noticeably at $10^{26} W/Hz$ for 1.4 GHz (Owen & Laing, 1989). In general, FR-II galaxies tend to have more powerful AGN and/or less dense environments than do FR-I galaxies, allowing the jet material to be flung out further away at higher velocities (Meisenheimer et al., 1989; Laing & Bridle, 2002). Hence, it would be tempting to try to explain the trend in emission line luminosities as a transition between FR-I and FR-II prevalence in the samples. Nonetheless, as noted by Lin et al. (2010), there isn't a very clean separation between the properties of FR-I and FR-II galaxies. Thus, we believe that a less ambiguous correlation can be determined by looking at efficiency rates via studying emission line luminosity-to-Eddington or radio luminosity-to-Eddington ratios.

As depicted in Figure 5.21, there is a strong correlation between radio luminosity and the ratio of radio luminosity to $vdisp^4$. Using the well-known velocity dispersion-to-black hole mass relation discussed in the introduction, we used the fourth power of the velocity dispersion as a stand-in for SMBH mass. SMBH mass is likewise directly proportional to the SMBH's Eddington Limit (the maximum radiative output

Table 5.1: Classifications of Radio Galaxies

Radio Sample	# of Galaxies	% LERG	% HERG	% Unidentified AGN	% Star-forming
1	104	95.2	0.0	0.0	4.8
2	350	98.3	0.0	1.4	0.3
3	924	87.1	0.3	12.4	0.1
4	1435	81.5	0.3	18.2	0.0
5	814	83.8	0.9	15.4	0.0
6	190	87.4	2.6	10.0	0.0

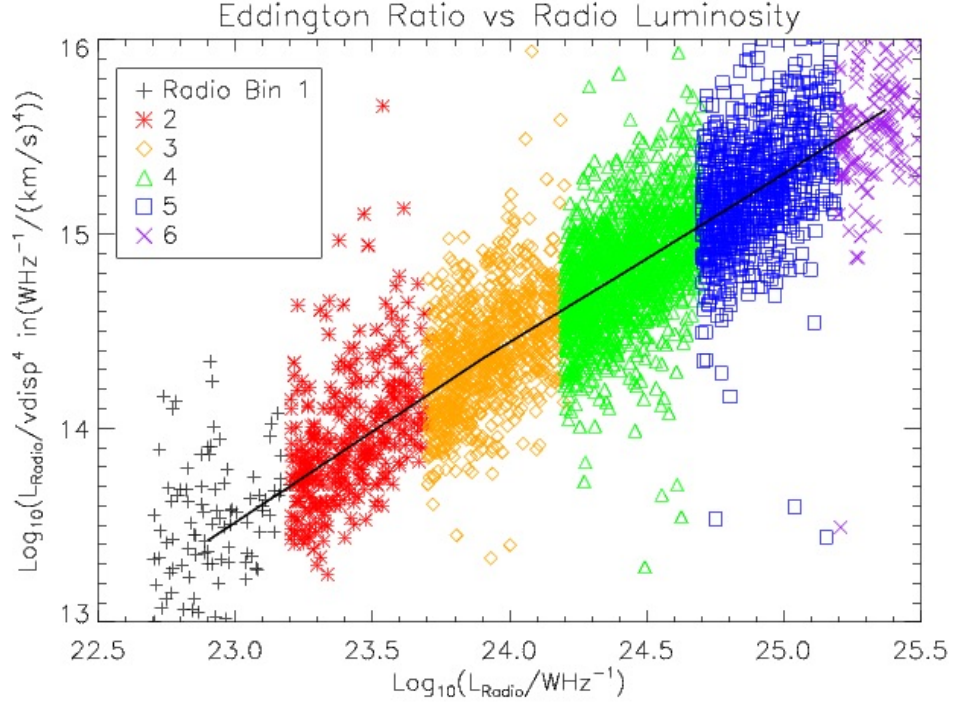


Figure 5.21: This plot compares the relationship of radio luminosities and radio-to-Eddington luminosity ratios. The horizontal axis shows the log of radio luminosity in W/Hz. The vertical axis gives the log of the radio luminosity divided by the fourth power of the velocity dispersion. The individual galaxies' values are shown as symbols, the color and shape of which indicate their radio bins. The solid black line connects the median radio luminosity-to-median $vdisp^4$ ratios of each bin.

which is allowed by hydrostatic equilibrium (Eddington, 1925)). Thus, setting the constant values in these relations to unity, we compared the radio luminosity output (an indicator of kinetic energy release) to the Eddington limit for the SMBHs. The resulting correlation seems to suggest that, within our radio samples, the AGN become more kinetically-efficient with increasing radio luminosity.

After looking at comparisons of radio luminosities to Eddington limits, we followed up by exploring the implications for emission lines. In Figures 5.22 to 5.27, we examined relationship between the AGN-powered emission line-to-Eddington limit ratios with the radio luminosity-to-Eddington limit ratios. To represent the emission line-to-Eddington ratios, we used the estimated the mean AGN-powered emission lines divided by the fourth power of the median $vdisp$ for each bin. Similarly, we used the median radio luminosity divided by the fourth power of the median $vdisp$ to represent the radio-to-Eddington ratios. In Figures 5.22 to 5.27, the emission line-to-Eddington ratios are on the vertical axes, and the radio-to-Eddington ratios are on the horizontal axes. The error bars represent to estimated errors in these estimations, propagated from the errors in emission line means and radio luminosity medians. Note that, while the horizontal error bars are unnoticeably small, the vertical error bars are significant. The vertical error bars were too large to discern meaningful results

for $H\beta$. A few other emission lines from specific bins (such as [SII] for the sixth bin) show large error bars. Even so, most of the lines seem to show a transition around Radio Bins 3 and 4. [OII] seems to show an extreme transition between Bins 4 and 6, but we must view Figure 5.25 with extra caution as the radio and control samples were too similar to give a useful AGN-powered mean for Bin 5. In general, Bins 1 through 3 (or 1 through 4) tend to have decreasing emission line luminosities, as well as decreasing emission line-to-Eddington limit ratios. In sharp contrast, the bins with higher radio luminosities generally showed increases in both emission line luminosities and emission line-to-Eddington limit ratios.

Comparisons of this to Figure 5.21 would suggest that, at radio luminosities below the regions of $10^{23.7}$ to $10^{24.7}$ W/Hz, the relation of the emission lines to the Eddington limit is anti-correlated to that of the radio luminosities. However, above this region, the two relations seem positively-correlated.

From this observation, one might propose that the mechanism for increasing radio efficiency (kinetic energy release) is likewise tied to the emission lines at higher radio luminosities. By a similar line of reasoning, one might suppose that, at lower radio luminosities, the dominant mechanism of emission line production is opposed to that of increasing radio efficiency (at least in terms of population statistics). Thus, perhaps AGN-powered emission lines dominantly result from photoionization in AGN with low radio efficiency, and result from collisional ionization when a higher fraction of the energy is released kinetically. If so, one might further speculate that we're viewing two populations of AGN with distinct accretion modes. At the lower radio luminosities, decreasing radiative efficiency with increasing radio luminosity is consistent with the RIAF model (Netzer, 2013). Above the dip shown by the data, the positive correlation between emission line and radio luminosities could be explained by radio bubbles shock heating their surroundings. This idea merits further investigation.

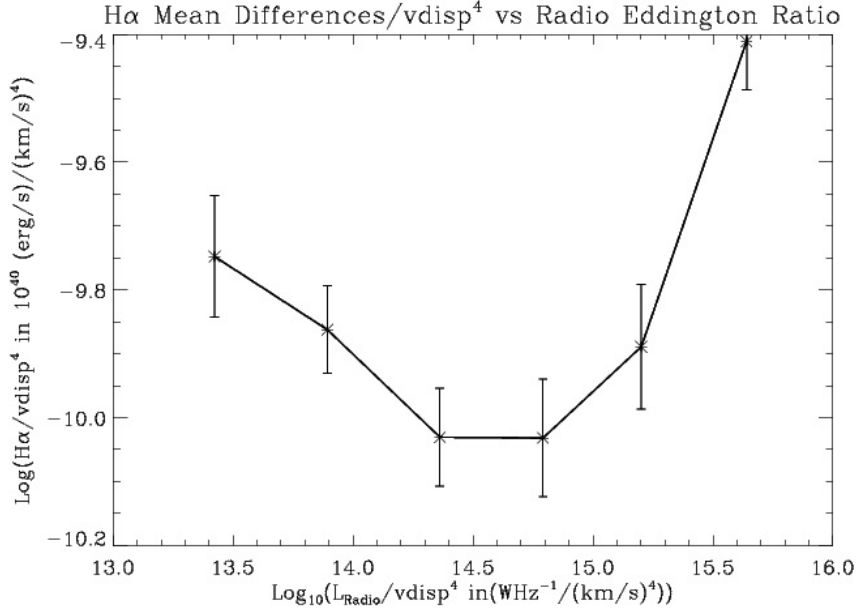


Figure 5.22: This plot compares the relationship of $H\alpha$ -to-Eddington luminosity ratios and radio-to-Eddington ratios. The vertical axis shows the base-10 log of the median radio luminosity divided by the fourth power of the radio sample’s median velocity dispersion. The vertical axis gives the base-10 log of the AGN-powered mean $H\alpha$ (representing the mean AGN-powered $H\alpha$) divided by the fourth power of the median velocity dispersion.

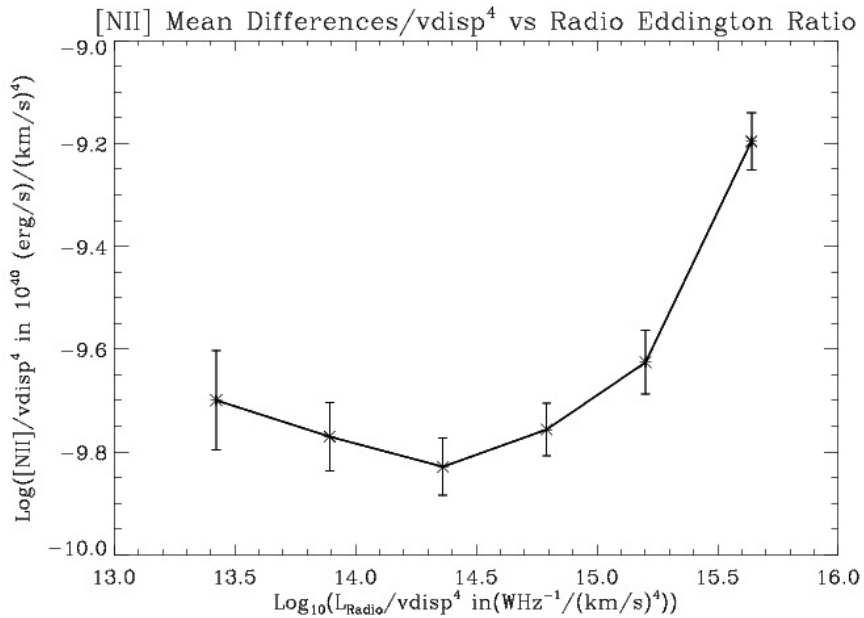


Figure 5.23: This plot compares the relationship of AGN [NII]-to-Eddington luminosity ratios to median radio luminosity-to-Eddington ratios. See the caption for Figure 5.22 for more details.

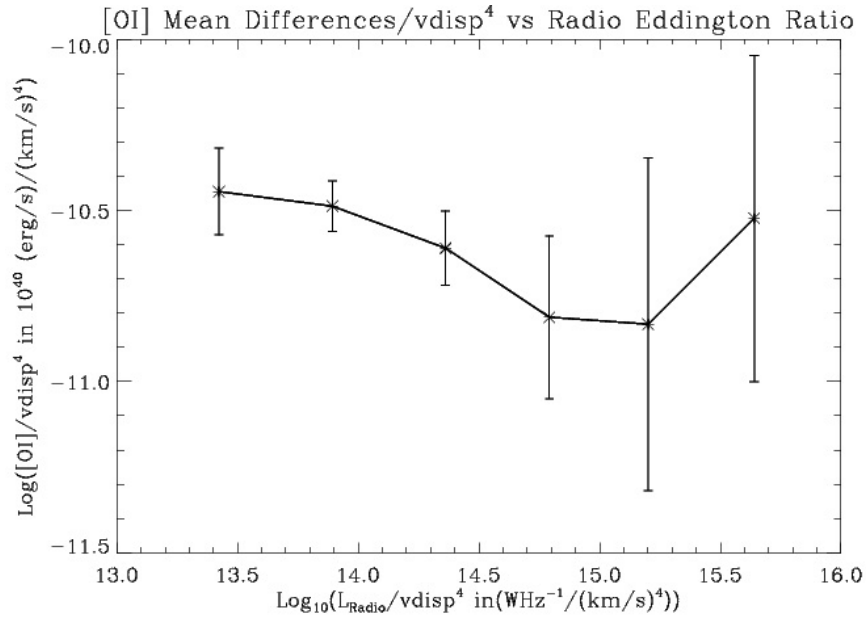


Figure 5.24: This plot compares the relationship of AGN [OI]-to-Eddington luminosity ratios to median radio luminosity-to-Eddington ratios. See the caption for Figure 5.22 for more details.

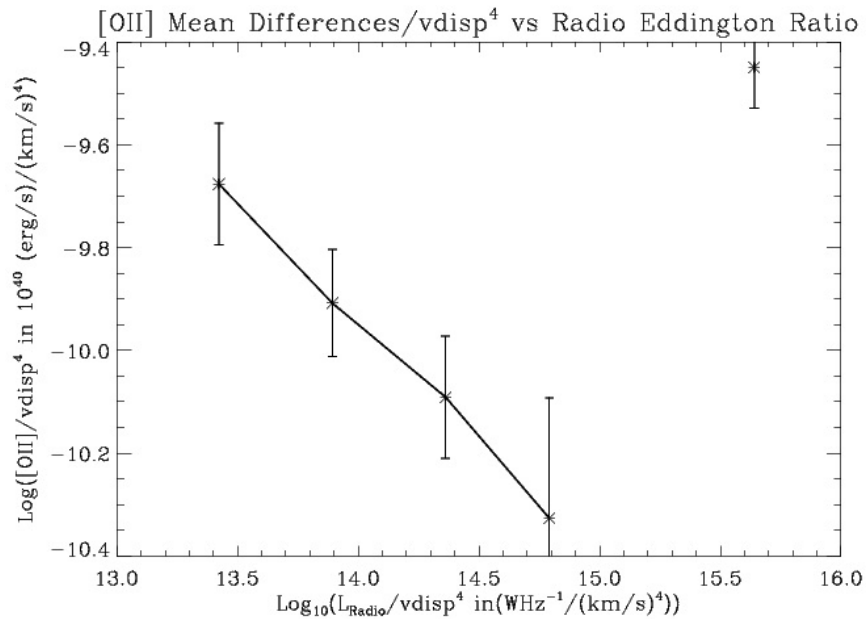


Figure 5.25: This plot compares the relationship of AGN [OII]-to-Eddington luminosity ratios to median radio luminosity-to-Eddington ratios. See the caption for Figure 5.22 for more details.

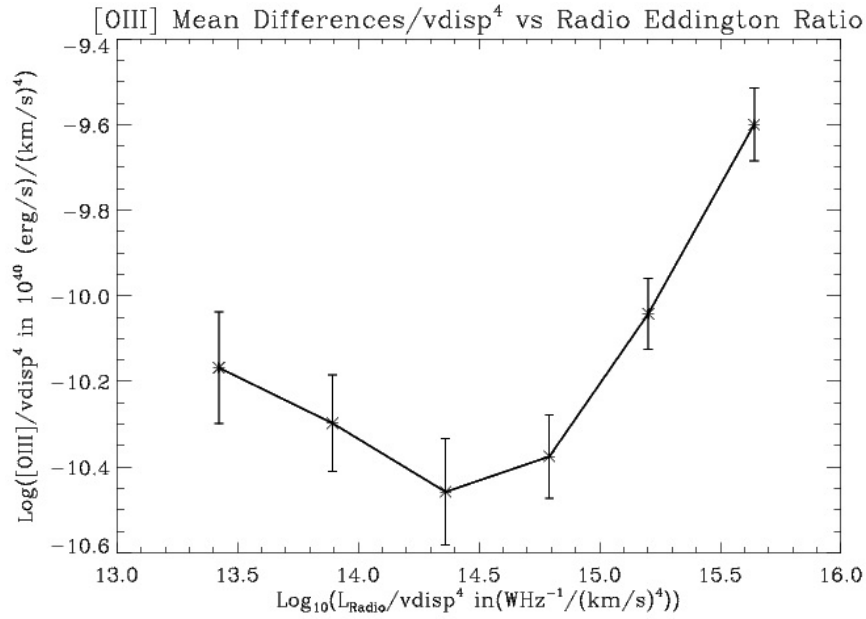


Figure 5.26: This plot compares the relationship of AGN [OIII]-to-Eddington luminosity ratios to median radio luminosity-to-Eddington ratios. See the caption for Figure 5.22 for more details.

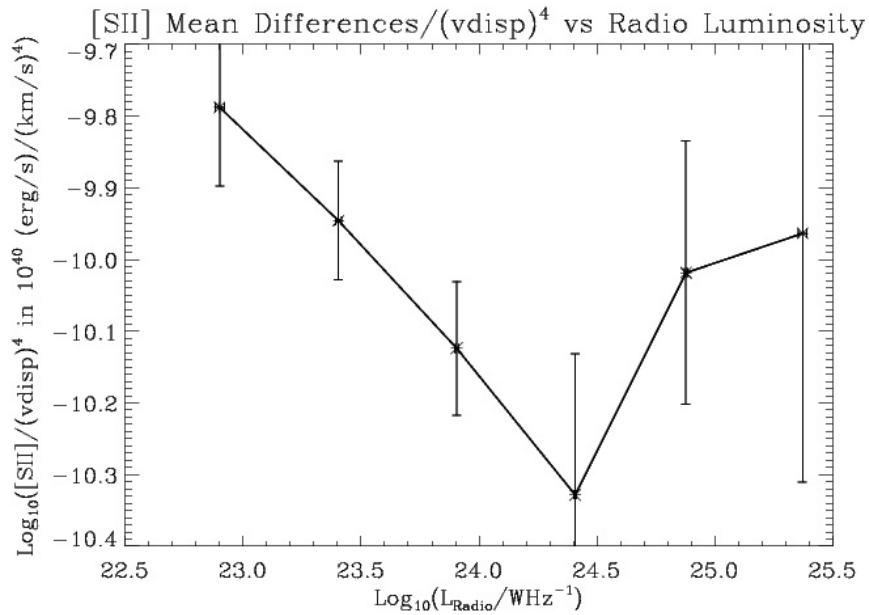


Figure 5.27: This plot compares the relationship of AGN [SII]-to-Eddington luminosity ratios to median radio luminosity-to-Eddington ratios. See the caption for Figure 5.22 for more details.

Chapter 6 Summary

In summary, we used SDSS and NVSS data (Chapter 2) and selected our radio samples from among red, older-stellar population galaxies (Chapter 3). We created radio-faint control samples to match the radio samples in stellar mass, redshift, and color.

Chapter 4 described early, straight-forward attempts to isolate the AGN-powered emission line distributions, as well as the drawbacks to these elementary methods. Despite the complexities of extracting AGN-powered emission line contributions, the simplistic subtraction of control from radio sample line medians alerted us to an interesting pattern wherein the differences between radio sample and control emission line medians decrease with increasing radio luminosity until the middle bins, and then increase thereafter.

Chapter 5 detailed our attempts to improve the previous chapter's results through using lognormal distributions to model the AGN-powered and non-AGN powered emission line distributions. We detailed the importance of correct noise estimates in this process. Our lognormal modeling failed to produce meaningful AGN-powered distributions for each and every line in every radio bin (due to problematic statistical spreads), but produced an estimate for the AGN-powered [OIII] across all bins. Moreover, if we consider the meaningful simulated data points for all of the lines (ignoring noisy $H\beta$), we frequently see this same "dipping" pattern, which is even more pronounced if we look at the differences in simulated emission line medians. We then discussed possible explanations for the "dipping" pattern, easily dismissing the influence of contamination by star-forming galaxies. Upon examining relations of emission lines and radio luminosities to Eddington limits, we conjectured that our samples cover a transition between AGN populations (possibly differing by dominant energy release mode, accretion, etc).

Reviewing the original goals of this project, our attempts to isolate the radio AGN contribution to emission lines had mixed success. Nevertheless, we noticed interesting patterns which could have implications for studying the output mechanisms of RIAF-powered radio AGN.

Bibliography

- Abazajian, K. N., Adelman-McCarthy, J. K., Agüeros, M. A., et al. 2009, *ApJS*, 182, 543, doi: 10.1088/0067-0049/182/2/543
- Belfiore, F., Maiolino, R., Maraston, C., et al. 2016, ArXiv e-prints. <https://arxiv.org/abs/1605.07189>
- Best, P. N., & Heckman, T. M. 2012, *MNRAS*, 421, 1569, doi: 10.1111/j.1365-2966.2012.20414.x
- Best, P. N., Kauffmann, G., Heckman, T. M., et al. 2005, *MNRAS*, 362, 25, doi: 10.1111/j.1365-2966.2005.09192.x
- Binette, L., Magris, C. G., Stasinska, G., & Bruzual, A. G. 1994, *A&A*, 292, 13
- Blandford, R. D., & Begelman, M. C. 1999, *MNRAS*, 303, L1, doi: 10.1046/j.1365-8711.1999.02358.x
- Blanton, M. R., Schlegel, D. J., Strauss, M. A., et al. 2005, *AJ*, 129, 2562, doi: 10.1086/429803
- Bruzual, G., & Charlot, S. 2003, *MNRAS*, 344, 1000, doi: 10.1046/j.1365-8711.2003.06897.x
- Bruzual A., G. 1983, *ApJ*, 273, 105, doi: 10.1086/161352
- Cid Fernandes, R., Stasińska, G., Mateus, A., & Vale Asari, N. 2011, *MNRAS*, 413, 1687, doi: 10.1111/j.1365-2966.2011.18244.x
- Condon, J. J., Cotton, W. D., Greisen, E. W., et al. 1998, *AJ*, 115, 1693, doi: 10.1086/300337
- di Serego Alighieri, S., Trinchieri, G., & Brocato, E. 1990, in *ASSL Vol. 160: Windows on Galaxies*, 301–+
- Dopita, M. A., & Sutherland, R. S. 1995, *ApJ*, 455, 468, doi: 10.1086/176596
- Eddington, A. S. 1925, *Monthly Notices of the Royal Astronomical Society*, 85, 408, doi: 10.1093/mnras/85.5.408
- Eracleous, M., Hwang, J. A., & Flohic, H. M. L. G. 2010, *ApJ*, 711, 796, doi: 10.1088/0004-637X/711/2/796
- Fanaroff, B. L., & Riley, J. M. 1974, *MNRAS*, 167, 31P, doi: 10.1093/mnras/167.1.31P
- Fenton, L. 1960, *IRE Transactions on Communications Systems*, 8, 57, doi: 10.1109/TCOM.1960.1097606

- Ferland, G. J., & Netzer, H. 1983, *ApJ*, 264, 105, doi: 10.1086/160577
- Frolov, V., & Zel'nikov, A. 2011, *Introduction to Black Hole Physics* (OUP Oxford).
<https://books.google.com/books?id=nZsNduVxmB8C>
- Gebhardt, K., Bender, R., Bower, G., et al. 2000, *ApJ*, 539, L13, doi: 10.1086/312840
- Ghisellini, G., & Celotti, A. 2001, *A&A*, 379, L1, doi: 10.1051/0004-6361:20011338
- Halpern, J. P., & Steiner, J. E. 1983, *ApJL*, 269, L37, doi: 10.1086/184051
- Hawley, J. F., & Balbus, S. A. 2002, *ApJ*, 573, 738, doi: 10.1086/340765
- Heckman, T. M., Baum, S. A., van Breugel, W. J. M., & McCarthy, P. 1989, *ApJ*, 338, 48, doi: 10.1086/167181
- Ho, L. C. 2008, *ARA&A*, 46, 475, doi: 10.1146/annurev.astro.45.051806.110546
- Kim, D.-W. 1989, *ApJ*, 346, 653, doi: 10.1086/168048
- Laing, R. A., & Bridle, A. H. 2002, *Monthly Notices of the Royal Astronomical Society*, 336, 328, doi: 10.1046/j.1365-8711.2002.05756.x
- Lin, Y.-T., Shen, Y., Strauss, M. A., Richards, G. T., & Lunnan, R. 2010, *ApJ*, 723, 1119, doi: 10.1088/0004-637X/723/2/1119
- Magorrian, J., Tremaine, S., Richstone, D., et al. 1998, *AJ*, 115, 2285, doi: 10.1086/300353
- Marlow, N. A. 1967, *The Bell System Technical Journal*, 46, 2081, doi: 10.1002/j.1538-7305.1967.tb04244.x
- McCarthy, P. J. 1993, *ARA&A*, 31, 639, doi: 10.1146/annurev.aa.31.090193.003231
- Meisenheimer, K., Roser, H.-J., Hiltner, P. R., et al. 1989, *A&A*, 219, 63
- Narayan, R., & Yi, I. 1994, *ApJL*, 428, L13, doi: 10.1086/187381
- . 1995, *ApJ*, 444, 231, doi: 10.1086/175599
- Netzer, H. 2013, *The Physics and Evolution of Active Galactic Nuclei* (New York: Cambridge University Press), 3–11; 43; 64–67; 84–90; 120–122
- Owen, F. N., & Laing, R. A. 1989, *MNRAS*, 238, 357, doi: 10.1093/mnras/238.2.357
- Papaderos, P., Gomes, J. M., Vílchez, J. M., et al. 2013, *A&A*, 555, L1, doi: 10.1051/0004-6361/201321681
- Quataert, E., & Gruzinov, A. 2000, *ApJ*, 539, 809, doi: 10.1086/309267

- Sarzi, M., Shields, J. C., Schawinski, K., et al. 2010, MNRAS, 402, 2187, doi: 10.1111/j.1365-2966.2009.16039.x
- Sijacki, D., Springel, V., Di Matteo, T., & Hernquist, L. 2007, MNRAS, 380, 877, doi: 10.1111/j.1365-2966.2007.12153.x
- Singh, R., van de Ven, G., Jahnke, K., et al. 2013, A&A, 558, A43, doi: 10.1051/0004-6361/201322062
- Stasińska, G., Vale Asari, N., Cid Fernandes, R., et al. 2008, MNRAS, 391, L29, doi: 10.1111/j.1745-3933.2008.00550.x
- Urry, C. M., & Padovani, P. 1995, PASP, 107, 803, doi: 10.1086/133630
- Urry, M. 2003
- Voit, G. M., & Donahue, M. 1990, ApJL, 360, L15, doi: 10.1086/185801
- Wilson, A. S., & Colbert, E. J. M. 1995, ApJ, 438, 62, doi: 10.1086/175054
- Yan, R. 2018, MNRAS
- Yan, R., & Blanton, M. R. 2012, ApJ, 747, 61, doi: 10.1088/0004-637X/747/1/61
- York, D. G., Adelman, J., Anderson, J. E., et al. 2000, AJ, 120, 1579, doi: 10.1086/301513

Vita

Jessica Short-Long grew up in Olive Hill, Kentucky, where she graduated from West Carter High School in 2007. She obtained her B.A. in mathematics and physics from Transylvania University (2011) in Lexington, Kentucky, before pursuing graduate work in physics at the University of Kentucky. She obtained her M.S. in physics from UK in 2015.